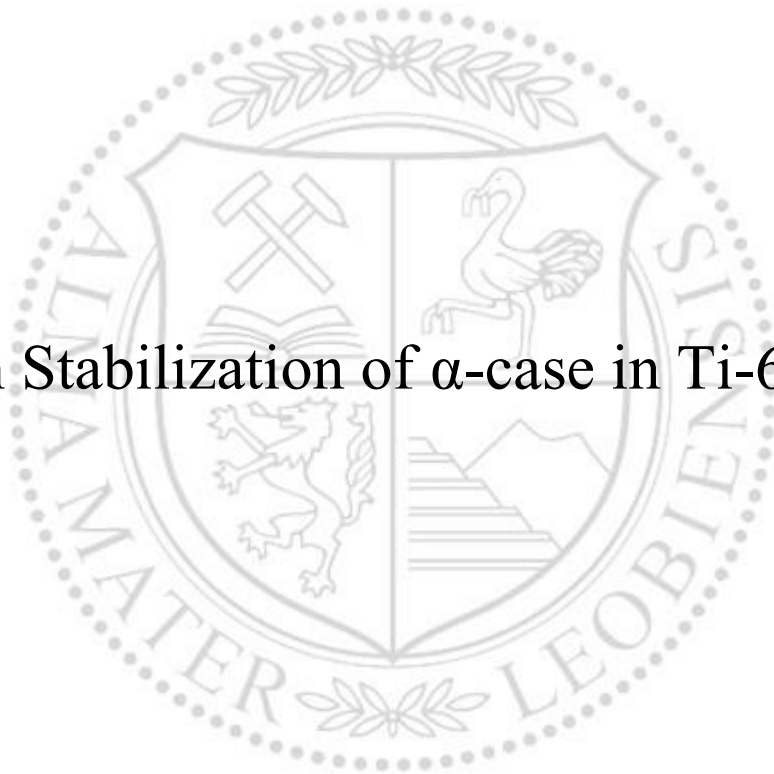Chair of Physical Metallurgy and Metallic Materials

Master's Thesis

Study on Stabilization of α-case in Ti-6Al-4V

Thomas Lukas, BSc

June 2021

MONTANUNIVERSITÄT LEOBEN www.unileoben.ac.at

EIDESSTATTLICHE ERKLÄRUNG

Ich erkläre an Eides statt, dass ich diese Arbeit selbständig verfasst, andere als die angegebenen Quellen und Hilfsmittel nicht benutzt, und mich auch sonst keiner unerlaubten Hilfsmittel bedient habe.

Ich erkläre, dass ich die Richtlinien des Senats der Montanuniversität Leoben zu "Gute wissenschaftliche Praxis" gelesen, verstanden und befolgt habe.

Weiters erkläre ich, dass die elektronische und gedruckte Version der eingereichten wissenschaftlichen Abschlussarbeit formal und inhaltlich identisch sind.

Datum 19.04.2021

_____

Unterschrift Verfasser/in

Thomas Lukas

Acknowledgments

Content

List of Abbreviations

$\bar{x}$	diffusional path
bcc	body-centered cubic
BOR	Burger's orientation relationship
c	concentration
cp	commercially pure
CRSS	critical resolved shear stresses
D	diffusion coefficient
EBSD	electron backscatter diffraction
EDX	energy dispersive X-ray spectroscopy
FIB	focused ion beam
hcp	hexagonal close-packed
IPF	inverse pole figure
j	diffusion current
LOM	light optical microscope
M_s	martensite start temperature
Q	activation Energy
R	gas constant
SEM	scanning electron microscope
T_β	beta transus temperature
vol.%	volume percent
WDX	wavelength-dispersive X-ray spectroscopy
wt.%	weight percent
XRD	X-ray diffraction
α'	hexagonal martensite
α''	orthorhombic martensite
α_s	secondary α phase

Abstract

This work was inspired by findings of a certain, rather unusual appearance of precipitations, which geometrically occurred in an L-shape, hence the name "L phase", within the microstructure of forging parts and plates made from the conventional (α+β) alloy Ti-6Al-4V, by voestalpine Böhler Bleche GmbH & Co KG. The parts and plates had a β annealing in common and the influence of oxygen was suspected in being responsible for the development of this phase. As each sample was exposed to an air environment, cooling inclusive. The assumption was that the material could form a sort of α case from within, by the oxygen content of the material. However, as this type of formation and its characteristic shape was never documented before, further investigations were to be aimed at.

The L phase should be reproduced and characterized due to its appearances and mechanical properties. Furthermore, an attempt in annihilating the L phase should be made, in order to control the development of this phase. Therefore, a comprehensive heat treatment study was made, with a subsequent light optical microscope (LOM) study to characterize the precipitation and growth behavior of the phase. An intensive microhardness study was additionally made, with which results a mathematical model was used to calculate the diffusion coefficient for oxygen in Ti-6Al-4V. By an electron backscatter diffraction (EBSD) measurement over a zone, which was nano indented, a correlation between the orientation of the phase and its mechanical properties was investigated. To receive proof of oxygen as a main contributor for the development of the L phase, chemical analysis using wavelength-dispersive X-ray spectroscopy (WDX), energy dispersive X-ray spectroscopy (EDX) and X-ray diffraction (XRD) were made.

Resulting in an extensive characterization of growth behavior of the L phase, a favorite growth condition within heat treatments was found as well as ways to complete annihilation of the phase. The hardness and Young's modulus were determined, as being considerably high compared to the ground material. Oxygen was verified as the main stabilizer of this phase and as a stronger stabilizer as aluminum for the α phase as well. Additionally, nitrides were proven within the surface zone of the specimens.

1. Fundamentals

In this chapter, an overview about the theoretical basics should be given in order to support the upcoming assumptions and conclusions. Not only titanium as an element and its alloys will be covered but also the state of the art in research will be mentioned. Due to diffusion calculations made in this thesis, a brief insight into diffusional models and operations is given as well.

1.1.   Titanium and its properties

Titanium, with the atomic symbol Ti and the atomic number of 22, is the fourth most common metal in the earth's crust. It has become commercially attractive with the "Kroll-Process", which is still used today. Yet only 5% of the production is used for metal or alloy purposes, larger amounts are being processed to TiO_2-powder and used as a permanent white pigment in paints for example [1, 2].

However, the widely most used alloy is Ti-6Al-4V (all compositions in wt%, unless indicated otherwise), with an approximate usage of 50% of all Ti alloys. The typical application area of Ti alloys is in aerospace. But there are more areas in which Ti alloys can be applied, for example in medical devices or motorsports [1, 2]. In this thesis the focus will be lain on Ti-6Al-4V.

With a melting temperature of 1668°C and a density of 4.5 g/cm^3 Ti belongs to the lightweight metals. Titanium forms a passivating oxide surface layer, which yields to a superior corrosion resistance up to 600°C. With increasing temperatures, however, Ti shows an excessive growth of the oxide surface layer, yielding to a steep decrease in its corrosion resistance at elevated temperatures. Due to this extensive layer growth and the implementation of leaks, the passivating effect is being considerably weakened. At 882°C commercially pure (cp) Ti shows an allotropic phase transformation [1, 2]. An allotropic transformation is a change of the crystal lattice in a solid state of the metal [3]. During cooling, however, the crystal structure of Ti transforms from the high temperature phase, called the β phase, with a body-centered cubic (bcc) crystal structure, into a low temperature, hexagonal close-packed (hcp) crystal structure, the α phase. Due to this fact, two different crystal structures (hcp and bcc) can be present in the titanium microstructure. A comparison of both unit cells is shown in Figure 1.
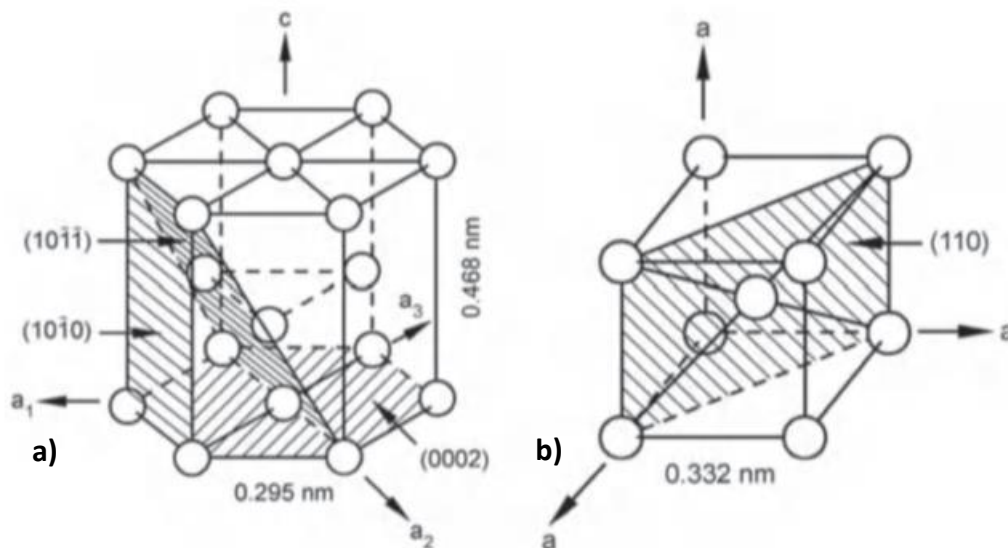
Figure 1: Unit cells of a) α phase with its three most densely packed lattice planes and b) β phase with on variant of its six most densely packed lattice plane [1].

With different crystal structures, there come different properties. The hexagonal α-phase, for instance, has an anisotropic character, which yields to a dependence of the elastic properties as a function of the declination angle between the c axis of the unit cell and the stress axis as can be seen in Figure 2. This explains why the Young's modulus of a single crystal at room temperature can vary from 145 GPa to 100 GPa [1, 2].

Additionally, the c/a ratio of α Ti is 1.587 (a=0.295 nm, c=0.468 nm) [1, 2]. In Figure 1 a) the lattice parameters c and a are shown. The c/a ratio of α Ti can be altered by implementing substitutional and interstitial atoms like Al or O [1, 2, 4, 5]. The smaller c/a ratio compared to a hcp crystal structure yields to a bigger distance between the prismatic planes {$10\bar{1}0$}. Thus, the packing density of the prismatic plane is higher than the basal plane {0001}. This yields to a simplified dislocation slipping on the prismatic plane, compared to the basal plane (Figure 3 b)). This phenomenon is crucial when it comes to slip during plastic deformation [1, 2].

Within the α phase unit cell there can be found four independent slip systems on two slip planes, the basal and prismatic plane (Figure 3 a)). There are three slip systems on both, but only two per plane are independent, which yields to an overall of four independent slip systems. The slip systems on the pyramidal plane are composed from basal and prismatic shears (c+a), which does not yield to an additional slip system. If the critical resolved shear stresses (CRSS) of each slip plane are compared, it shows that at room temperature the basal plane {0002} has a higher value of the CRSS than the prismatic plane {$10\bar{1}0$}. The pyramidal

plane {10$\bar{1}$1}, however, a combination of basal and prismatic slips, outstands them both (Figure 3 b)) in having the highest CRSS value.
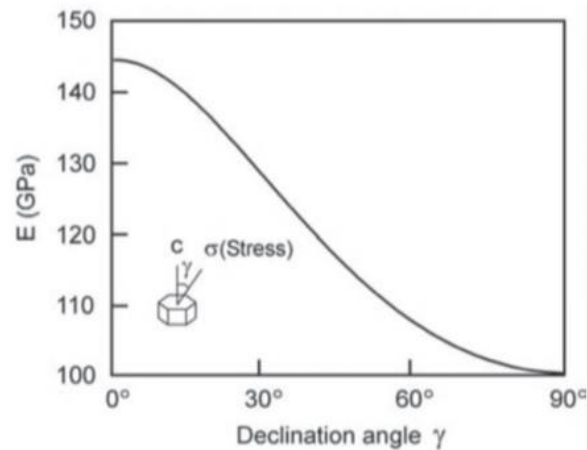
Figure 2: Young's Modulus dependency of declination angle γ, the angle between the normal vector of the basal plane (0002) and the stress axis [1]. This relation is valid only for single crystals.

Von Mises states that five independent slip systems are prerequisite for homogenous plastic deformation in metals [6], which is why deformation in polycrystalline hcp metals can be problematic at room temperature. However, α Ti has the urge to induce additional deformation and secondary slip systems as well as a mechanical twinning mechanism, which increases the possibility of deformation. This ductilization at low temperatures, due to twinning and activation of secondary slip planes are predominant especially in cp Ti and same α Ti alloys, hence not in (α+β) alloys and fully heat teated β alloys. As in (α+β) alloys, twinning is suppressed by several alloying elements. However, with the bcc β phase, the von Mises criterion is fulfilled, leading to an increase in ductility due to homogenous plastic deformation [1, 2].
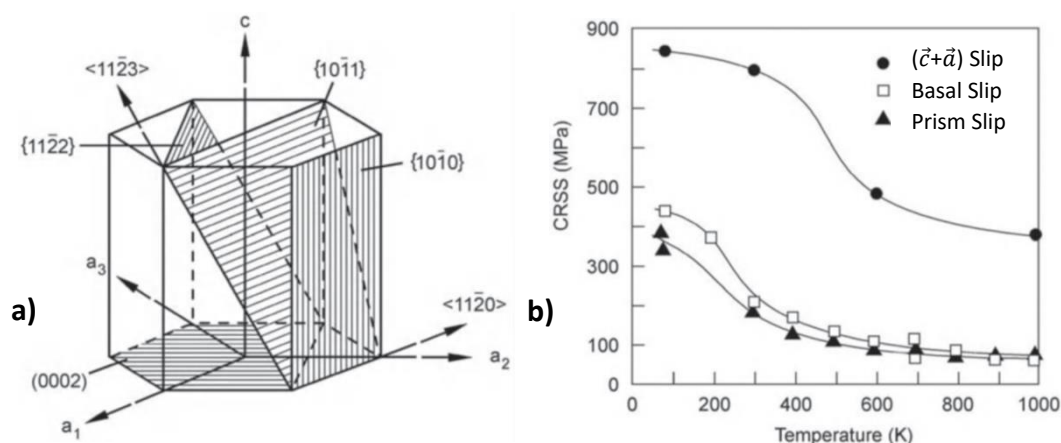
Figure 3: a) slip planes and slip directions of hexagonal α-titanium and b) critical resolved shear stresses corresponding to their slip planes [1].

As mentioned above Ti shows an allotropic transformation. This transformation from one crystal lattice to another crystal lattice (in Ti hcp to bcc) is vulnerable to diffusional processes. For instance, if the transformation is executed in a considerably fast period of time, thus by

suppressing diffusional processes, a martensitic structure is formed [1, 2, 3]. This will be explained in more detail later.

An aspect of Ti and its alloys worth mentioning is the formation of a so-called α-case. It is a hard and brittle surface of α grains. Usually, these grains are enriched with O leading to a high hardness of this surface layer. It is formed, for example, due to a reaction between the liquid Ti metal and the mold wall, developing TiO_2 first and then a solid solution of O within Ti. The α-case can reach a thickness of up to 500 µm as respected for Ti castings [7, 8].

Another characteristic of titanium is the precipitation of secondary α phase ($α_s$) when it comes to a β to α transformation. It is assumed that it is mainly nucleated at the grain boundary and is competing with the growth of primary α. However, $α_s$ phase is mainly observed in two-phase Ti alloys [9].

1.2.   Titanium alloys

Alloying elements have different effects in Ti. Vanadium, for example, stabilizes the cubic β phase. The β phase, with respect of vanadium as an alloying element, shows a lower elastic modulus, for instance. Aluminum, on the other hand, the most common α stabilizer, increases the elastic properties, due to its tendency of accompanying changes within the lattice and an increase in covalent bonding, respectively. This leads to a numerous number of possible applications for Ti [1, 2]. The most common elements for the stabilization of the α phase are Al, O, N and C. Common elements stabilizing the β phase are V, Mo, Nb and Ta. These elements, however, have influence on the thermodynamic behavior of Ti alloys. An equivalent over the variations of different Ti alloys in respect to a certain β stabilizer concentration can be seen in Figure 4 [1, 2].
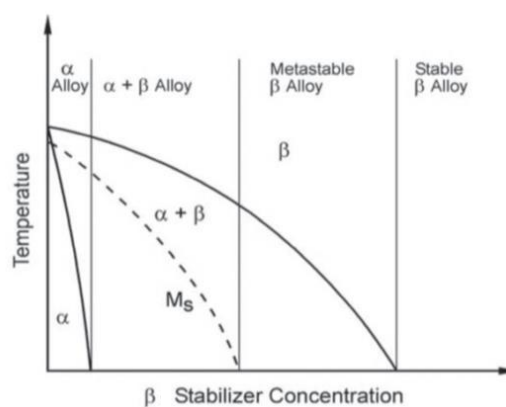
Figure 4: Pseudo-binary phase diagram, showing the different categories of Ti alloys [1].

The alloys are usually classified in four different categories: α, near α, (α+β) and β. This differentiation is made visible in Figure 4, which shows the alloy variety of titanium-based alloys and their differentiation. This thesis will focus on (α+β) Ti alloys, which combine the characteristics of both, α and β titanium. With a density of approximately 4.4 g/cm^3 and superior mechanical properties, Ti-6Al-4V is the most common representative of this alloy section [1, 2], and the material on which this work is based on.

In Figure 4 within the (α+β) alloy region a martensite start temperature (M_S) is depicted. As mentioned before, at a certain temperature a crystal lattice transformation occurs. With prohibition of diffusion-controlled processes, thus high cooling rates, a martensitic microstructure instead of an (α+β) microstructure can develop in (α+β) alloys. With increasing β stabilizing elements, such as vanadium, the respective phase transformation can be suppressed, resulting in a bcc structure of Ti.

1.3.   Martensitic transformation

Depending on the cooling rate the transformation from β Ti to α Ti can be martensitic or diffusion-controlled. When either is forming, an orientation relationship between the developed α-laths or platelets and the former β grains can be observed. The same formation was discovered first in zirconium, due to the similarities between zirconium and titanium, this relationship has been assumed for titanium as well and verified by Newkirk et al. [10]. The so-called Burgers orientation relationship (BOR) [10, 11].

According to this relationship, a bcc crystal can transform into twelve hexagonal variants with a difference angle of 60° between the formed α colonies. Yielding to six slip planes and two slip directions within a grain, leads to the twelve possible variants. This relation is found for both martensitic and diffusion-controlled transformations [1, 2]. The main difference of both is the form in which they appear to grow. As the diffusion-controlled microstructure has the conventional basket weave appearance with thick α laths surrounded by thin β precipitations. The martensitic microstructure shows thin α-laths in an acicular manner, which can hardly be observed under a conventional optical microscope due to their thinness. However, the orientation relation according to Burgers is shown here [10, 11]:

$$(110)_\beta || (0002)_\alpha$$

$$[1\bar{1}1]_\beta || [11\bar{2}0]_\alpha$$

The distance between the atoms in the basal planes of hexagonal α Ti is relatively bigger than the related distance of the {110} planes of the bcc β Ti. This yields to an atomic displacement during the β/α transformation and therefore, the c value of the hexagonal unit cell is decreased in size relatively to the a value, which yields to a reduced c/a ratio compared to an

ideal hcp lattice. A volume increase is observed due to this effect while the β to α-transformation is happening. This transformation is happening according to the BOR [1, 2].

The twelve variants consist of six glide planes and two glide directions, which yields to twelve possible orientations of the α crystal. Within the former β grains, α lamellae colonies are observed at lower cooling rates from the β phase field, showing the described growth directions. Within these colonies the orientation of the lamellae is the same, however, this property leads to the characteristic microstructure of Ti, the so-called basket weave. During continued cooling an initial α plate nucleate at a former parent β grain boundary and grow as parallel plates, taking over the same crystal orientation forming a so-called α colony. Growing along one of twelve possible growth directions, until meeting a different oriented α colony. This effect is validated for both, the diffusional nucleation and growth process and the martensitic transformation [1, 2, 10].

When the martensitic transformation occurs, diffusion is suppressed, yielding to the prevention of the nucleation and growth process of the α phase, but to a shear type process into a hexagonal martensitic or orthorhombic microstructure with dependence of the given alloying elements, respectively. Therefore, this transformation is accomplished through high cooling rates. Ahmed et. al. [12] found, that cooling rates above 410°C/s yield to a fully martensitic transformation in Ti-6Al-4V. Whereas cooling rates lower than 20°C/s yield to a lamellar, basket weave state, thus to a nucleation and growth transformation.

As described above, there exist twelve possible crystallographic variants of α in a parent β grain. At slow cooling rates, when there is sufficient time for diffusion, the α phase forms in colonies of laths, while cooling down from the β phase field. Lamellae belonging to one and the same colony are of the same orientation according to the BOR. Basket-weave structures promote a more uniform distribution of all twelve variants. These α crystals have the orientation of one of the possible twelve Burgers orientations [13], with respect to the orientation of the former β grains.

The martensitic transformation, which is further analyzed in the course of this thesis, involves an atomic movement process, where the bcc structure transforms into a hcp structure. This process can be expressed by a shear process, in which following shear systems are activated: $[2\overline{1}\overline{1}3]_\alpha$ $(\overline{2}112)_\alpha$ and $[2\overline{1}\overline{1}3]_\alpha$ $(\overline{1}011)_\alpha$ [1]. This martensite form is referred to as hexagonal martensite or α', the orthorhombic martensite mentioned above is known as α''. However, there are two morphologies distinguished in literature [1, 2], the massive and the acicular martensite. While on the one hand the massive martensite only occurs in cp-Ti, with large irregular regions filled with almost parallel α laths, growing according to the BOR, the acicular martensite, on the other hand, contains various individual α plates, with each growing according to the BOR. The acicular martensite emerges within alloys with higher solute

content. It should be mentioned, that with higher solute content, the microstructure transforms from the hexagonal martensite α' to the orthorhombic martensite α'' [1, 13, 14].

1.4.   Diffusion

According to the definition by J. Crank [15]: "*Diffusion is a process by which matter is transported from one part of a system to another as a result of random molecular motions*". Motions which are in close relation to heat conduction, yielding to the assumption that in materials with a lower heat conductivity, diffusion is rather prohibited [16]. In the following chapter, the basic mechanisms and physical principles should be discussed. In every system, matter will flow in a manner which will decrease an initially existing concentration gradient, in order to maintain the lowest possible Gibbs free energy. This is how an inhomogeneous system becomes homogenous and this flow of matter will cease. This problem can be described by equation 1 [17].

$$j = -D \nabla c \quad \left(\text{one} - \text{dimensional: } j = -D \frac{\delta c}{\delta x} \right) \quad (1)$$

Properly known as the Fick's first law, with j as the flux, D as the diffusion coefficient and c as the concentration. This law fits the empirical finding that the flux goes to zero, if homogenization is reached in equilibrium and thus, the state with the lowest Gibbs free energy. Because this equation describes the steady state, concentration changes with time must be taken into account as well. Thus, Fick's second law is applied, equation 2 [17].

$$\frac{\delta c}{\delta t} = D \nabla^2 c \quad \left(\text{one} - \text{dimensional: } \frac{\delta c}{\delta t} = D \frac{\delta^2 c}{\delta x^2} \right) \quad (2)$$

The diffusion coefficient is empirically found and can be characterized by equation 3 [15, 16, 17].

$$D = D_0 \exp \left(-\frac{Q}{RT} \right) \quad (3)$$

D_0 acts as a pre-factor and Q as the activation energy. These will vary with composition, crystal structure e.g. This exponential relation allows to plot the diffusional behavior of a specific material and the alloying elements within the material in an Arrhenius-plot. Therefore, depicting the possibility of diffusion at a given temperature. With an estimated D for the according temperature T, D_0 and Q can be experimentally found [17]. In Figure 5 the diffusivity data of cp-Ti and its most common alloying elements are shown. The difference of diffusion due to the different crystal lattice should be noted as well. As self-diffusion in a hexagonal hcp crystal is significantly slower compared to a cubic bcc crystal [1, 2, 3].

The concentration is determined as a function of position and time, c(x,t). With a short diffusion distance and therefore no complete homogenization, the concentration c(x,t) can be expressed in terms of error functions. Another way to express c(x,t) by complete homogenization is to form the first important terms of an infinite trigonometric series [17]. With equation 2 being a linear, homogeneous differential equation, initial and boundary conditions are needed for receiving a solution. This is done in order to receive a solution and is a simplification, which is not applicable for every case. Therefore, the available space for diffusion is assumed to be infinite large. Meaning that the available space must be bigger compared to the characteristic length of the diffusion $\bar{x}$, which can be expressed by equation 4 [15, 16, 17].

$$\bar{x} = 2\sqrt{Dt} \quad (4)$$

The most common way for finding a solution for the concentration difference is with the approach of the Gaussian function, i.e. with the error function (erf). The Gaussian error function being a linear transfer of partial solutions of the diffusion equation, is applied as a valid solution of the same. The error function is tabularized and can be looked up. At this point it should be mentioned that for a simplified notation it can be useful to utilize the term "erfc", being the abbreviation for 1-erf() [17]. If applied onto a special case, where a certain concentration is infinite at the surface (c_0) and zero in the sample at time t=0, a concentration distribution can be written as in equation 5 [15, 16, 17].

$$c(x,t) = \frac{c_0}{2} \operatorname{erfc}\left(\frac{x}{\bar{x}}\right) = \frac{c_0}{2} \operatorname{erfc}\left(\frac{x}{2\sqrt{Dt}}\right) \quad (5)$$

In the case of this thesis, a unidirectional diffusion into a semi-infinite solid occurs, thus the initial and boundary conditions for equation 2 are c(x,0) = c_i, c(0,t) = c_0, D = constant. The concentration distribution is depicted in Figure 6. Thus equation 5 can be transformed for this purpose. The same solution of Song et al. [18] can be used as seen in equation 6.

$$\frac{c - c_i}{c_0 - c_i} = \operatorname{erfc}\left(\frac{x}{2\sqrt{Dt}}\right) \quad (6)$$
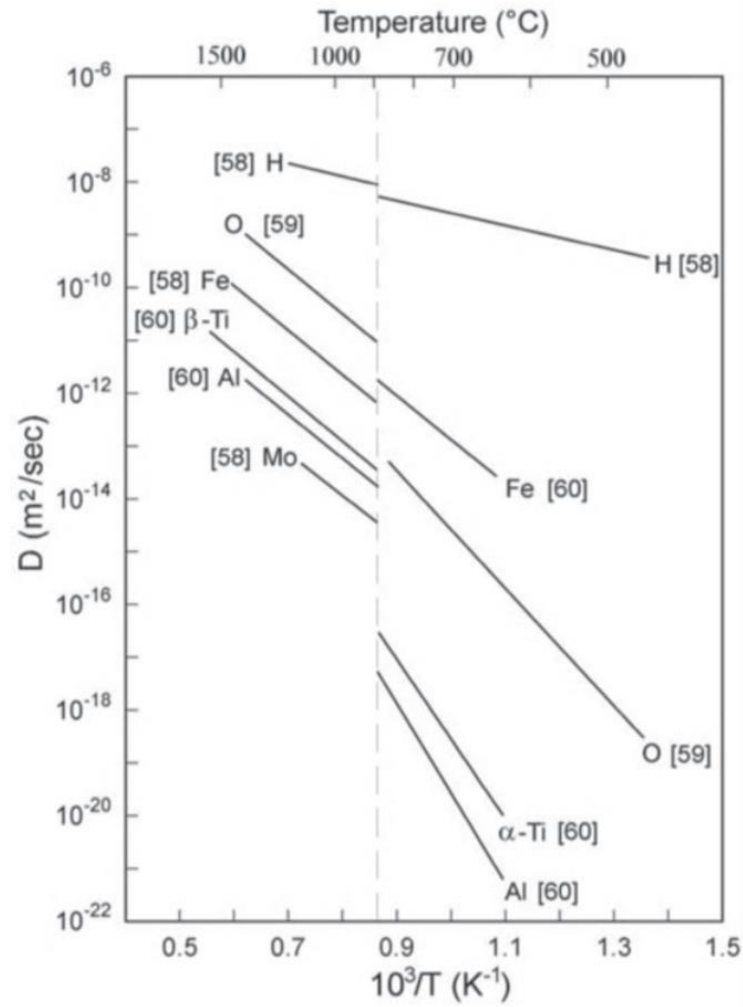
Figure 5: Arrhenius-plot of Ti self-diffusion and the diffusion behavior of the most common alloying elements of Ti in the β and α phases [1].
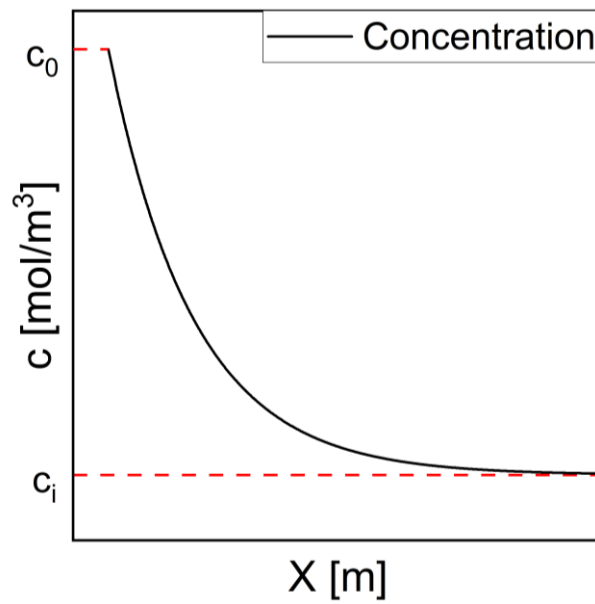
Figure 6: Schematic illustration of a concentration distribution in a sample.

However, to understand the mechanisms of diffusion properly, the characteristics of atomic movement must be internalized. The basis of every diffusion mechanism is the model of the Brownian motion, which was first discussed by Einstein in 1905 for liquid motions [19]. This motion can be applied in solids too. It describes the motion of atoms with a random walk model. This indicates a periodic jumping of atoms from one lattice site to another. There are three different ways, which are commonly used to describe this procedure. First, the interstitial mechanism, where an atom moves from one interstitial site to one of its nearest-neighbor interstitial sites, without permanently displacing any of the matrix atoms. If this occurs with a presumably larger matrix atom, a distortion will occur, this mechanism is called interstitialcy mechanism. Third, the vacancy mechanism, where unoccupied lattice sites, i.e. vacancies, are switching places with an atom in its near environment [17].

As mentioned above, diffusion is always intertwined with the heat flow. The heat flow can be decreased by various atomic imperfections, lattice impurities or the lattice itself. For instance, the hcp crystal structure is a close-packed atomic lattice, which does not benefit the heat flow of a system, therefore diffusivity is low. This phenomenon is very important in titanium due to its allotropic phase transformation. In the hcp α Ti diffusion is significantly lower than within the bcc β Ti phase. This is accurately demonstrated in Figure 5, as it can be seen, that diffusivity increases abruptly for most of its alloying elements in the β region [1, 2, 17].

As O plays a major role in this thesis, further focus should be held on the O diffusion in Ti-6Al-4V. As mentioned above, together with O, Ti can form an oxide layer on the surface with an additional O diffusion layer beneath it, where O is in solid solution [8]. TiO_2 in form of rutile and anatase are the most common modifications of TiO_2 as an oxide layer [8, 20]. If the diffusion of O in the O diffusion zone yields to dissolution, these hard and brittle zones are forming, leading to a loss of ductility and fatigue resistance [8, 21]. Ti has a very high affinity to O, demonstrated by a thin passivating oxide layer formation even at room temperature. At temperatures above 200°C, the thickness of the oxide layer continues to grow. An oxygen diffusion zone can be detected at temperatures above 400°C. At temperatures above 600°C, the oxide layer is becoming more and more defective, due to increasingly high oxide formation rates, also yielding to an easy access of O into the underlying substrate. At even more elevated temperatures (above 800°C), oxidation degrades the high temperature performance of titanium unprecedentedly, due to dissolution of the material into a thick oxide layer and a deep oxygen diffusion layer [1, 2, 22, 23]. Du et al. [24] found that with higher oxidation temperatures and/or longer oxidation times a formation of a multilayered oxide layer is established. Due to alternate growth of Al_2O_3 and TiO_2 layers by outward diffusion of Al and inward diffusion of O. At the early stages of oxidation, Al_2O_3 nucleates on the surface together with TiO_2, with increasing oxidation times, Al_2O_3 grows and covers TiO_2. Even though the

experiments of Du et al. were made at much longer oxidation times compared to the times of exposure to O for the specimens within this study, the kinetics of the alloying elements, Al and O, were observed.

Guleryuz et al. [25] oxidized Ti-6Al-4V-samples for different time intervals up to 72h within a temperature range of 600 to 800°C. A microhardness study was made to analyze the hardness of the oxide layer and the oxygen diffusion zone. They found a correlation between the microhardness measurements in HV and the concentration profile, represented by the erf() term, given in equation 7.

$$\frac{HV_X - HV_S}{HV_0 - HV_S} = \mathrm{erf}\left(\frac{X}{2\sqrt{Dt}}\right) \qquad (7)$$

HV_X is the hardness at depth X, HV_S is the surface hardness (at X=0) and HV_0 is the hardness value at a semi-infinite distance from the surface. With given microhardness values, D can be calculated, thus D_0 and the activation energy Q can be obtained with equation 3.

By comparing equation 6 with equation 7 a connection can be built between the concentration and the effect of solute strengthening of the observed material. Therefore, with the knowledge of the hardness properties of a material, an estimation can be made of the concentration profile of the foreign atomic content, which is responsible for the varying hardness of the used material, as seen in equation 8.

$$\frac{c - c_i}{c_0 - c_i} = \frac{HV_X - HV_S}{HV_0 - HV_S} \qquad (8)$$

As much was documented about the influence of O on the Ti microstructure, less is known about the influence of N on the microstructure of Ti. The chemical affinity for N and Ti is significantly lower compared to O and Ti [1, 2]. Therefore, N-effects on Ti and its alloys are not well investigated, but especially hardening and embrittlement of Ti under N influence is documented. However, N shows a hardening effect in various other metals, as well and is industrially used in the course of a surface strengthening treatment i.e., nitriding, to enhance wear resistance [3]. This effect may be of interest for Ti and its alloys as well, thus further research regarding the influence of N on Ti is necessary.

2. Material and experimental

In this chapter, an overview about the individual experimental methods, which were used during this thesis should be given. For all procedures Ti-6Al-4V was used as tested material. The test sample geometries were cut out of β forged slab material. The chemical composition in weight percentage (wt.%) can be seen in Table 1. The geometries for the used specimens are 10 mm x 5 mm x 2 mm and were cut with an Accutom-5R cutting machine, using a diamond cut-off wheel B0D35 from Struers.

Table 1: Chemical composition of the tested material, a conventional Ti-6Al-4V (Grade 5).

	Ti	**Al**	**V**	**Fe**	**O**
wt.%	bal.	6.34-6.45	3.96-4.05	0.18	0.18

For illustrating most of the plots in order to evaluate the measured results (see Chapter 3), Origin 2020 was used as software, if not mentioned otherwise.

2.1. Heat treatment

As already mentioned, as a motivation for this thesis a particular phase with a L shape geometry was found during microstructural characterizations, in samples of conventional Ti-6Al-4V (Grade 5) at an industrial partner. These parts, however, where intended as forged parts or plates, which had a β-phase annealing around 1050°C for up to five hours. Due to this extraordinary shape of an "L", it will be from now on referred to as "L phase".

The following heat treatments were entirely performed on a Bähr DIL 805A quenching dilatometer from TA Instruments. As a first step and in order to reproduce the L-phase, the Ti-6Al-4V samples were heat-treated for 45 min at different temperatures, with a heating rate of 3°C/s and a cooling rate of 200°C/s. The annealing temperatures, however, varied from 950°C, below the single β phase field, up to 1300°C, with a temperature increase of 50°C from sample to sample. Afterwards, in order to analyze the growth behavior of the L phase, the heat treatment was altered due to the holding times, leading to 15, 30, 45, 60, 75 and 90 min of exposure within the dilatometer. The annealing temperature, however, was fixed with 1200°C due to limitations of the present dilatometer type. The heating and cooling rate were the same as prior mentioned. Finally, to get an even deeper understanding of the growth process, the cooling rate was altered. For this purpose, the samples were heated to 1200°C with a heating rate of 3°C/s, held for 60 min, in order to ensure a high oxidation of the samples. The applied cooling rates were 1°C/s, 15°C/s, 20°C/s, 100°C/s and 200°C/s. The different cooling rates should give further insights into the precipitation behavior of the L phase. Ti-6Al-4V exhibits a martensitic β/α phase transformation at cooling rates above 20°C/s and a

diffusion-controlled transformation at rates lower than 15°C/s, with both between these two cooling rates.

All heat treatments were performed in air, the cooling agent, however, was nitrogen gas (N_2), with a gas flow of 450 l/min, leading to a well controllable cooling of the sample and the dilatometer chamber.

2.2. Metallography

After the heat treatment the specimens were embedded with a CitoPress 20 from Struers. For the embedding mass, Polyfast was used. The metallographic preparation according to Fleißner et al. [26] was used in order to get optimum results. For this the embedded samples were mounted in a Tegramin from Struers, where the samples underwent a grinding and polishing process. The grinding process consisted of a 400 μm abrasion with the Struers MD Grinding Surface, MD Piano #220 followed by a double, fifteen seconds treatment with the Struers Silicon Carbide Foil, SiC #1200 and lastly a three step, fifteen seconds treatment with the Struers Silicon Carbide Foil, SiC #2000. The polishing process consisted of an 8-minute polishing treatment with a Struers OP-Chem Foil. The polishing mixture consisted of 950 ml Struers OP-S NonDry, 0.25 μm silica suspension and 150 ml H_2O_2.

The samples were afterwards cleaned with water and soap. Conventional soap showed great power in removing remaining OPS particles. An ultrasonic cleaning step with ethanol and acetone should be added too. As for the etching, a Kroll-etchant was used, consisting of HNO_3-acid and HF-acid in H_2O. With the etching completed, the samples were ready for an optical investigation, therefore the LOM Axio Imager from Carl Zeiss was used. For picture editing the software Gimp, version 2.10.22, was used. The focus in this step should be on the characterization of the different appearance of α case and hence, L phase and changes within the microstructure due to the different heat treatments applied. To determine the thickness of the L phase affected zone in the specimens, which was done with ImageJ, version 1.53f, five measurements, taken from the LOM pictures of each sample, were used and the average value was calculated.

2.3. Hardness measurements

In order to characterize the L-phase and the effect of it within the microstructure, a hardness study according to Vickers was examined. This was necessary because the L-phase is mainly considered as an α phase within the martensitic microstructure, which is stabilized by O. Hence, a higher hardness is expected.

For this purpose, a Qness Q60A+ automatic hardness testing machine was used. On each sample an area testing, consisting of five columns with thirteen lines leading to 65 indents,

was performed. The testing area must include the edge zone and the zone of uninfluenced microstructure near the sample middle. This is to gain an overview of the influenced zone by the L phase. The calculated hardness values were then plotted into diagrams to demonstrate the impact of the various heat treatments on the mechanical properties, more precisely the strength, which goes in proportion with the hardness. Therefore, the hardness values were averaged over five indent values, which is the amount of indents per row, for 13 rows in total. Leading to 13 averaged hardness values per tested specimen as a function of depth ([HV]=f(x)). The distance between the indents was chosen to be of 60 μm, to avoid effects related to stresses, gaining a minimum distance from the surface of 720 μm.

2.3.1.   Nanoindentation

A more detailed understanding of the interaction between L phase and the sample matrix can be achieved by nanoindentation measurements. The nanoindentation experiments were conducted on an InForce-50 from Nanomechanics Inc. (Oak Ridge) to determine the Young's modulus and the hardness of both, L phase and matrix.

Therefore, the etched sample, which was heated up to 1250°C for 45 min and cooled with 200°C/s, needed to be polished off the etched surface. This was accomplished by the use of a vibratory polisher, Vibro Met 2 by Struers, for several hours. The polishing surface was a Buehler MicroCloth, as lubricant the same OP-S mixture as in the polishing step before was used. A subsequent cleaning of the remaining OP-S particles in acetone was performed with an ultrasonic bath to be able to carry out the nanoindentation measurements. The testing itself was then proceeded under a 30° angle, with respect to the specimen's edge. An area scan, with a distance of 5 μm between each indent and row, in immediate surface distance was established to cover an area of 5200 μm2. This measurement was done to get a closer understanding of the mechanical properties between L phase and martensitic matrix.

2.4.   Diffusion calculation

As already mentioned in the second chapter, Guleryuz et al. [25] found a correlation between the hardness of an oxidized material and the content of O in Ti-6Al-4V. By applying equation 6 of Song et al. [18] a correlation between the oxygen content and the hardness can be estimated. By using this method, the diffusion coefficient of O in Ti-6Al-4V can be estimated and thus an Arrhenius plot can be created.

For demonstration purposes an example calculation shall be made with a sample, which was heat-treated at 1200°C for 45 min in air and cooled down with 200°C/s using a N_2 cooling agent. However, hardness and the according distance values are needed in order to perform the calculation.

$$\frac{HV_X - HV_S}{HV_0 - HV_S} = \frac{795{,}9 - 1020}{560 - 1020} = 0{,}487218 \qquad (9)$$

First the hardness term of equation 7 is calculated. For HV_X the microhardness value of an indent, which is 81 µm away from the surface was used for this example. In order to receive an accurate fit for the error-function term, an exponential fit for the measured hardness values (HV_{exp}) should be made, with the help of this a more continuous function is established. If the error function term is aligned to the established exponential fit, the most suitable diffusion coefficient is found. The exponential fit for the measured hardness values was achieved by applying following equation 10.

$$HV_{exp} = HV_S + (HV_0 - HV_S) * \exp\left(-\frac{x}{C_{exp}}\right) \qquad (10)$$

C_{exp} is an exponential coefficient which can be altered to achieve the best suited fit. HV_{exp} can be put into equation 9 by replacing HV_X, to get a smoother approximation of a diffusion curve. With this an approximation of the diffusion coefficient can be achieved. As a next step the term of the error function is calculated in equation 11.

$$\mathrm{erf}\left(\frac{X}{2\sqrt{Dt}}\right) = \mathrm{erf}\left(\frac{81 * 10^{-6}\,[\mathrm{m}]}{2 * \sqrt{D\left[\frac{\mathrm{m}^2}{\mathrm{s}}\right] * t[s]}}\right) \qquad (11)$$

In equation 11 X is the distance of the comparable indent location, for this example 81 µm, t the holding time in seconds and D is the diffusion coefficient for O in Ti-6Al-4V. By altering the diffusion coefficient, the results of equation 9 can be fitted to the results of equation 8. Thus, the diffusion coefficient can be estimated. With (4) the mean diffusion distance of O can be estimated as well.

By applying this procedure on each indentation row, the according diffusion coefficient of O in Ti-6Al-4V can be estimated, using the mathematical fit for the exponential function and D. Further, by applying this procedure for many samples in a wide temperature range, an Arrhenius plot can be made. With this calculation the area of O influence can be determined and used for further explanations.

2.5. Electron backscatter diffraction

For the EBSD measurements, however, a deformation-free surface guarantees an improved diffraction pattern. Therefore, the samples intended for EBSD measurements were put into a plasma cleaner for four hours in addition. By applying an EBSD measurement, further insight into the crystal structure and orientation relationship between the L phase and the matrix can

be achieved. Because the optical investigation indicates that the growth of the L-phase proceeds according to the BOR, this measurement is crucial for the understanding of this process. The EBSD measurement was performed with a focused ion beam (FIB), Versa 3D HiVAC. The parameters used for this measurement were an acceleration voltage of 20 kV and a spot size of 4.0. For analyzing the EBSD data, the TSL OIM Analysis software version 7 was used.

2.6. Chemical analysis

After investigating the physical properties of the L phase, an analyzation of its chemical composition is inevitable to gain a further understanding of the phase. An EDX measurement was made in order to detect the distribution of O within the sample. Point measurements were made in different distances to the surface and in addition a two-dimensional map was created for one of the used investigated specimens. This EDX measurement was only performed on one specific sample, which was heated up to 1200°C, held for 60 min in air and cooled to room temperature using N_2 gas with 50°C/s.

To obtain a more accurate result of the O distribution within the O affected zone a line scan from the surface area into the sample middle with a WDX was applied as well on two selected samples. With this method the differences in the chemical composition between L phase and matrix can be quantitatively measured. Thus, it is necessary to scan an area where both, L phase and matrix can be observed. This WDX procedure was performed on two samples of different heat treatments. One sample was heated to 1200°C for 45 min in air and cooled down using N_2 gas with 200°C/s. The other one was heated up to 1200°C, held for 60 min in air and cooled using N_2 gas with 50°C/s. Each sample had a different microstructure due to the heat treatment. A post treatment as described prior to get rid of the etched surface layer has proven to deliver sufficient surface quality.

2.7. X-Ray diffraction

To intepret the chemical profiles of the WDX results a XRD measurement was additionally made, with a Bruker-AXS D8 Advance. Inconsistencies could be observed due to an unexpected decrease of the Al content and O content at the immediate surface area, whereas the Ti content was not affected. Therefore, the specimens, on which the investigation took place were the same, as were described in Chapter 2.6. The XRD was used to investigate the sample surface after heat treatment. However, to determine the present phases from the diffraction patterns the beta software of Topas 2002 was used. The different intensity peaks of the occurring phases were found with the help of Materials Project [27] and CrystalMaker X, version 10.5.4.

3. Results and discussion

The generated results of this thesis will be shown with a subsequent discussion of these, following in each chapter. The structure will be the same as in the previous chapter. Starting with a LOM study for the various heat treatments, for illustrating the different impacts on the microstructure depending on the heat exposure in an air environment. Followed by the diffusion calculation, where an approximation-model to illustrate the O diffusion in Ti-6Al-4V is applied. The microhardness and nanoindentation investigations afterwards can therefore be discussed with more detail, while the EBSD measurements, combined with the nanoindentation measurements, give a deeper insight into the crystallographic background and the mechanical properties of the L phase. This chapter will conclude with the presentations of the chemical and surface analysis.

3.1.   Microstructural characterization via LOM

First, the unique geometries of this particular form of α phase should be discussed. As the name of the phase hints the form already, it has a remarkably similarity with an "L", found on LOM images after certain heat treatments made on Ti-6Al-4V (Grade 5) samples. There are, however, other shapes as well. Many L phases seem to be intertwined and distorted, which might be due to the grinding direction. Another property of interest is their growth direction. Because the phase seems to grow with a certain orientation, it is assumed that the L phase might be growing according to the BOR as well. Because of its light appearance on LOM pictures of etched samples, it also hints being stabilized α phase. As with a Kroll etchant and bright field mode at LOM, the α phase appears white, whereas the β phase dark. The occurrence of the L phase was in β annealed samples, with air cooling at the end only. Therefore, exposure to O during holding and cooling was inevitable.

With the heat treatment study described in Chapter 2.1, the focus lies on the differentiation of several appearances of the L phase. Basically, the attempt in this study was to manipulate the L phase in its growth behavior, to see if this particular phase can be prevented or positively oriented in the growth habit to even gain useful mechanical properties. As mentioned in Chapter 2.1, three different heat treatment parameters were varied: annealing temperature, holding time and cooling rate.

First, by altering the annealing temperature to higher temperature values, starting from 950°C and ending at 1300°C with an increase in temperature of 50°C per step. However, the heat treatment of 1200°C had promising results, leading to a dense layer of accumulated L phase near the surface, as seen in Figure 7, which was achieved with this particular heat treatment process. Even though tests above 1200°C show an increased growth behavior, testing at higher temperatures might lead to higher wear of the dilatometer equipment, which was used. Due

to the numerous amounts of heat treatments at elevated temperature, which are to follow, 1200°C was chosen to be the most representable condition. The thickness was determined as being the L phase affected zone, starting from the surface.
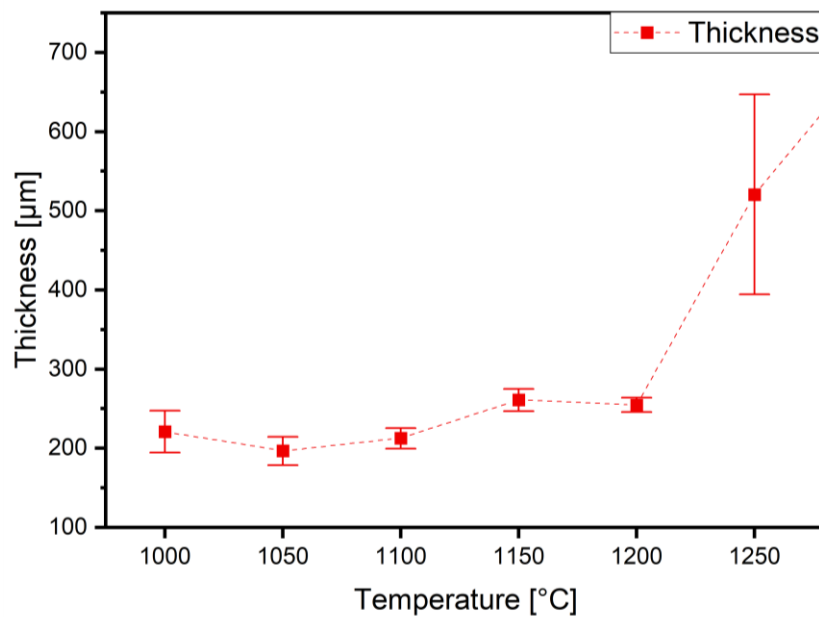
Figure 7: Thickness progression of L-phase affected zone within the microstructure of the samples at different annealing temperatures. With a heating rate of 3°C/s a holding time of 45 min and a cooling rate of 200°C/s.

In a second step, the influence of the holding time should be investigated. Therefore, the samples were exposed to 1200°C for different holding times, reaching from 15 min to 90 min, with an increase of 15 min per step. The sample with a high accumulated L phase influenced zone and still a uniform distribution of L phase was found at 60 min of holding time (Figure 8).

Lastly, the cooling rates were altered from 1°C/s up to 100°C/s. Due to the pronounced effects of the heat treatment with a holding time of 60 min at 1200°C, all treatments in this step were made with these parameters, because a more uniform distribution of the L phase affected zone was gained within the microstructure, unlike the heat treatments with a longer holding time.
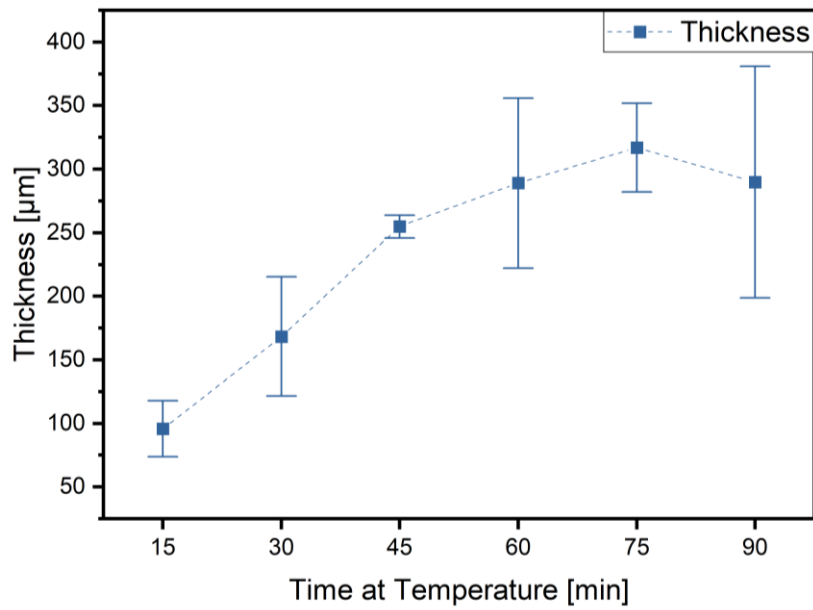
Figure 8: Thickness progression of L-phase affected zone within the microstructure of the samples at different holding times. With a heating rate of 3°C/s a holding temperature of 1200°C and a cooling rate of 200°C/s.

Within this heat treatment step cooling rates were changed to slower ones than 200°C/s, which means more exposure to diffusional processes. Nevertheless, the thickness of the zone declines with lower cooling rates as seen in Figure 9. At lower cooling rates, a uniform and continuous surface layer is formed, with the L phase appearing only occasionally and not in colonies as observed before.
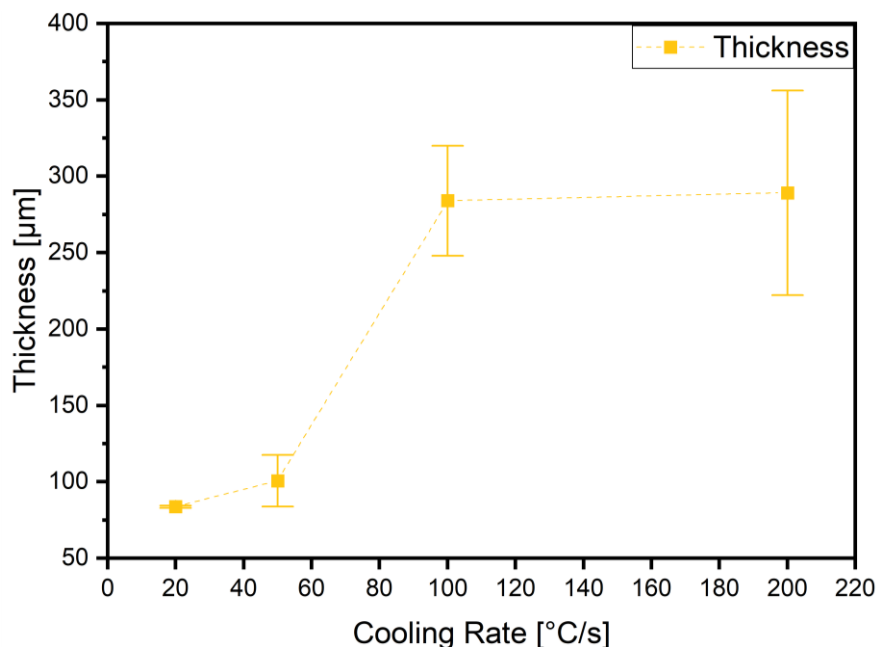
Figure 9: Thickness progression of L-phase affected zone within the microstructure of the samples at different cooling rates. With a heating rate of 3°C/s a holding temperature of 1200°C and holding time of 60 min.

However, four different microstructure types could be examined. With the first type A (Figure 10), being without any L phase. The microstructure contains a martensitic structure, with acicular martensite formation, as usually found in fast cooled Ti-6Al-4V samples. This occurred in a sample where the annealing took place at 950°C for 45 min in air with an accelerated cooling with N_2 gas of 200°C/s. The β transus temperature (T_β) in conventional Ti-6Al-4V is, depending on the exact chemical composition, about 995°C [1]. Therefore, this heat treatment was made within the (α+β) phase field, as at 950°C still 50% of β phase can be found within the sample [28]. This indicates that L phase appears especially when the sample is annealed above T_β.

As a second type B (Figure 11 and Figure 12), a microstructure with a coarse L phase was determined. This type can be found in every sample in respect of the first heat treatment step, where the temperature was altered above T_β. However, with increasing temperature the zone, where the L phase appears, is expanded, which can be nicely seen in Figure 11 and Figure 12.

Figure 8 indicates an increase in the thickness of the L phase affected zone at a holding time of 60 min. By optical analysis it was observed that not even the zone has grown, but also the single L phase precipitation itself in size, see also Figure 13. Accounting as proof that these parameters are favorable for L phase growth. Additionally, this is the confirmation that the appearance of this phase can be significantly modified.

a)

100 µm

b)

100 µm
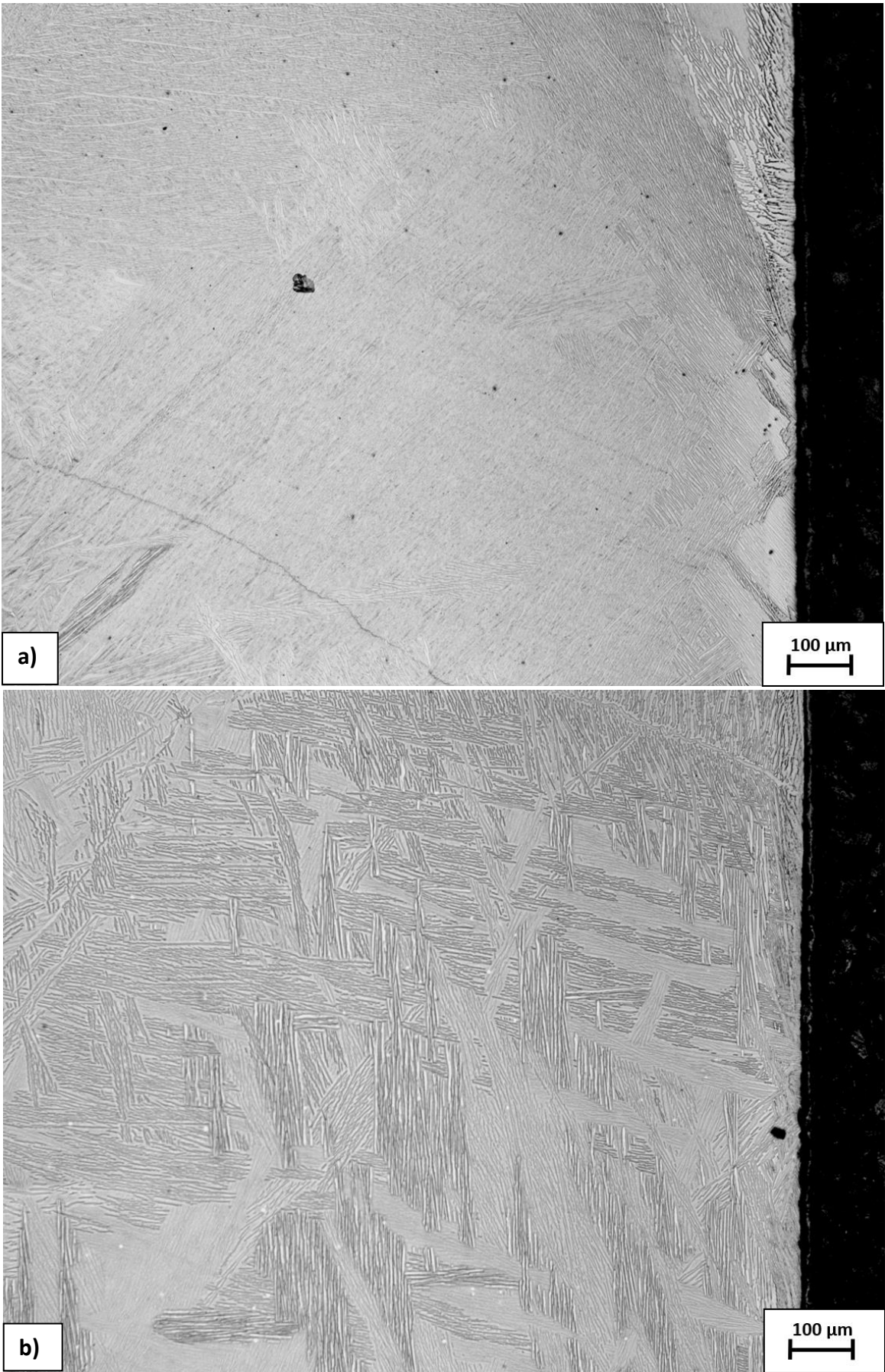
Figure 10: LOM images of a microstructure as seen on a sample with annealing under T_8. No visual appearance of L phase. Both a) and b) are originating from the same heat treatment (950°C for 45 min and a cooling rate of 200°C/s). This microstructure was declared as type A.
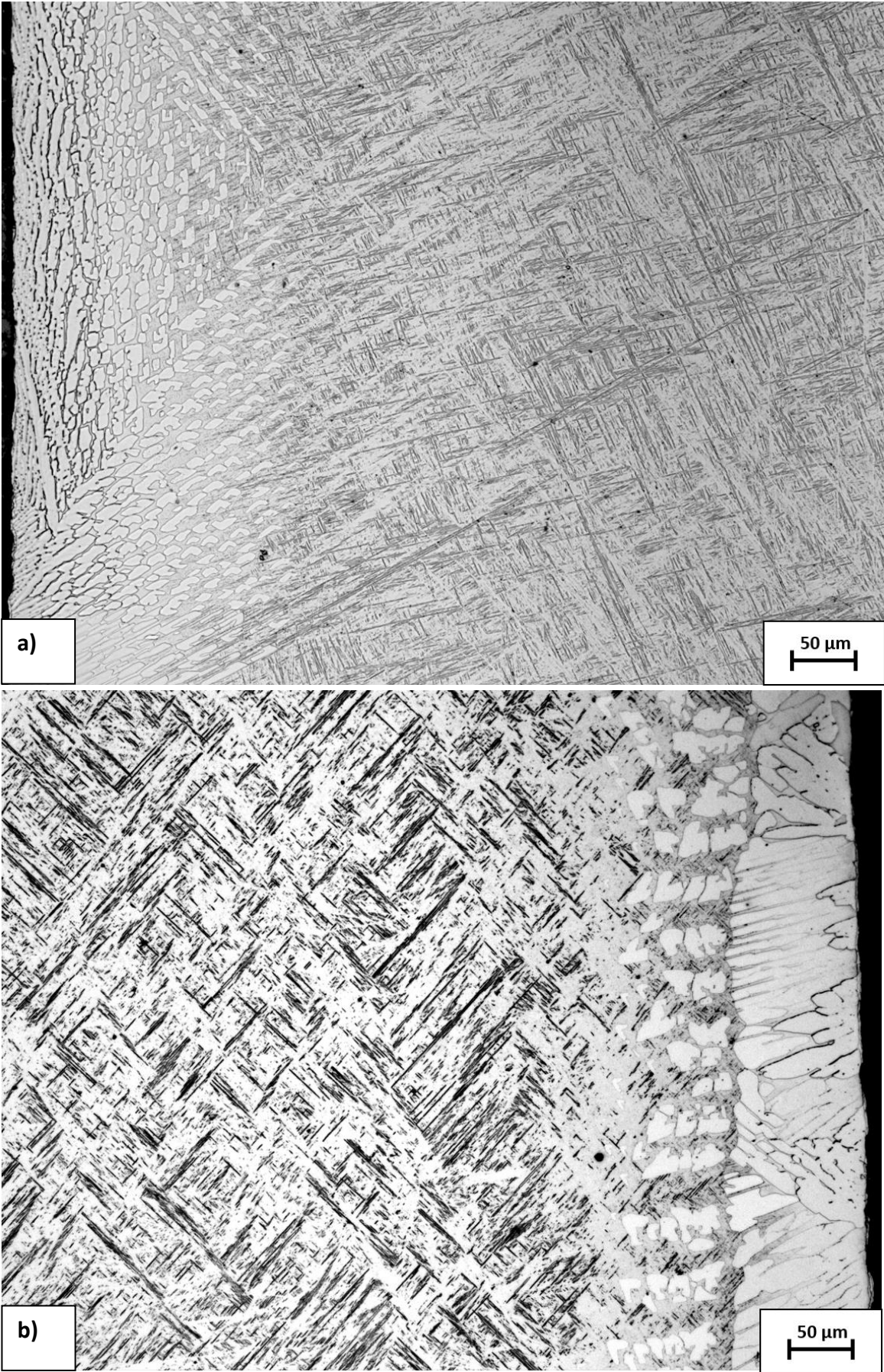
Figure 11: LOM images of the coarse L phase in the course of a β annealing. Annealed for 45 min at a) 1000°C and b) 1100°C and a cooling rate of 200°C/s. This microstructure was declared as type B.
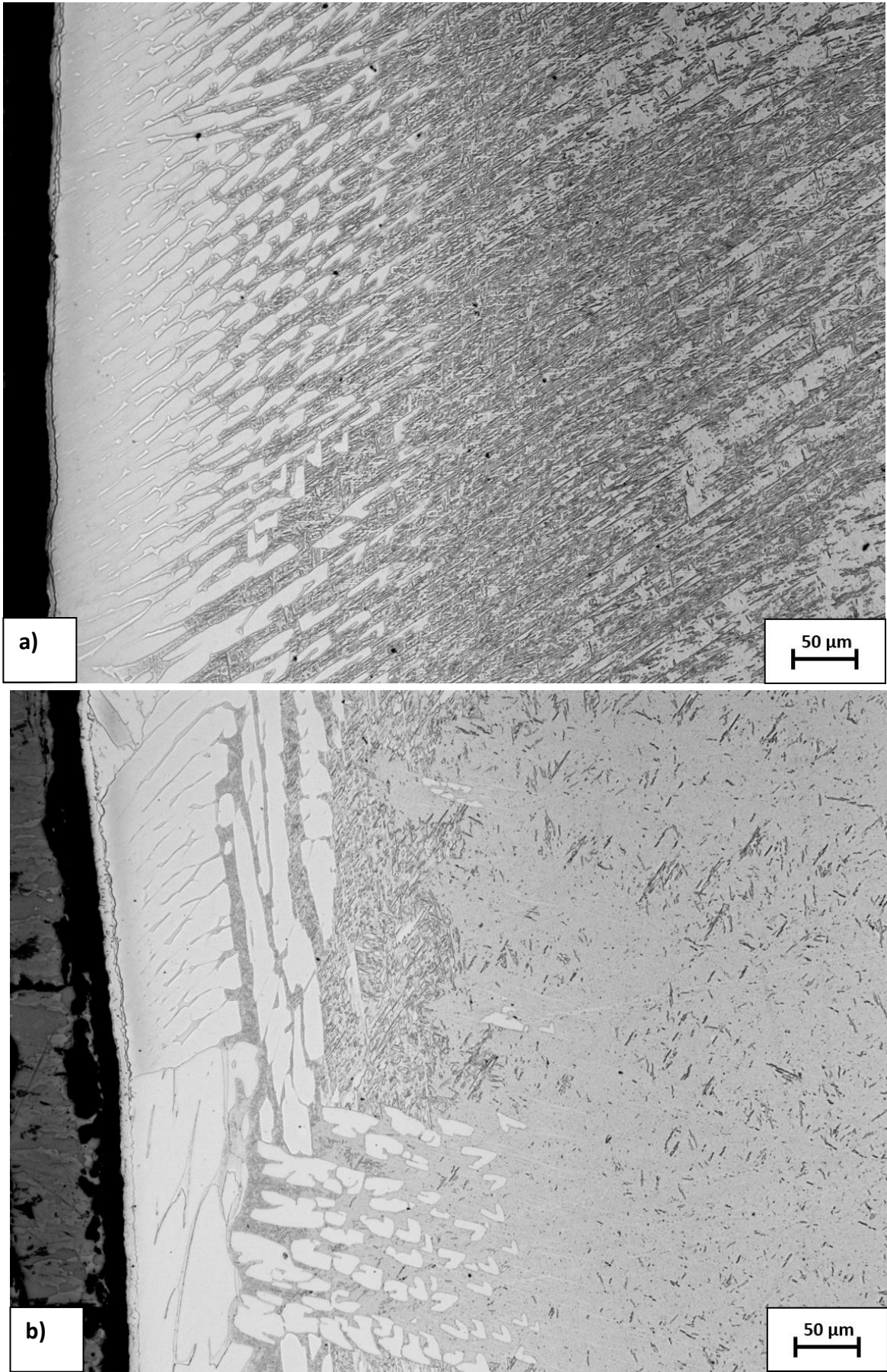
Figure 12: LOM images of a coarse L phase in the process of a β annealing. Annealed for 45 min at a) 1150°C and b) 1200°C with a cooling rate of 200°C/s. This microstructure was declared as type B.
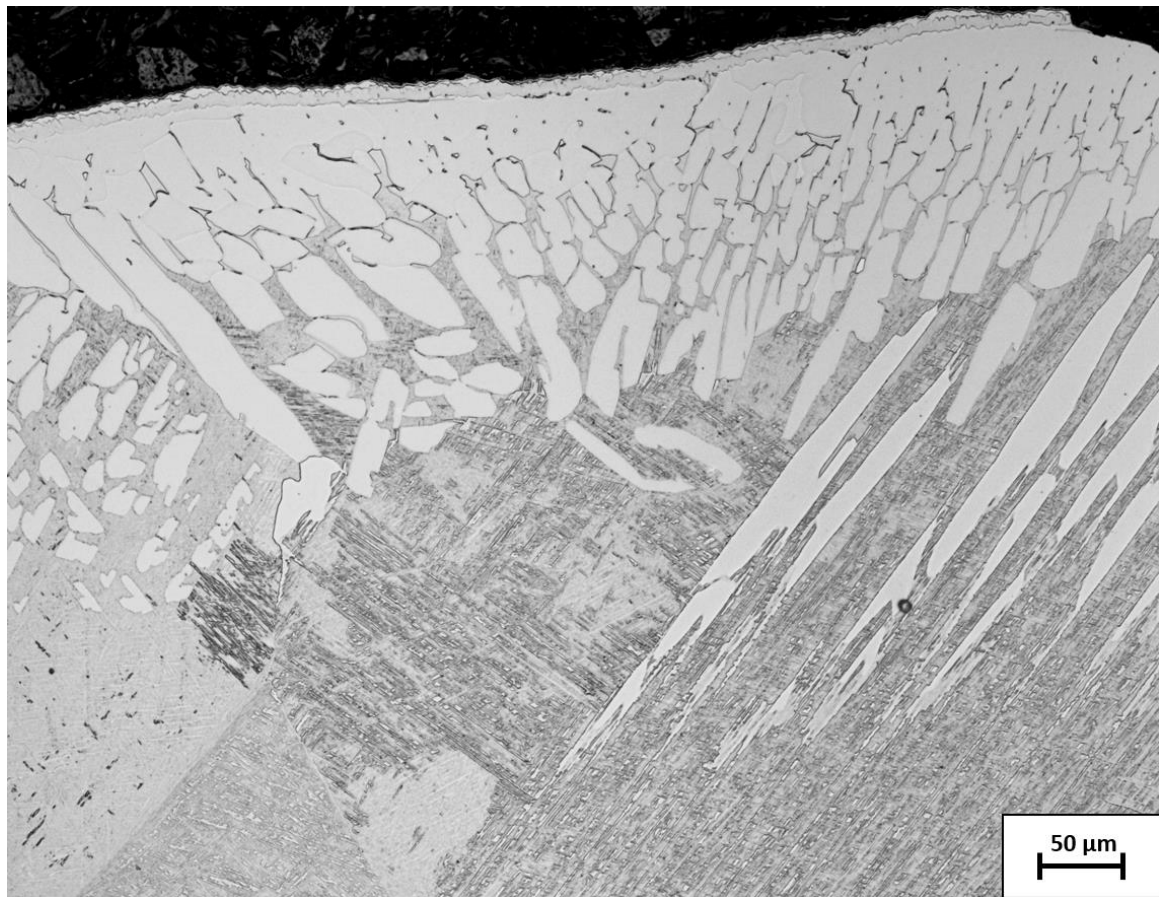
Figure 13: LOM image of a coarse L phase in the process of β annealing. Annealed for 60 min at 1200°C with a cooling rate of 200°C/s. An increase in size of the α phase precipitation is observed as well.

Continuing with the third type C microstructure (Figure 14), the shape of the L phase transformed into a more stem-shaped one, compared to the shapes A and B, seen above (Figure 11, Figure 12 and Figure 13). These stem-shaped phases are frequently visible in samples which were exposed to holding times of over 60 min, thus slightly longer held at higher temperatures. These samples have a nearly continuous edge zone in common and directly behind this zone the partly stem-shaped L phase is observed. It should be said that in some cases the origin of the stems appeared to be within the edge zone itself (Figure 14).

As the last type among the found microstructures, type D (Figure 15), shows a continuous α phase zone, while the rest of it consists of acicular martensite. It has similarities with the edge zone in Figure 14, but unlike type C, there is hardly any L phase found next to the continuous edge zone. If there is any found, however, it is situated right next to the edge and singularly. The optical analysis of type D indicated that it is possible to modify the L phase within the microstructure in that manner, that it becomes stabilized close to the edge of the specimen at a thickness of around 50 µm, by forming a continuous zone instead of distributed precipitations. This behavior was observed only for samples which received a heat treatment with different cooling rates, between 15°C/s and 50°C/s. Examples of this type D microstructure can be observed in Figure 15.
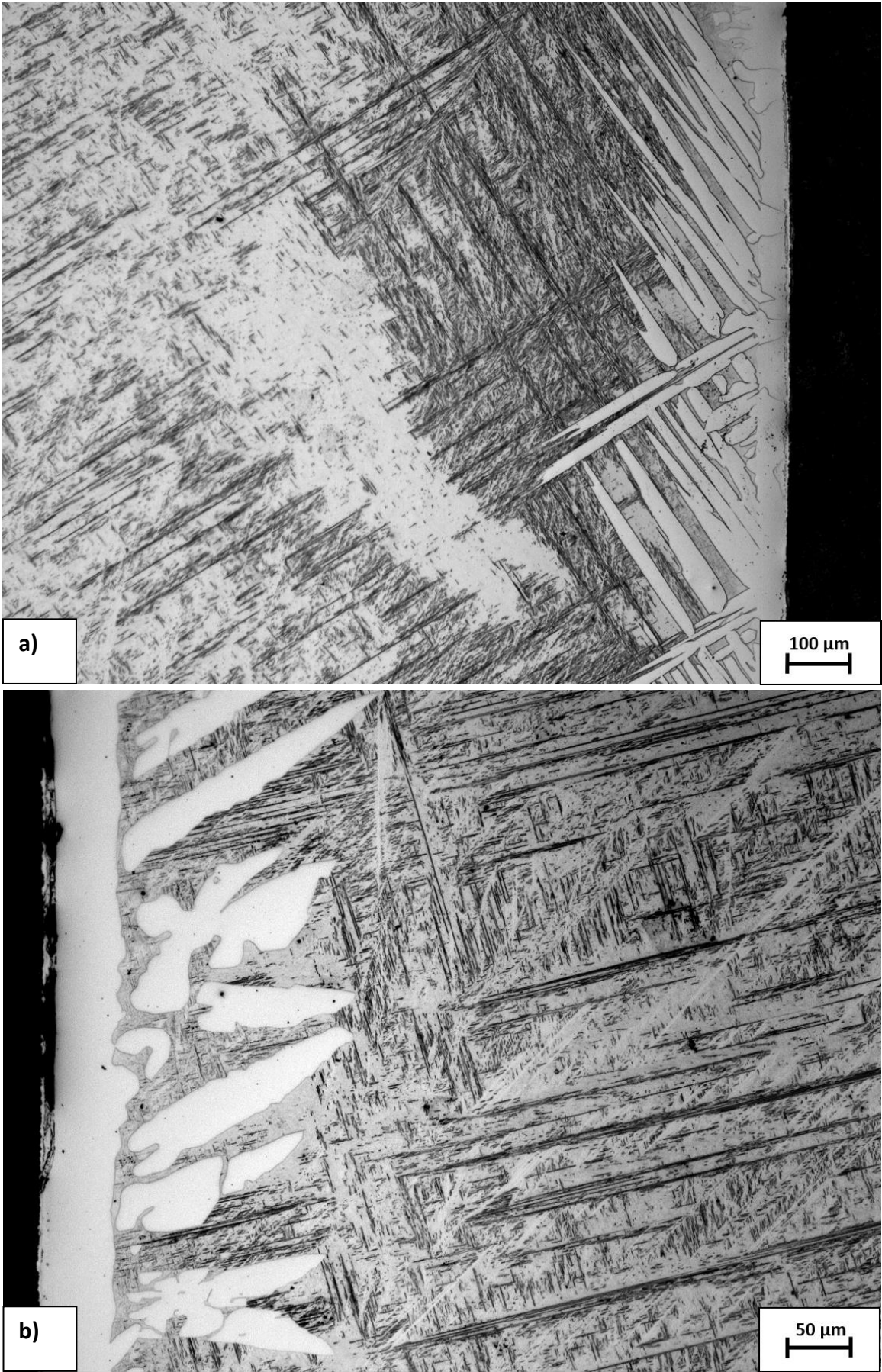
Figure 14: LOM images of a stem-shaped L phase in the process of β-annealing. Annealed for a) 75 min and b) 90 min at 1200°C with a cooling rate of 200°C/s. Note the nearly continuous edge zone. This microstructure was declared as type C.
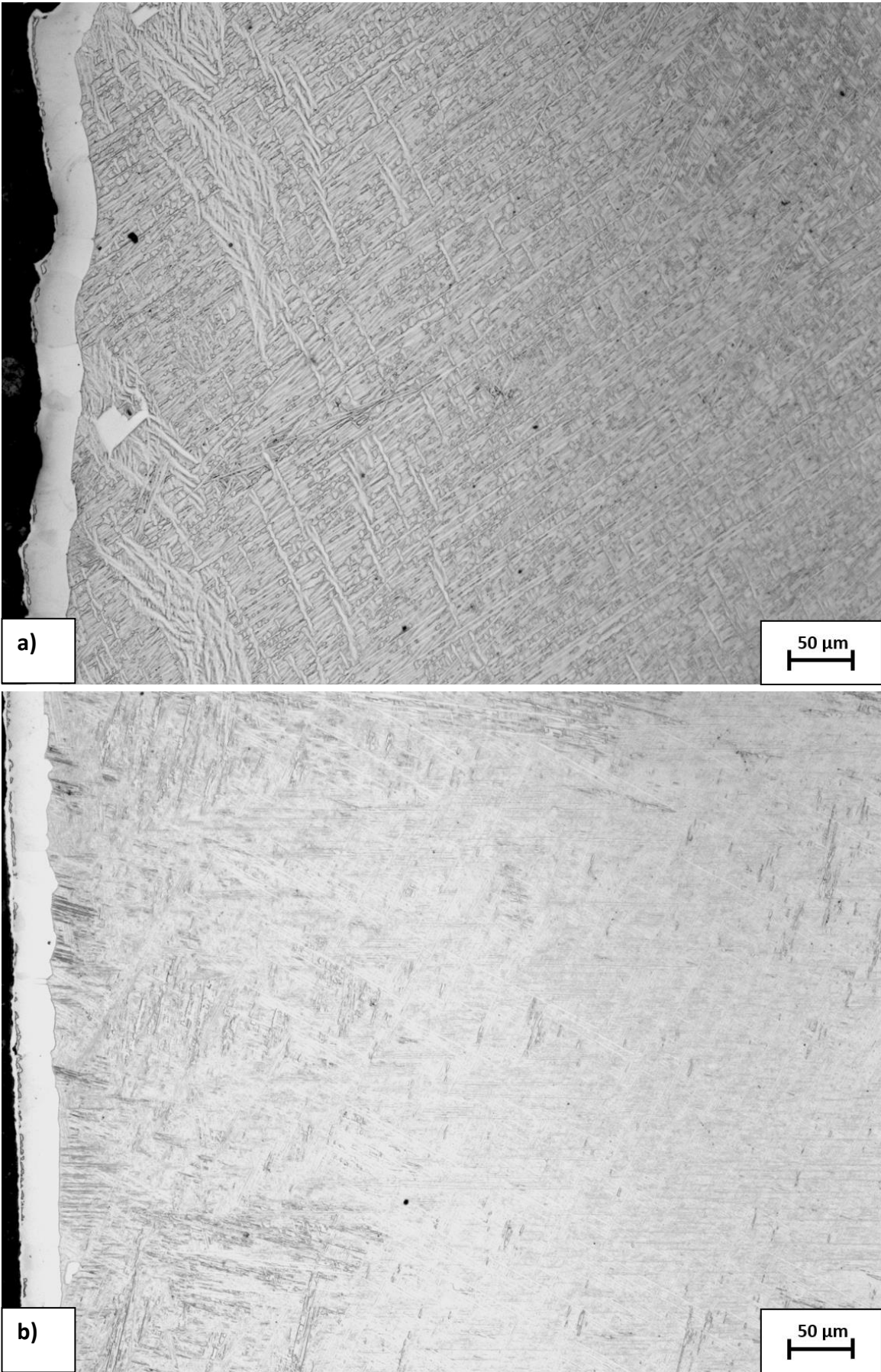
Figure 15: LOM images of a continuous edge zone with isolated L phase in the process of a β annealing. For annealing at 1200°C for 60 min and at cooling rates of a) 20°C/s and b) 50°C/s. This microstructure was declared as type D.

The formation of a continuous surface zone is well depicted in Figure 9 and indicates a transformation of type C and D between 100°C/s and 50°C/s, thus depending on the cooling rate. However, in Figure 15 a) a single L phase precipitate is found next to the edge zone. The single phase exists within an area, which is surrounded of coarsened α lamellae. This indicates that the L phase could act as a starting point for the growth of α lamellae into the sample, while being situated in a region of clustered α phase stabilizing elements during β annealing. If in addition the thickness values of the continuous zones are measured, the results for the mean values can be seen in Table 2.

Table 2: Measured thickness of continuous edge zone with standard deviation.

Sample [°C/s]	Thickness [mm]	Standard deviation [mm]
50	0.029	±0.00118
20	0.033	±0.00205
15	0.034	±0.00537

A growth of the continuous edge zone within the microstructure of type D is observed. This growth correlates with the fact that due to lower cooling rates, thus longer exposure within the β-phase field, the thickness of this continuous zone is increased, forming the alpha case eventually.
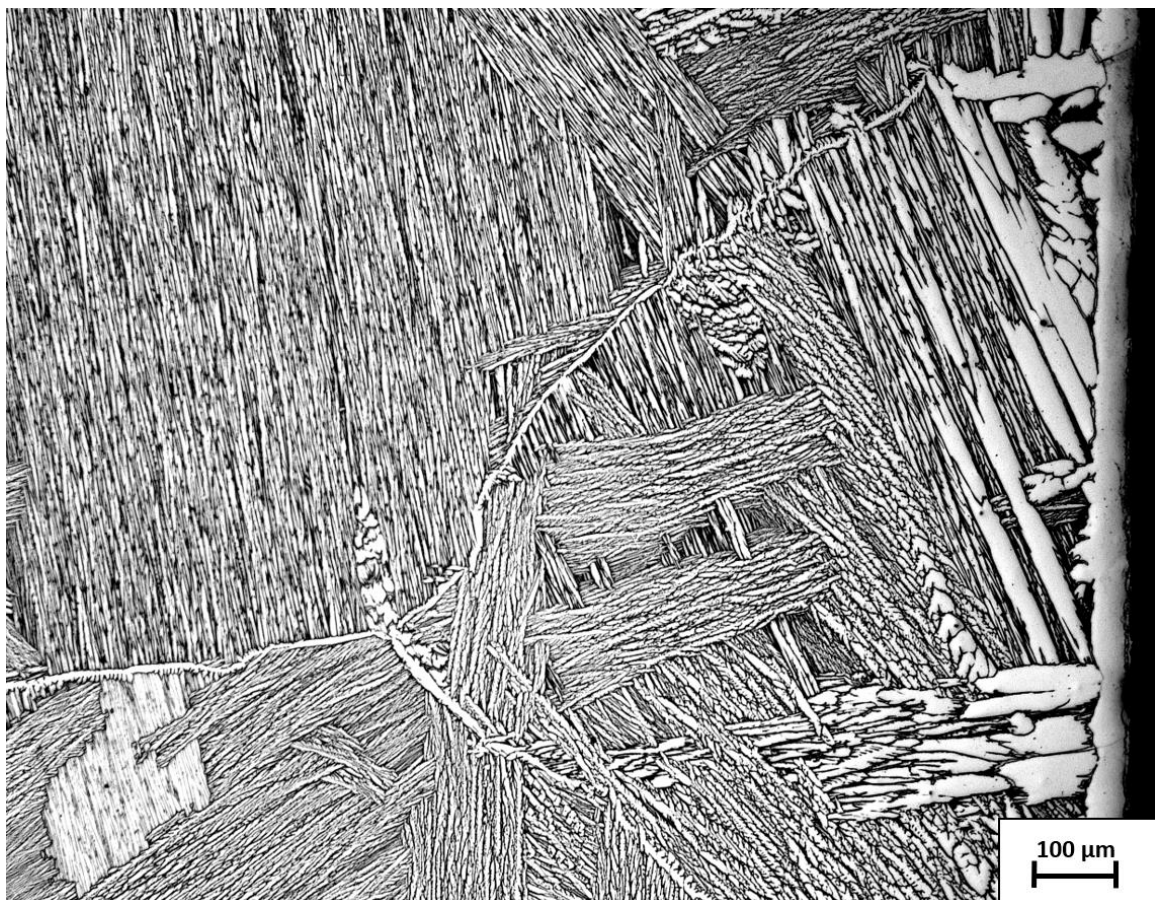
Figure 16: LOM image of a sample which was held for 60 min at 1200°C with a cooling rate of 1°C/s.

Compared with the LOM analysis of the sample with a cooling rate of 1°C/s (Figure 16), the lamellae are now the dominant feature of the microstructure, still containing L phase next to the edge. The existing L phase, however, appears to fade into the typical lamellar shape. This behavior coincides with what can be seen in Figure 15a. In this figure it becomes visible on why the differentiation between L phase and lamellae is not intuitive and was therefore excluded from Figure 9.

In general, it can be said that the phase only appeared in samples, which were β annealed in an air environment, by comparing Figure 10 with Figure 11 for example. If comparing these figures, it should be mentioned that, at 950°C the microstructure consists of 50% α phase and 50% β phase [28]. Yielding to the assumption that at this temperature, sufficient α phase exists where O can diffuse, prohibiting the formation of L phase. Therefore, the sample, with heat treatments above 950°C, were exposed to O in the more diffusive β phase. Yielding to an assumption that O is stabilizing this L phase in particular, forming an L shaped obstacle within the microstructure. Due to its size from 10-100 µm it can easily be seen within LOM. However, these microstructural obstacles grow in a certain direction, what seems to have resemblance to the BOR. In Figure 16 a change of shape of the L phase into α laths can be observed, indicating that the L phase is subjected to the BOR and therefore growth can happen along the twelve directions. The growing directions, as it was stated in Chapter 1.3, are following a 60° angle according to the BOR, therefore the L phase should show a similar growth behavior. However, further analyzation was made to proof this behavior. In Figure 11 and Figure 12, type B of the microstructure is seen, where a coarse L phase appears. This type occurs with rising temperatures in deeper depths of the samples as seen in Figure 7 with a significant rise in depth at 1250°C. On this sample, L phase occurred even in the middle of the specimen, indicating that growth of the L phase was at some locations at least beyond the 400 µm, which had been removed due to the grinding process. The depth of the phase within the 1300°C sample had the same phenomenon with L phase being visible all over the specimen section. This shows that with rising temperatures during β annealing, L phase and other α structures continue to grow within the microstructure. By setting the holding time up to 60 min and above, the coarsening of the phase is observed. With Figure 13 showing type B of the L phase at a heat treatment for 60 min at 1200°C, yielding to the revelation of stem-shaped L phase at longer exposure times in Figure 14, this being the microstructure type C. Leading to the assumption that with longer holding times, L phase is merging into a more stem-shaped form and in Figure 8 it can be seen that, due to this merge, the depth of the zone where L phase can grow is decreasing. Forming a more continuous edge zone as well, compared to the coarse zone of type B seen in Figure 11, Figure 12 and Figure 13. Indicating the stem-shaped L phase as a diffusion path for O influenced α phase.

By altering the cooling rate this effect can be increased, forming a continuous edge zone with little to none L phase crystallites found in the microstructure (Figure 15). Note that by lowering the cooling rate, the specimens had a significantly longer exposure time within the β phase field. While the effect of a cooling rate of 100°C/s is marginally little, due to an additional 2 s within the β phase field, compared to the usual 200°C/s cooling (1 s), the effect is not shown. However, the microstructure of the sample with this cooling rate (100°C/s) rather shows stem-shaped characteristics[1]. At cooling rates of 50°C/s, 20°C/s and 15°C/s (4 s, 10 s and 13 s additional exposure time in the β phase field while cooling) a highly continuous edge zone is forming. Amplifying the effect above by dissolving the L phase within the microstructure and forming the edge zone, this is assumed due to the results shown of type B. As with a cooling rate of 200°C/s, the microstructure is deprived of the ability of diffusion, hence the L phase is disabled of dissolving. This continuous zone was found to be approximately 30 µm in thickness (Table 2). Comparing these values with the, up to, 350 µm thick zones occurring within many samples, it can be said, that a sharp transformation from a coarsened, widened zone into a continuous, small zone was performed.

The described processes indicate that an α phase is able to be stabilized at temperatures above T_β ($T_\beta \approx 995$°C). A thermodynamic calculation with ThermoCalc [29, 30] made for the given chemical composition, the α phase can be stabilized up to 1250°C with an O content of 1.5 wt.% in thermodynamic equilibrium. T_β is therefore elevated to these temperatures, however, the results state, the stabilized α phase might in fact consist of α_S phase, in 32 vol.% within the microstructure. Yielding to the assumption that the found L phase, could be α_S phase, stabilized by O and supported by 6 wt.% Al. According to the LOM images, 32 vol.% of L phase are a reasonable assumption, as the phase is concentrated at the surface area only and an O gradient had to be taken into account. However, to get an approximation of the O content within the microstructure, deeper investigations are necessary. In addition, it can be observed that with longer exposure times above T_β, not only the L phase is coarsening but also the edge zone is transforming. A trend in forming a more uniform zone, thus the α case, is observed. By comparing Figure 11 and Figure 12 with Figure 14 and Figure 15, the transformation of this edge zone can be observed. A trend can be exaggerated by cooling with lowered cooling rates as mentioned above.

Due to its appearance in the LOM and the fact that the samples were exposed to O at elevated temperatures, it is assumed that the L phase is in fact an α phase, which is stabilized by O to temperatures up to 1300°C[2]. Additionally, the geometric alignment of the L phase has similarities with the martensitic alignment, which is known to follow the BOR. Therefore, as

---

[1] Illustrations of this heat treatment can be seen in the appendix.
[2] In this thesis, the maximum annealing temperature of the heat treatments was 1300°C.

the next step, the microhardness measurements, the diffusion analysis and orientation relationship of the L phase are discussed. A quantitative proof shall be found to state whether O could diffuse into the observed depths.

3.2. Microhardness testing

To gain even further insights into the properties of the L phase a microhardness study was made. In order to find a proof of an increase in hardness of the L phase within the microstructure due to O influence. Therefore, the microhardness, HV0.05, was measured according to Vickers as already described in Chapter 2.3. A deeper investigation of the four microstructure types, found within the LOM, was made.

Due to calibration issues of the fully automated hardness testing machine, the indents were not exactly in the desired positions, leading to an unsteady distance of the indent rows from the surface. In some cases, this circumstance led to missing the outer surface zone explaining the different distance values in the following graphs. Due to the risk of breakage of the brittle surface zone by indentation, the distance of the anticipated indent from the surface should be adapted, to prevent distortion of the results through breaking the material of the indentation region.

To give a proper overview of the microstructure types, illustrations of the hardness progressions were made, starting with the microstructure type A. The associated tables, which were used for calculation can be found in the Appendix (Chapter 7). In Figure 17 the hardness progression of a specimen with no L phase is illustrated. This sample had no β annealing due to a maximum heat exposure of 950°C. As with the exponential fit, the strong decrease in hardness from the surface to the sample middle is seen. The hardness values are situated between 400 HV and 750 HV, which show an average increase, expected due to an annealing process in an air environment and diffusion of O. The change of the microstructure to lamellar structure in the surface region with fine α lamellae, as seen in Figure 10, might also explain the hardness course of this sample. However, if compared to other specimens, which received a β annealing, the hardness increase is lower. This correlates with the LOM images, as there is no L phase established in the sample.
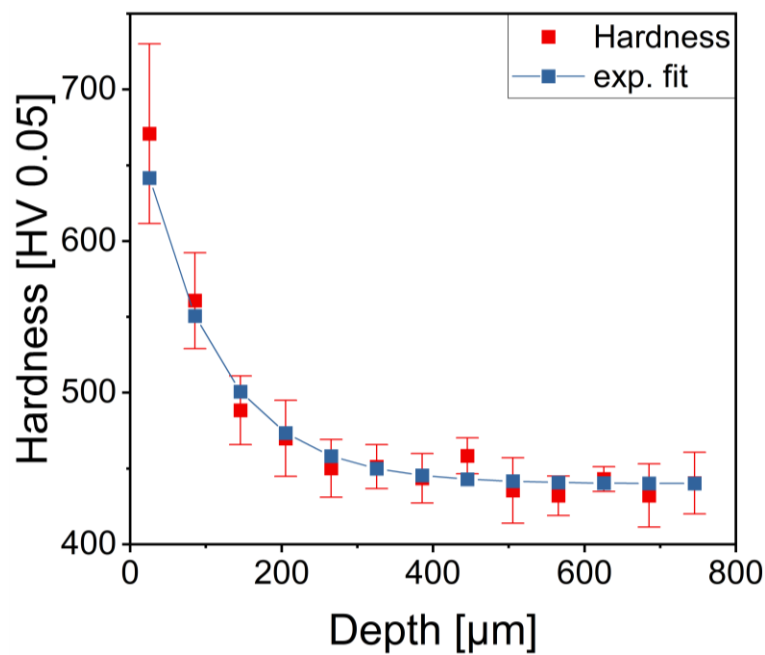
Figure 17: Hardness progression of type A microstructure with an exponential fit, annealied 45 min at 950°C in an air environment with a 200°C/s cooling rate in N_2.

For type B, according to the LOM pictures, coarse L phase precipitates are present. Based on the assumption that the L phase is in fact α phase stabilized by O, high hardness values are to be expected. In Figure 18, the microhardness results of a type B microstructure are shown, and a significant hardness increase in the surface area can be seen, when compared to type A. If Figure 17 and Figure 18 are compared, the surface hardness increases by 300 HV, to over 1000 HV (type B). Even though a rapid decrease can be seen, the ground hardness of this sample is still around 600 HV compared to 450 HV, an increase of up to 150 HV, as can be seen in Figure 18. Meaning that with annealing in the β phase field, and subsequent quenching, both surface and ground hardness can be altered to higher values.
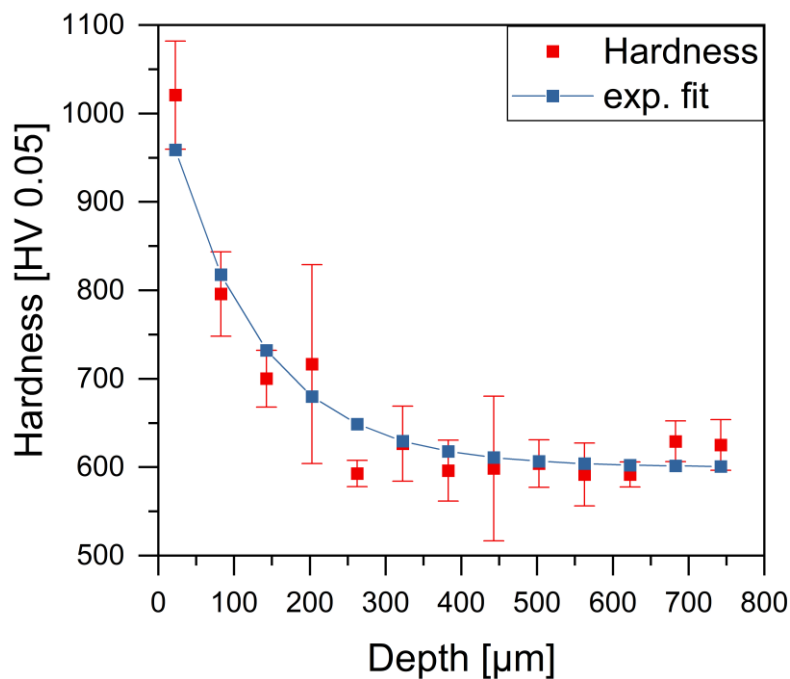
Figure 18: Microhardness of microstructure type B, annealed for 45 min at 1200°C in an air environment with a cooling rate of 200°C/s in N_2.

In the measurements for type C, where a stem-shaped L phase formation is observed, an increase, likewise type B, is visible as well, as can be seen in Figure 19. However, a decrease of the hardness values occurs within a shorter distance compared to type B, as the area where L phase occurs, decreases, as can be seen in Figure 19.
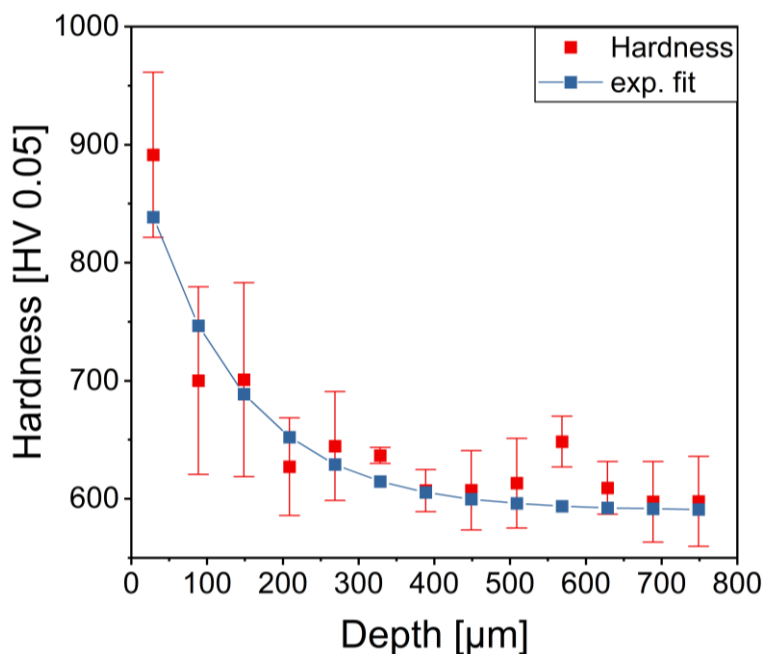
Figure 19: Microhardness of microstructure type C, annealed 90 min at 1200°C in an air environment with a cooling rate of 200°C/s in N_2.

However, the ground hardness is on the same level of around 600 HV. The slightly faster decrease can be seen if the hardness values of a distance of 100 μm and 200 μm are compared, i.e. Figure 18 and Figure 19. As with type B (Figure 18), at a distance of 100 μm a hardness

value of around 800 HV is achieved, whereas for type C (Figure 19) a hardness value of around 750 HV is achieved. Leading to a difference of 50 HV between these microstructures. This trend continues at a distance of 200 μm, with type B achieving slightly below 700 HV, and type C around 650 HV. Both types achieving the ground hardness of around 600 HV at a distance from surface of at least 400 μm. The heat treatments for these specimens in particular, distinguish in the different holding times at 1200°C, with type B of 45 min and type C of 90 min, meaning a doubling of the holding time.

The last microstructure, type D, is characterized with a continuous edge zone, with no L phase next to it. According to the assumptions made in the LOM study, this edge zone was built up due to merging of the existent α stabilizers on the surface. Meaning that this type must have a high amount of O dissolved in regions next to the surface of the specimen, high hardness is expected. Nonetheless, in Figure 20 a significant hardness increase can be observed. With a distance of 13 μm from the surface for the first indentation row, it was possible to take a microhardness measurement in the immediate continuous edge zone. An averaged hardness value of 1308 HV was measured, yielding to a significant enhancement of the hardness compared to other tested values. A steep decrease immediately after the continuous edge zone can be observed as well, with a difference of up to 700 HV within the first 120 μm, leading to a hardness of around 600 HV at greater distances from the surface. The hardness over depth mirrors what was seen in the microstructure of this sample, a sharp zone of a brittle phase is formed. In addition, the trend observed for longer holding times, with decreasing hardness values for smaller distances, continues.
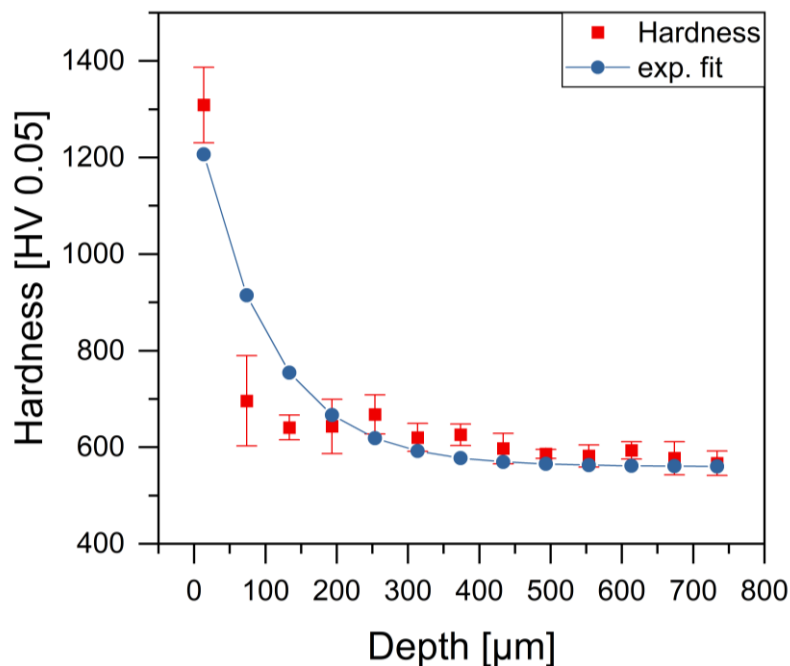
Figure 20: Microhardness of microstructure type D, annealed 60 min at 1200°C in an air environment with a cooling rate of 50°C/s in N_2.

During this microhardness study, further insights of the precipitation behavior of the L phase could be accomplished. With the samples which were held for 45 min at different temperatures within the β phase field in an air environment and cooled with N_2 with 200°C/s, the growth behavior of the L phase influenced zone could be depicted and its hardness increases due to enhanced diffusion. As mentioned in the LOM-study before, the zone, within the L phase occurred is expanding with higher temperatures. In Figure 21, this effect can be seen due to an increase of hardness at each heat treatment steps. It also shows that with an increase of the temperature, the hardness values near the surface are increasing as well, which is due to a higher O diffusion. It also shows the extensive zone of the L phase within the specimens.
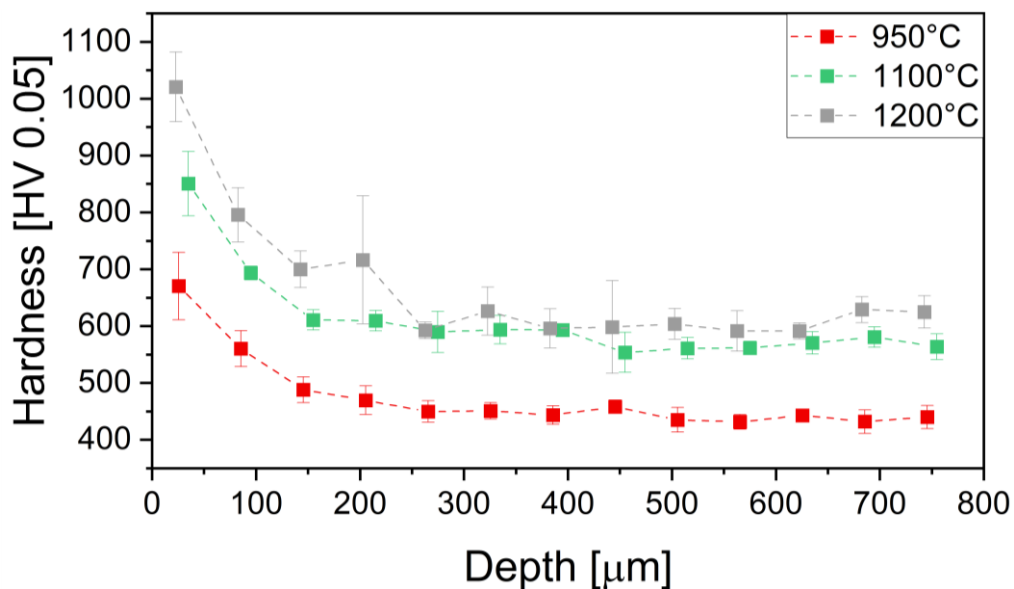
Figure 21: Microhardness measurements for different temperatures at 45 min in an air environment with cooling at 200°C/s in N_2.

Starting from 950°C holding temperature, where a hardness increase near the surface can be observed, however, this is due to the finer lamellae structure on the surface. The ground hardness is on a level of around 450 HV. If increasing the holding temperature above $T_β$, a general increase of hardness is observed. The ground hardness of the depicted two heat treatments with β annealing, show no significant difference and level themselves at around 600 HV. The surface hardness, however, shows a significant difference, which is increased due to elevated holding temperatures. This study suggested that with increasing annealing temperatures, surface hardness is increased as well, whereas the ground hardness stays the same for specimens, which were heated above $T_β$.

Another fact observed in this study was the hardness difference between the samples with altered cooling rates. As mentioned above, these samples show the formation of a continuous edge zone, with very little to no L phase next to it. Uniform formation of α case is established, by longer exposure at a temperature in the β phase field, however, a strong decrease of the

hardness is observed. This agrees with the LOM study, as α phase stabilization only seems to appear in a continuous surface layer and therefore achieving higher hardness values, as can be seen in Figure 22.
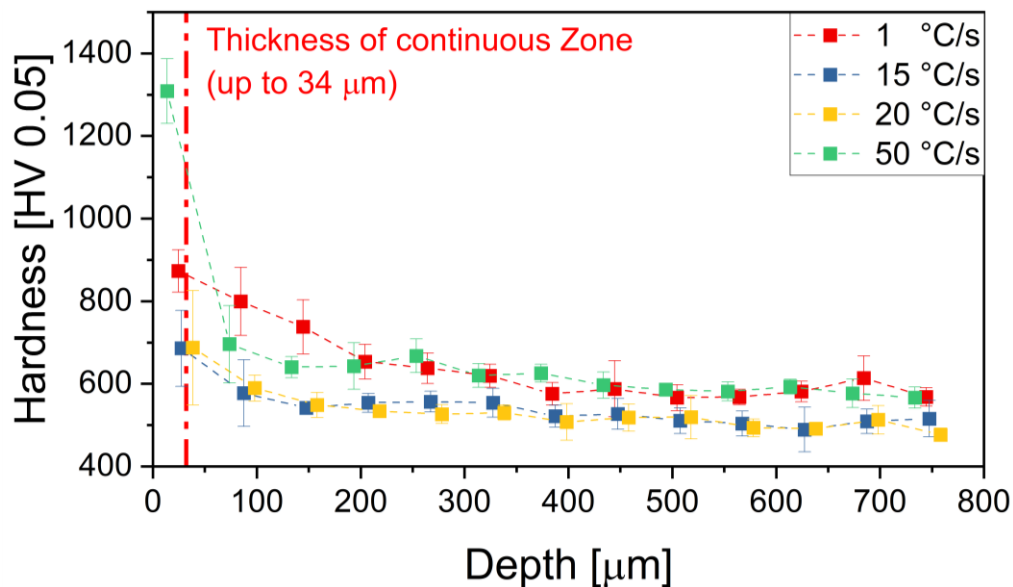
Figure 22: Microhardness measurements for samples which were exposed to 1200°C at 60 min in air and cooling with different cooling rates in N_2.

In Figure 22 the thickness of 34 µm of the continuous zone is marked as well (see Table 2 for further information), making it more understandable, where high values of hardness are to be expected. As can be seen, only at the measurement of the sample with 50°C/s, it was possible to indent an entire row inside the thin continuous zone. The indents for the other samples were partly taken next to this zone, explaining the huge differences for near-surface mean values. However, the ground hardness values (600 HV) for these samples appear to be in the same area as for the other samples, which encountered annealing in the β phase. For the sample cooled with 1°C/s, however, an almost linear decrease can be observed. Here no β annealing took place, but instead thick α lamellae were established, which were indented eventually. The other measurements, with cooling rates of 15°C/s, 20°C/s and 50°C/s, and the according LOM study illustrate the formation of α case and the annihilation of L phase due to longer exposure and longer cooling rates within the β phase field.

A comparison of the hardness measurements for different exposure times should deliver an additional insight of the growth behavior of the L phase. In Figure 23, a slight decrease of the hardness for specimens with higher holding times can be observed. The same can be seen for shorter holding times. As with short exposure times the L phase affected zone can only grow to a limited distance, as it is stopped by the applied cooling. Hence, less O can diffuse into the material, bounding the hardness of the surface zone to lower values. However, for longer exposure times, the formation of a diffusion barrier through the coarsened L phase itself, might be the reason for lower hardness values in the surface background. As O is prohibited

to diffuse into larger distances through this barrier. This diffusion barrier can be seen as a weaker diffusional barrier than observed for microstructure type D. As type C shows no formation of a continuous zone, but coarse stem-shaped L phase, which might resemble locally to the continuous zone from type D. This illustration suggests a maximum growth of L phase for 45 min holding time. Above 45 min coarsening occurs, hence hardness values are decreasing in a shorter distance.
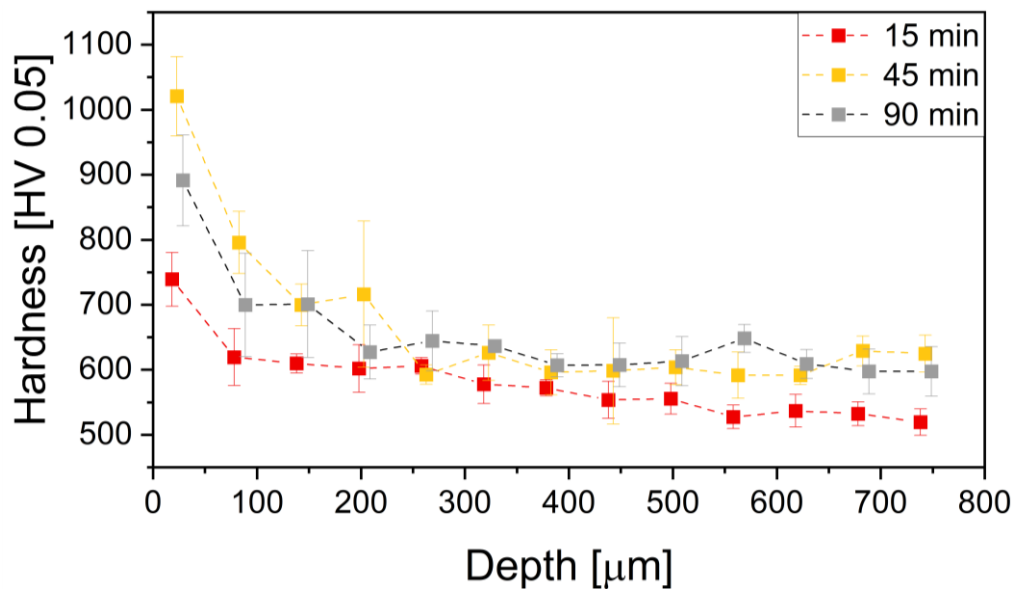
Figure 23: Microhardness measurements for samples which were exposed to 1200°C at different times in an air environment and cooling with 200°C/s in N_2.

Ultimately, it can be said that with an annealing in the β phase field, hardness can be increased by 150 HV in respect of the ground hardness. The reason for this increase might be due to the greater temperature gradient, which occurs while martensite formation. Hence, a greater distortion of the microstructure, which leads to higher hardness values. However, the hardness near the surface can be significantly increased by altering the temperatures at constant holding times (Figure 21). Yet the ground hardness seems to stay at the same level, however, the distance where ground hardness is achieved is set to higher values. Indicating a higher diffusional force, thus a higher diffusion coefficient. This means that the diffusional path is longer in samples with higher temperature exposure, hence, higher possibility of L phase development.

Nonetheless, an exponential hardness increase from sample middle to surface can be seen in all microstructure types. Even for microstructure type A, without a β annealing, which can be explained due to the formation of a fine lamellae microstructure and the annealing process in an air environment, thus the diffusion of O into the specimen. But it must be mentioned that these values are gained through a microhardness measurement, which limited in describing the local mechanical properties for small microstructural details, such as fine lamellae or precipitations. As with the size of the used indenter, an indentation into the L phase or matrix

alone could not be guaranteed. Many indents were made in a mixed area of L phase and matrix, distorting the hardness values of the L phase, the matrix and the zone between them. In an attempt to compensate this effect, an average of the values within a row of the respective indent matrix was calculated. In order to counteract this effect and receive adequate values for L phase, matrix and the zone between, a more precise testing method is needed. Therefore, an additional nanoindentation measurement was made.

3.3. Diffusion analysis

In this chapter a calculation shall be made to see whether it is possible for O to diffuse into depth ranges as seen in the previous chapter. For the used model, the diffusion coefficient is needed, which was calculated as well and is presented in an Arrhenius plot for the used temperatures in the β phase field. As shortly discussed in Chapter 2.4, there might be a correlation between an O amount in the specimen and the formation of the L phase, regarding a possible α_S phase formation. With an assumption that O follows the hardness in its course, an exponential model can be established which predicts the O content in the sample.

Starting with the calculation of the diffusion coefficient, here the mathematical process is based as described in Chapter 2.4. For the diffusion calculations, however, the microhardness of the semi-infinite distance from the surface is needed, for which the ground hardness was used (see Chapter 3.2). As ground hardness, the hardness within the sample middle was used. As with a distance from over 720 μm from the surface, this is a sufficient approximation of the ground hardness. The surface hardness was estimated by using an exponential progression based on the measured hardness values and their distances from the surface. With these values, equation 7 can be used to calculate the hardness term of the equation. By using the distance of the indent and the holding time, the second term of (7), the error function term, can be calculated. With an alteration of the diffusion coefficient D, a fit can be expressed, which suits the exponentially fitted course of the hardness term best.

For better illustration purposes, a demonstration calculation (Table 3) of a sample which was heated up to 1200°C, held for 45 min at this temperature, in an air environment and subsequently cooled with N_2 at 200°C/s, shall be made. The mean hardness values per row were calculated as it has been described in Chapter 2.3.

Table 3: Example of a tabular calculation for equation 7, row by row according to the measuring pattern. For a specimen which was held for 45 min at 1200°C in an air environment and quenched with a cooling rate of 200°C/s in N_2 gas.

Indent row Nr.	Hardness [HV]	Depth [mm]	Hardness term	Diffusion term
1	1020.897	0.023	0.02872	0.11546
2	795.8797	0.083	0.54798	0.40397
3	700.1499	0.143	0.76889	0.63982
4	716.5015	0.203	0.73115	0.80637
5	592.8143	0.263	1.01658	0.90798
6	626.4918	0.323	0.93887	0.96152
7	569.1403	0.383	1.07121	0.98590
8	598.4906	0.443	1.00348	0.99548
9	604.024	0.503	0.99071	0.99874
10	591.6287	0.563	1.01932	0.99969
11	591.7491	0.623	1.01904	0.99994
12	629.1923	0.683	0.93263	0.99999
13	625.1151	0.743	0.94204	1.00000

As for the best fitting a diffusion coefficient for this heat treatment, seen in Table 3, in particular, $D=4.5*10^{-12}[\frac{m^2}{s}]$ was found[3]. For a more accessible illustration, Figure 24 shows the hardness term and the error-function term within a diagram over the depth after applying the best fit parameters. Additionally, an exponential fit was added for the hardness term, as an auxiliary tool for finding the best fitted diffusion coefficient. As with the difference between the exponential fit and the error-function term, the diffusion constant can be altered to gain the best suited model.

With the knowledge of the diffusion coefficient, however, the average diffusion path of O in Ti-6Al-4V can be calculated with equation 4 in Table 4. This can be compared to the average thickness of the L phase affected zone as seen in Figure 7, Figure 8 and Figure 9.

---

[3] Note that the remaining tables with calculations are found in the appendix together with the calculated hardness values.
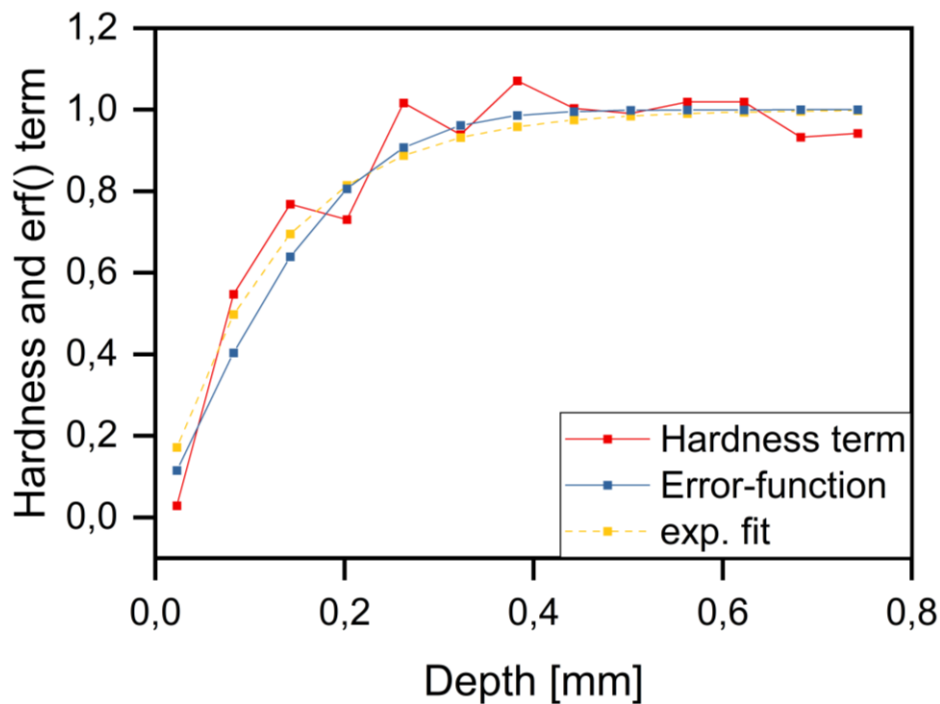
Figure 24: Hardness and error function term over depth, including an exponential fit for hardness values.

In the following in Table 4 the parameters of the heat treatments used are listed. In addition, $\bar{x}$, which was calculated under usage of equation 4, the diffusion path according to Einstein and the measured x with its standard deviation, which was estimated via optical analyzation under usage of ImageJ as described in Chapter 2.2. The calculated $\bar{x}$ is therefore, a mathematical estimation of the distance O can reach within the sample material starting from the surface, whereas the measured x is the expansion of L phase affected zone.

Table 4: Comparison of the diffusion path as calculated and the thickness of occurred L-phase within the LOM-study.

Temperature [°C]	Holding time [min]	Cooling rate [°C/s]	Calculated $\bar{x}$ [mm]	Measured x [mm]	Standard deviation [mm]
1000	45	200	0.11	0.2210154	±0.02624032
1050	45	200	0.25	0.1967392	±0.018002
1100	45	200	0.17	0.2126272	±0.01298432
1150	45	200	0.15	0.2609912	±0.01410218
1200	45	200	0.23	0.2548162	±0.00904181
1250	45	200	0.27	>0.4	-
1300	45	200	0.36	>0.4	-
1200	**15**	200	0.13	0.09581657	±0.02204591
1200	**30**	200	0.18	0.16842714	±0.04688689

1200	**60**	200	0.25	0.289072	±0.06698473
1200	**75**	200	0.28	0.3169835	±0.003479089
1200	**90**	200	0.31	0.29882717	±0.0909762
1200	60	**20**	0.2549	0.083674	±0.00077
1200	60	**50**	0.2547	0.100631	±0.01683983
1200	60	**100**	0.2546	0.2840585	±0.03601178

Resulting in a consistent approximation of the estimated diffusion coefficients, it should be said that after a heat treatment at 1250°C and 1300°C for 45 min and 200°C/s cooling rate, L phase occurred even in the middle of the sample sections. Therefore, >400 μm as occurring depth was used. Compared to the diffusional path calculated with this model, however, this is in reach with the measurements made. But as only distorted microhardness measurements from these specimens can be made, due to their established L phase affected zone, they were excluded from further investigations. However, this shows that the higher the annealing temperature, the deeper the O influenced zone gets, hence, the wider the L phase influenced zone is. Additionally, the specimens which were exposed for 60 min at 1200°C and cooled with 1°C/s and 15°C/s in an N_2 environment, respectively, were excluded of this measurement as well, due to difficulty in differentiation between L phase and lamellae.

As for the specimens with different holding times and different cooling rates at the temperature of 1200°C, the diffusional coefficient of $D_{1200°C}=4.5*10^{-12}[\frac{m^2}{s}]$, see the example calculation in Chapter 2.4, was used again. If the calculated $\bar{x}$ and measured x values are compared, this model delivers highly accurate values for specimens, which underwent different temperatures and for those with different holding times. As it shows an average deviation of 0.07 mm for different temperatures and for different holding times 0.02 mm. However, the calculation seems to fail for lower cooling rates, delivering higher values for $\bar{x}$ than it was measured via optical analysis, as can be seen in Table 4. This might be due to the constantly changing settings, which come when having an altered cooling. As the diffusion coefficient is constantly changing during the exposed time at temperature, therefore, a more sophisticated mathematical model is required to quantify these values. Another influence on the diffusion behavior of the sample, which has to be considered, might be the decelerating effect of the already established α phase in the surface zone of the sample, namely a continuous layer.

In addition to the calculation of the diffusional path, an Arrhenius plot can be created for the O diffusion in Ti-6Al-4V by using the approximated diffusional coefficients (Figure 25). For this plot, the diffusion coefficient values from the heat treatment process with altered holding

temperatures were used. In Figure 25 the diffusion coefficients of O in Ti-6Al-4V for temperatures between 1000°C and 1300°C as calculated are shown. The diffusion coefficients are in a range between $D_{1000°C}=1.2*10^{-8}\frac{cm^2}{s}$ and $D_{1300°C}=1.2*10^{-7}\frac{cm^2}{s}$.
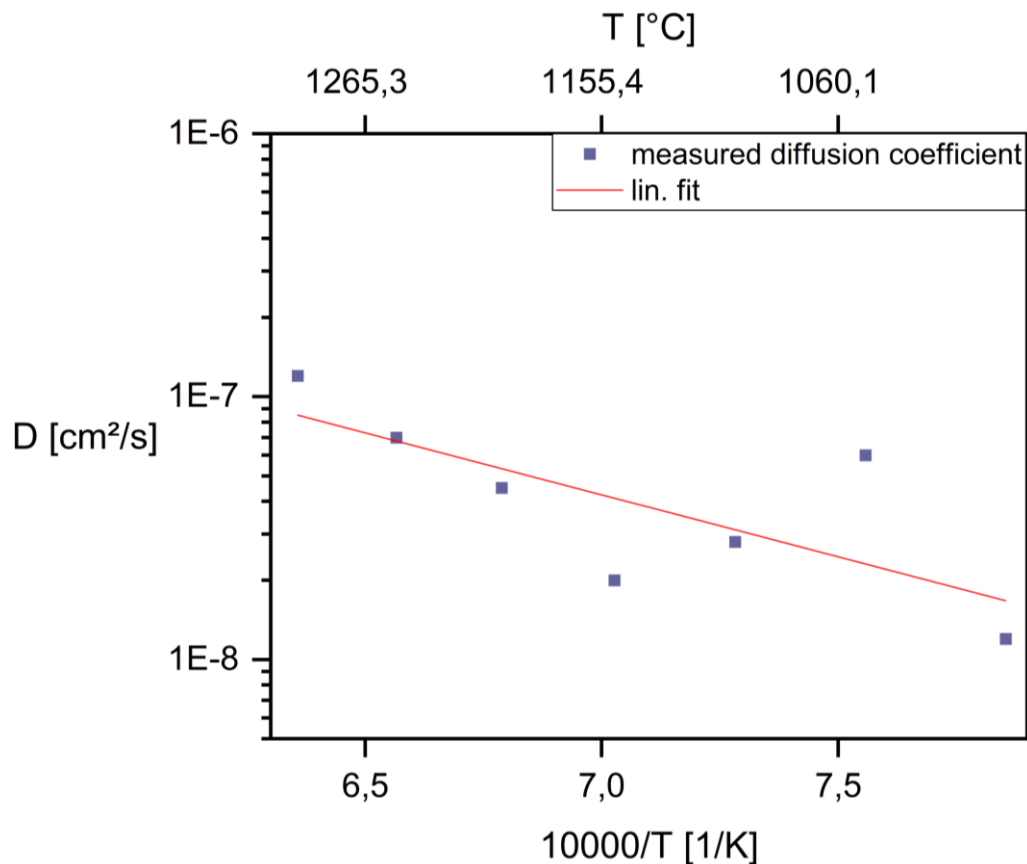
Figure 25: Arrhenius diagram of O diffusion in Ti-6Al-4V in a temperature range between 1000°C and 1300°C for a constant holding time of 45 min in an air environment and a cooling rate of 200°C/s with N$_2$ gas.

By comparing the diffusion of O in cp-Ti (Figure 5) with the diffusion in Ti-6Al-4V, the diffusion coefficient is lowered in the alloy by a factor of 10^4. Providing a proof that diffusion within the alloy is more difficult for O than within the pure metal [24]. However, in Figure 25 two estimated diffusional coefficients for the temperatures of 1050°C ($7.56\left[\frac{10000}{K}\right]$) and 1150°C ($7.02\left[\frac{10000}{K}\right]$) deviate strongly from the inserted linear fit. The reason for this might be due to the used, averaged hardness values, as there have been made only one hardness measurement per specimen. Therefore, by applying several hardness measurements per specimen, these deviations could be eliminated and additionally the approximation of the diffusional coefficient can be improved to more accurate values.

Nevertheless, it can be said that due to usage of the mathematical models according to Song et al. and Guleryuz et al. [18, 25], an indicative approximation was made. With an average abbreviation of 0.047 mm, for varying temperatures and varying holding times, of the diffusion path of O and the actual occurrence of L phase, this model is providing evidence, that in fact mainly O might be responsible for L phase appearance.

A more accurate hardness measurement might help in providing better values for this model. Because the microhardness measurements were made in just a small region of the surface area. Therefore, a bigger area scan in the course of the hardness measurement might be of help in gaining more precise results. In any case, due to the different heat treatments made by Song et al. and Guleryuz et al. [18, 25], where the samples were exposed at holding times of up to 24 h (Song) and up to 72 h (Guleryuz) and with Guleryuz studying the oxidation behavior of Ti-6Al-4V between 600-800°C, this model for quantification delivers good results in the prediction of the O influenced zone even for heat treatments used in the course of this thesis. Regardless, that the heat treatments studied in this thesis were well above T_β, hence a β annealing took place and the holding times were well below several hours with the longest being 90 min. Following the trend observed in the LOM study, the L phase appears to merge to the surface region forming coarse α phase and a continuous zone eventually. These aspects might also be an explanation, why the appearance of this shape was never mentioned in any of these papers. As seen in this work, the longer the holding times the L phase is coarsening and transforming into type C of the microstructure and type D, eventually. Indicating that L phase can be established at short annealing times with fast cooling rates. If slower cooling rates are applied, the L phase is compromised into a continuous zone near the surface, which is referred to as microstructure type D in this thesis.

The formation of a continuous edge zone might also lead to a diffusion barrier of additional O from the surface into the specimen. Which, if a mathematical model for the estimation of the thickness of the continuous edge zone is made, must be considered as well. With the assumption of being an O stabilized zone, thus having a high increase in hardness, an extremely hard surface zone can be established. This might lead to desired surface properties for new applications of this alloy.

If even slower cooling rates are applied, which lead to a diffusion-controlled phase transformation, a basketweave microstructure instead of a martensitic microstructure is the result. Instead of promoting a continuous edge zone only, coarse α lamellae and L phase are formed, as already discussed in Chapter 3.1 and this can be also seen in Figure 16. The difference is that with a diffusion-controlled process, α phase is precipitated, also without the presence of additional O.

As discussed in Chapter 3.1, thermodynamic calculations estimated 32 vol.% of α_S phase within the microstructure by a given 1.5 wt.% of O in the alloy at an elevated temperature. Making it possible for the L phase being α_S phase stabilized by O. Therefore, a proof should be made, if a weight percentage of 1.5 wt.% is possible for O near the surface of the specimens. A correlation between hardness and O content is given as seen before. However, due to the scattered growth behavior of the L phase as can be seen throughout the LOM study,

conventional microhardness measurements will lead to insufficient results. As an orientation dependence of the L phase and an O gradient within the L phase affected zone are expected. To gain better results of the observed hardness-decrease of the L phase, the results of the nanoindentation measurement can be of use, following in Chapter 3.4.

3.4.   Combining nanoindentation and EBSD

These measurements were made to get a deeper insight into the mechanical differences between L phase and the matrix of the material. As mentioned above (Chapter 3.2), an understanding of the hardness of the L phase itself is of interest. Thus, a nanoindentation can give the information needed for this, as with this indentation type, the hardness of small volumes can be measured, ideal for the L phase. Within this working step, EBSD measurements were made as well in order to provide additional insights on a possible orientation relation of the L phase according to the BOR.

For the nanoindentation measurement sample and area were chosen, where L phase was distinctly present. A measurement under 30° angle was made at a sample which was exposed to 1250°C for 45 min in an air environment and quenched with 200°C/s with N_2 gas. The sample was chosen due to its uniform appearance of L phase close to the surface throughout the sample. In course of the testing, the Young's modulus can be calculated as well and is needed for the hardness values [31]. Additionally, needed for this measurement is the poisson number of Ti-6Al-4V of 0.33 [-] [32]. The modulus course of this particular sample is seen in Figure 26.
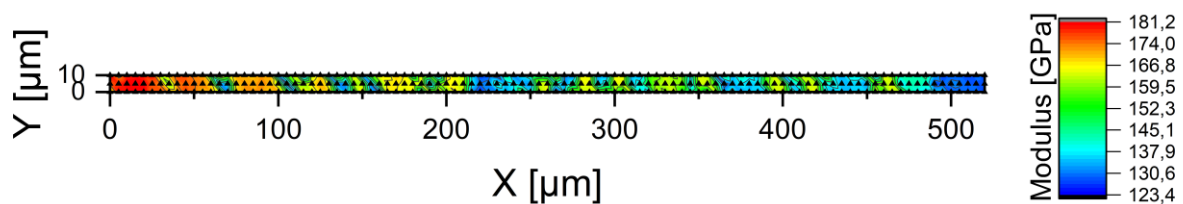
Figure 26: Heatmap of the Young's Modulus of nanoindentation measurements from the tested area.

It can be observed that near the surface region a modulus of 181 GPa is measured. With this being the continuous α case, as the measurement was set to measure right from the surface into the sample middle. However, right after this α case layer at a distance of around 50 μm in the diagram, with a modulus of around 170 GPa, the beginning of the L phase formation can be observed. This L phase containing zone is reaching up to 450 μm of the indentation length, leading to 225 μm from the surface regarding the indentation angle of 30°. The scattered L phase appears to be at least 165 GPa in the center of the L phase. The matrix appears to have a modulus between 120-140 GPa. If compared to literature values for Ti-6Al-4V (110-140 GPa) [1, 2], the matrix is right within these values. The L phase itself, however,

shows an increase of up to 35 GPa, yielding to a modulus of around 175 GPa, for L phase in the immediate area next to the surface.

The same effect can be observed for the hardness values, as illustrated in Figure 27. These values, however, are calculated in [GPa], to compare the received values, a transformation approximation into [HV] was made, as can be seen in Table 5.
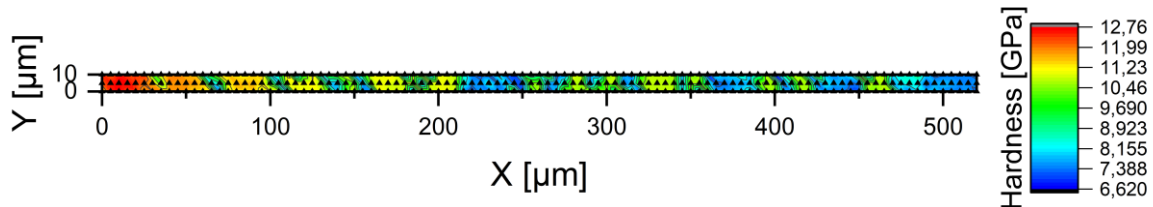
Figure 27: Heatmap of the hardness determined by nanoindentation measurements from the tested area.

The values which were transformed, are the values seen in the table, showing the hardness values in [GPa], next to Figure 27. The hardness is determined by the load over the surface area of the indentation area [33]. The conversion can be made by applying equation 12. It should be mentioned that with this transformation no size effects were regarded.

$$HV = \frac{GPa}{9,81 \frac{m^2}{s}} * 1000 \qquad (12)$$

Table 5: Conversion of hardness values from [GPa] of Figure 27 to [HV], to establish a better visualization when comparing values.

GPa	HV
12.76	1300.71
11.99	1222.22
11.23	1144.75
10.46	1066.26
9.69	987.77
8.923	909.58
8.155	831.29
7.388	753.11
6.62	674.82

The three regions of α case, L phase affected zone and the matrix, can be distinguished once again, with the L phase having an averaged hardness of 1105,25±87,415 HV. Figure 27 demonstrates the decrease of the L phase hardness with a growing distance from the surface. Due to a higher amount of indents, a more precise hardness progression can be estimated.

With a more accurate progression established, a connection of the hardness values and the O content can be made. This is possible because the indents can be observed separately with a higher accuracy, due to the small, tested volume. However, if indents were in the same row, and still within the L phase, the average of these values was calculated. Figure 28 shows the hardness values for the indents, which were explicitly situated in the L phase.
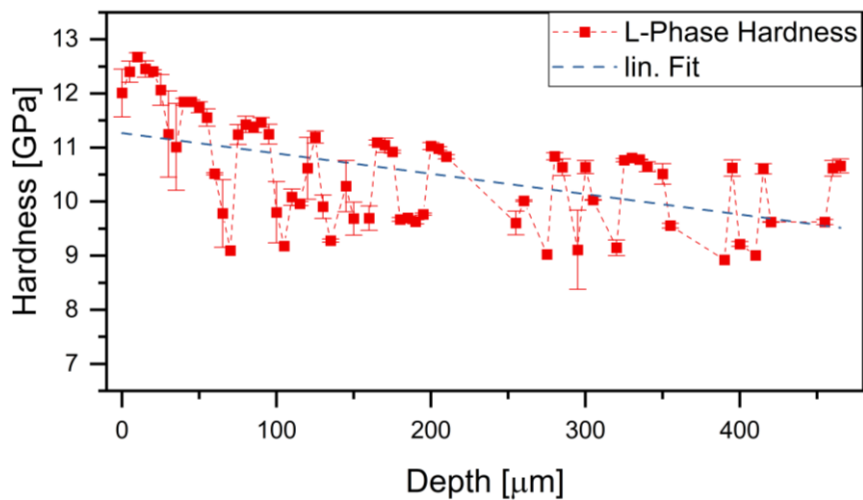
Figure 28: Hardness values received from nanoindentation of the L-phase.

This Figure indicates a linear progression of the L-phase hardness. Leading to an assumption that a linear connection between the O content and hardness can be established at a given base O content. However, in Figure 28 two levels of hardness values for the L phase can be observed. With the lower level of averaged indents, presumable being influenced by the surrounding matrix or the matrix underneath the indent. It has to be considered, that with this measurement a volume is tested, therefore, the softer matrix might influence the hardness values. Interestingly, the hardness decrease within the L phase is much steeper than compared to just the matrix values, as can be seen in Figure 29.
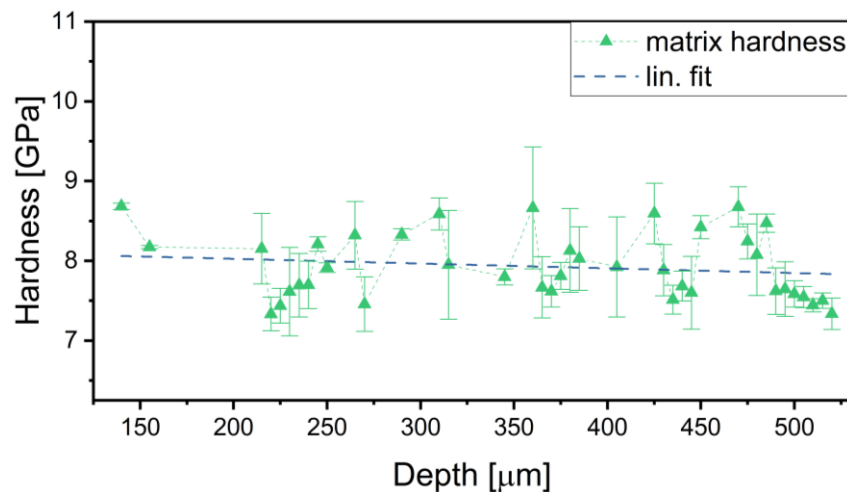
Figure 29: Hardness values received from nanoindentation of the matrix.

According to Figure 29 the hardness of the matrix has an approximately straight linear decrease and stays nearly at the same level. With hardness values of up to 670 HV for regions without L phase and a distance from surface of around 250 µm, considering the 30° influence, leading to an actual distance from surface of 125 µm. These values come very close to the values of the same distance from the microhardness study comparing Figure 21. With an EBSD measurement of the tested area, however, the orientation of the L phase and its nearby microstructure can be investigated. The L phase tested via nanoindentation, appears to belong to one and the same colony according to its crystal orientation shown in Figure 30, the inverse pole figure (IPF) map of the area. In Figure 30 three different orientations of L phase can be seen, as portrayed in IPF colors orange, green and red. The fourth orientation in purple, however, is assumingly the α case on the surface and therefore not considered. If a connection between the BOR and the growth behavior of the L phase can be established, then the assumption of L phase growth along the BOR can be proven to be true. For the nanoindents seen in this figure can be said that they were all made in an area where only one growth direction of L phase occurred. With the pole figures of this EBSD scan, the different orientations can be seen even clearer.
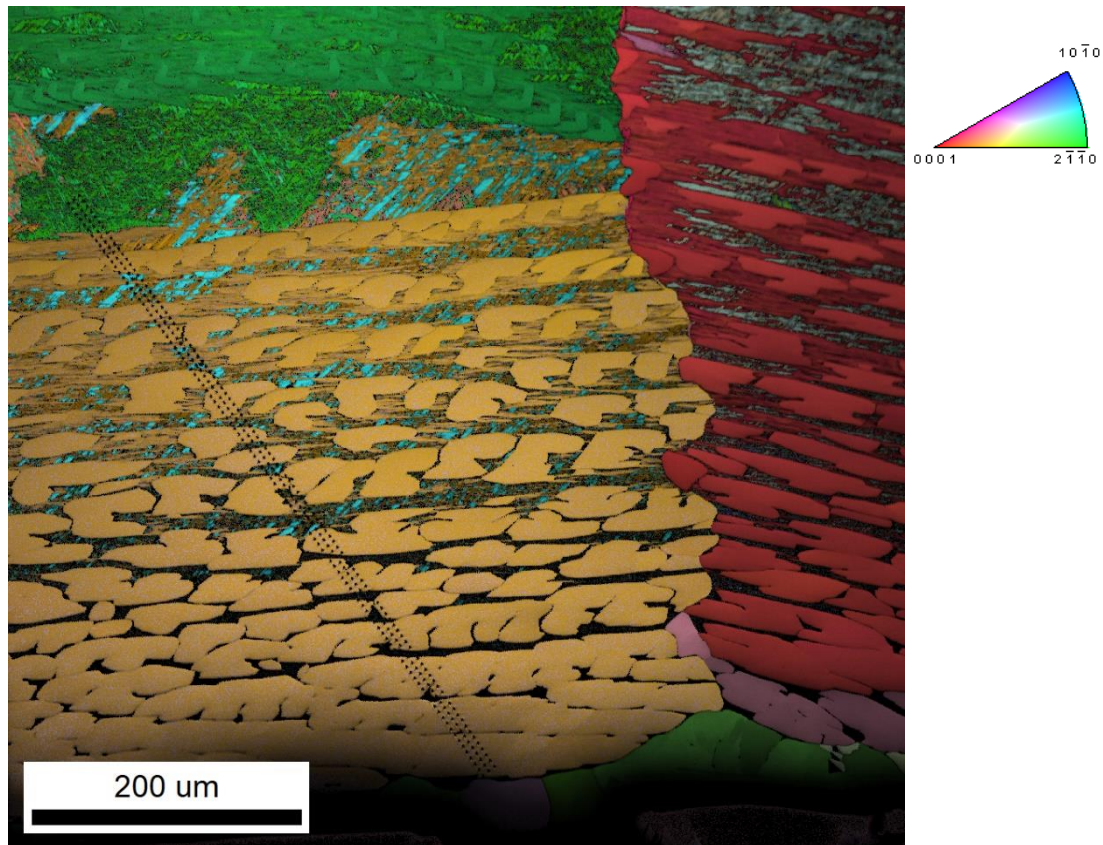
Figure 30: IPF map of a sample area where nanoindentation was applied. Sample condition: annealed for 45 min at 1250°C in an air environment with a cooling rate of 200°C/s in N₂ gas.

For analyzing Figure 31 and Figure 32, Figure 3 can be used as help. The pole intensities of the (0001) basal plane are nicely seen in Figure 31, as illustrated in Figure 30. Nonetheless, the crystallographic plane, when a test in plane normal direction is processed, with the highest Young's modulus is the basal plane (0001), the highest CRSS value is found in the pyramidal plane ($\bar{1}$011), yielding in high hardness values [1, 2]. As the indentation occurs in plane normal direction, the difference of the Young's modulus of the seen plane normal directions can be measured. Therefore, the pole intensities of the (0001) plane in Figure 31 can be used as help. The red dot in the middle belongs to the red area of L phase (Figure 31). In Figure 31 the red dot in the lower right quadrant belongs to the indented L phase zone (orange), seen in Figure 30. Under usage of the OIM software it is possible to estimate the tilt angle between these planes, which was found at 35°. With the help of Figure 2, where the dependence of the Young's modulus according to the declination angle, which is the angle between the normal vector of the basal plane (0001) and the force vector, an estimation of the Young's modulus of the red area should be possible. With a difference of around 20 GPa the orange zone shows a lower Young's modulus compared to the red zone, according to Figure 2 due to its tilt angle. However, in order to validate these estimations, further measurements in more orientation zones should be made.
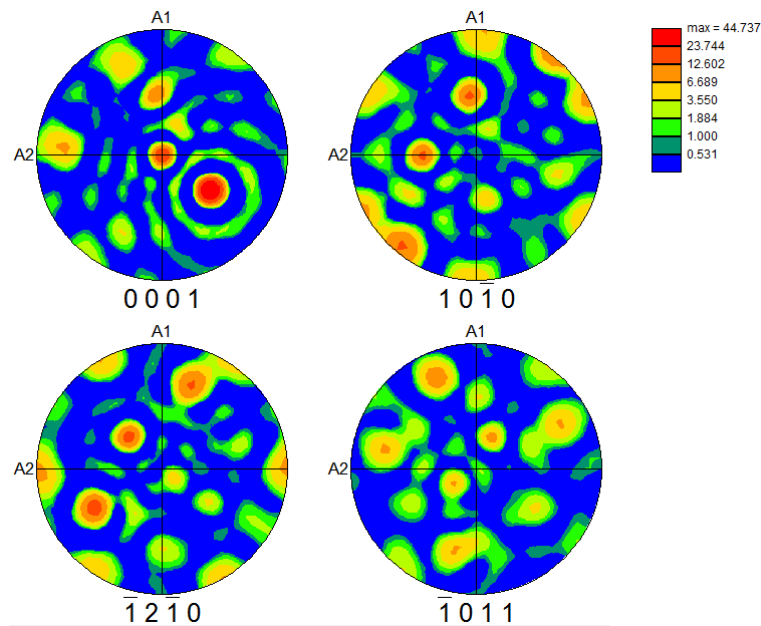
Figure 31: Pole figures of (0001), (10$\bar{1}$0), ($\bar{1}$2$\bar{1}$0) and ($\bar{1}$011) of the area.

The strict border in Figure 30 between the yellow and green orientation on the one side and the red orientation on the other, suggests a grain boundary between these orientations. If the different orientations seen in Figure 30 are further examined, the crystal cells with their orientations can be investigated. As already mentioned before, the modulus and hardness are orientation dependent in the α phase, hence different orientations of the L phase, as well as the matrix, should have different properties as well.
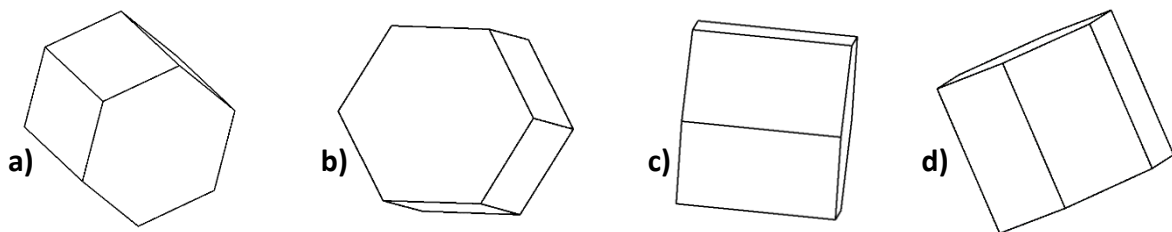
Figure 32: Different crystal orientations of the L-phase as seen in Figure 30. a) yellow b) red, c) green and a matrix orientation seen in Figure 30 d) turquois.

A closer look was taken on the orientation relation within a single parent grain, to proof whether the BOR corresponds to the L phase as well. Therefore, the next picture was cropped out of the scanned area (Figure 30) for further investigation. In Figure 33 the nanoindented grain is investigated. With the found angle relations, the BOR of the L phase should be made demonstrable.
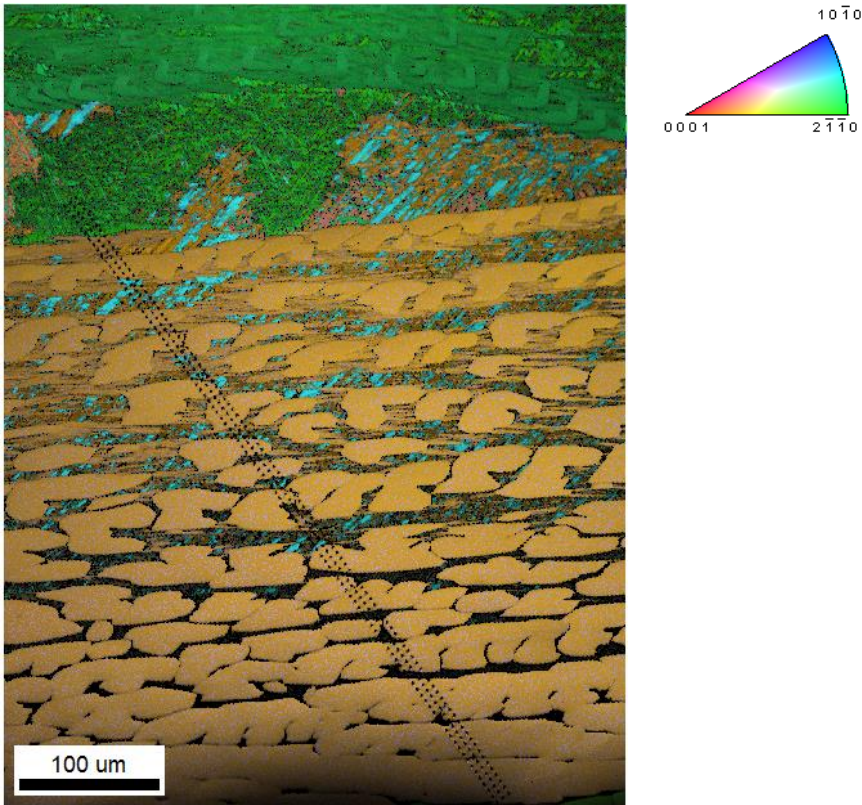
Figure 33: EBSD measurement with higher magnification in order to receive the orientation relations within one grain.

In this illustration (Figure 33), the three main orientations can be seen, visible as orange, green and turquois. If combined into a pole figure (Figure 34) once again, the orientation between them can be depicted. In the following Table 6 the angular relations between the observed orientations are presented.
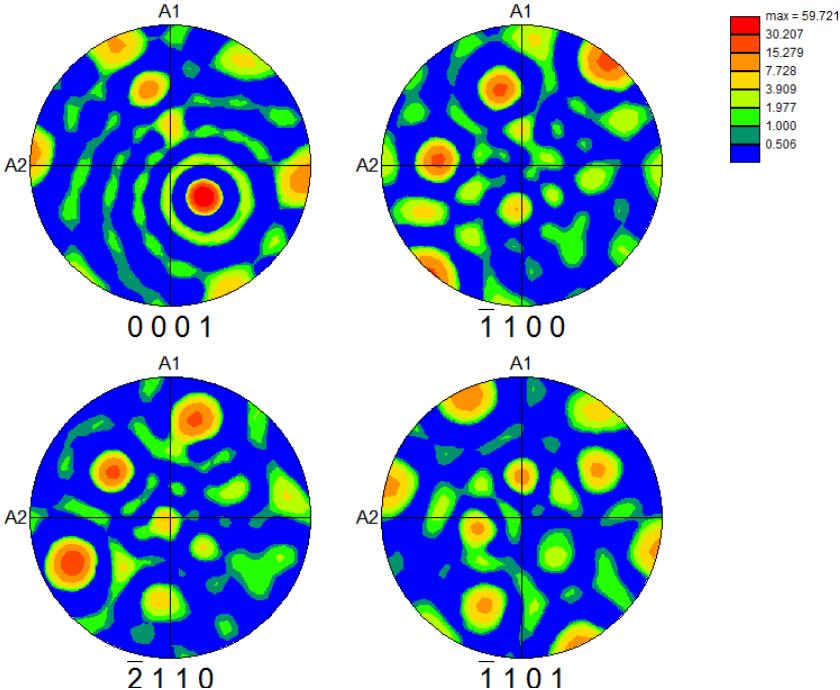
Figure 34: Pole figures (0001), ($\bar{1}$100), ($\bar{2}$110) and ($\bar{1}$101) of the cropped area of Figure 33.

If compared to Figure 31, the (0001) pole from the red crystal structure cannot be seen within this pole figure. This is shown best in the (0001) pole figure, as the intensity maximum in the middle is missing.

Table 6: Angular relation between the different orientations seen in a single grain.

	Yellow	Green	Turquois
Yellow	-	63.8°	61.1°
Green	63.8°	-	61°
Turquois	61.1°	61°	-

In Table 6 the corresponding angles of the found L phase orientations are tabularized. If these values are compared with the work of Chao et al. [34], the found angular relation matches. As Chao is stating that with twelve possible crystallographic orientations (Chapter 1.3), when transforming from a β bcc parent grain into an α hcp grain, a combination of two of the twelve variants lead to five different types of high angle intervariant crystallographic interfaces. With two of the five angles being 60.83°/<$\overline{10}$ $\overline{7}$ 17 3> and 63.26°/<$\overline{10}$ 5 5 $\overline{3}$>, these values fit with the values seen in Table 6, yielding in the confirmation that L phase growing according to the BOR. This also underpins the assumption that the investigated area is in fact part of a former parent grain. However, these assumptions are based on one EBSD measurement, within which only three different orientations were observed. By scanning a wider area within a single grain with more orientations visible, the determination should become clearer and more straightforward.

3.5.   Chemical analysis

Due to all the measurements made within this thesis, only assumptions could have been made so far that this particular phase is stabilized under the influence of O. Therefore, to receive clearance of the existence of O, a chemical analysis is following. In this chapter a qualitative analysis of the O content is made via WDX and EDX measurements. Lastly, due to irregular effects on the immediate surface, a XRD measurement was additionally carried out. A quantitative estimation of the O content within the L phase influenced zone was made too, with the help of results found in Chapter 3.4.

3.5.1.   WDX measurements

As mentioned in Chapter 2.6 two specimens were investigated. Focus was laid onto samples, where different microstructure types could be investigated. Therefore, one sample from microstructure type B and one from type D were used. This was done to get additional understanding, whether O is preferably dissolved in the L phase and α-case, respectively, or if significant amounts are dissolved in the martensitic matrix as well. As type B shows a great

amount of L phase within a wide area near the surface, whereas type D shows a uniform, continuous α-case. The type B specimen was held for 45 min at 1200°C in an air environment and cooled with 200°C/s in N_2 gas, while the type D specimen was held for 60 min at 1200°C in an air environment and cooled with 50°C/s in N_2 gas.

In Figure 35 a scanning electron microscope (SEM) picture is seen of the type B specimen, with the inserted line where the line scan took place. The typical microstructure of type B with coarse L phase, widely distributed within the surface region of the specimen can be seen. In the SEM picture the L phase has a darker contrast than the matrix, indicating a lower number of electrons, thus lower atomic number of elements, indicating an O influence within this phase. The brighter martensitic matrix indicates a higher atomic number of elements. Figure 36 reveals the one-dimensional distributions of the chemical elements of the tested alloy material, indicated along the black line seen in Figure 35. In addition, the darker regions marked with 1, 2 and 3 are marked as well for better visualization.
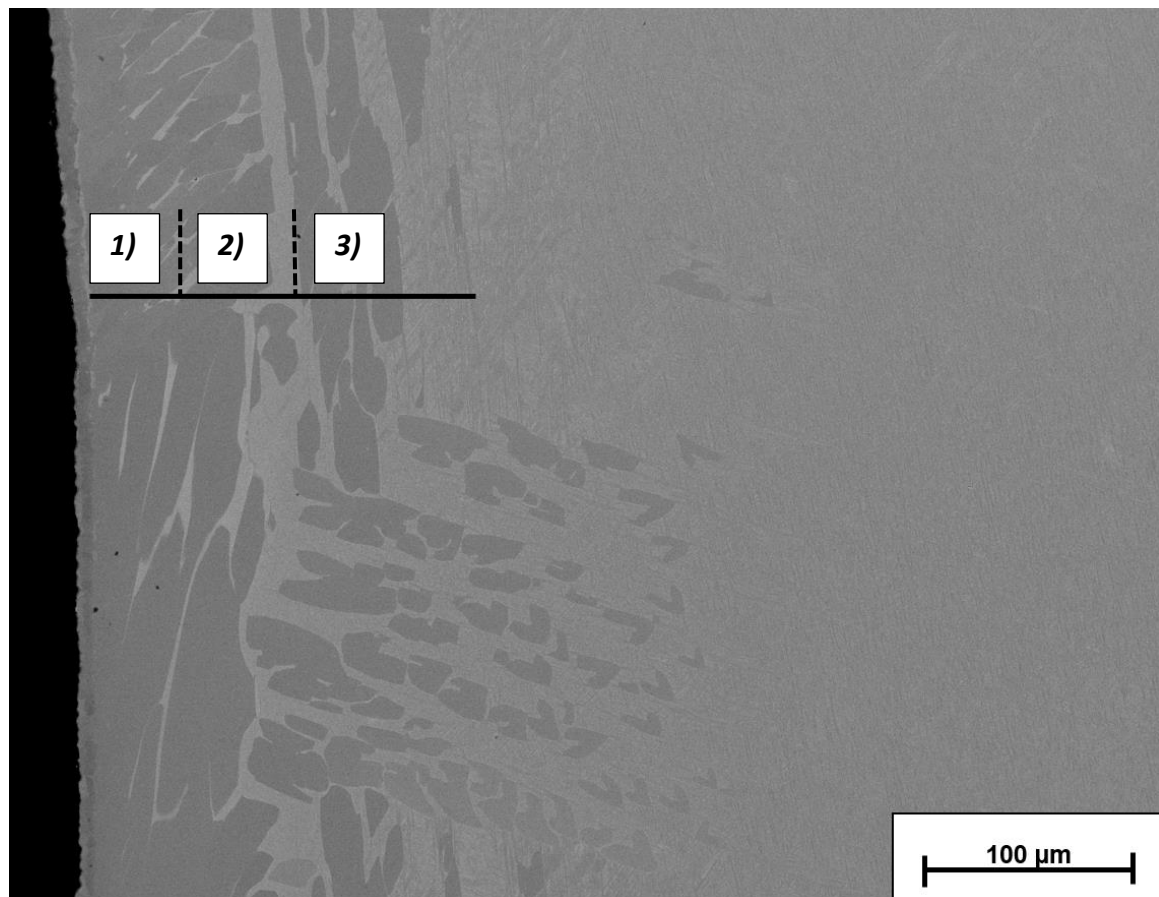
Figure 35: SEM picture of a type B sample, held for 45 min at 1200°C in an air environment and cooled with 200°C/s in N_2 gas, used for WDX measurement, with the presumed line scan added to the picture and three O influenced zones.
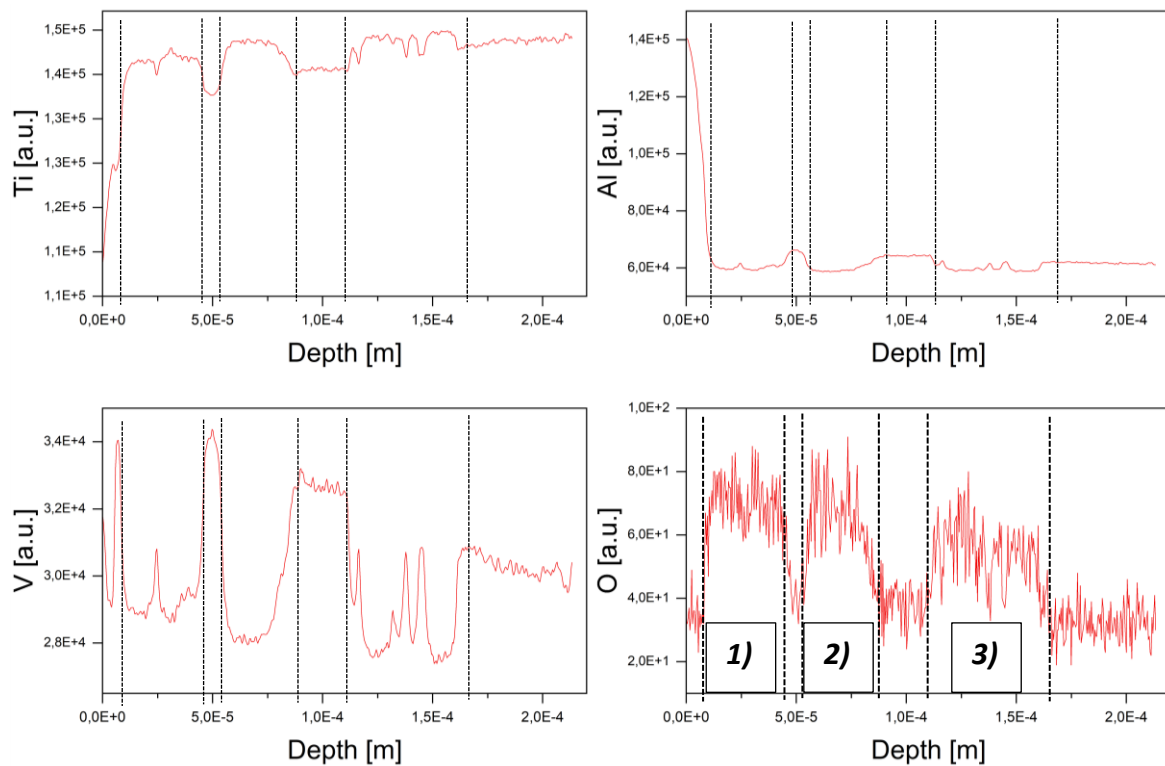
Figure 36: WDX result of the line scan performed on the sample with microstructure type B. Titanium, Al, V and O contents are shown.

As the results reveal, the O content is significantly increasing when crossing the L phase along the line scan. That proofs O as a strong stabilizer for α phase and thus L phase, even stronger than Al, with Al still being present as an α stabilizer in the L phase but at a smaller level. If investigated even further it shows that Ti and O are increasing in the L phase, whereas Al and V are decreasing, leading to an increase within the matrix next to an L phase. Aluminum, however, shows a significant increase next to the beginning of the scan, at the immediate surface zone. This can be explained by Du et al. [24] with outward diffusion of Al and inward diffusion of O, ultimately leading to the formation of alternate growth of Al_2O_3 and TiO_2 on the surface.

However, within a microstructure of type D, the local maxima as observed for O in Figure 36 should be annihilated by applying a lower cooling rate, as type D shows a formation of a continuous α case without L phase in the region next to the surface. Instead, a formation of a single maximum is observed right next to the surface of the specimen. In the following Figure 37 the SEM picture of the microstructure and the presumed line of the line scan is illustrated, with Figure 38 beneath, showing the qualitative analysis of the line scan of the specimen. The signal to noise ratio is strong in this diagram (Figure 38). As mentioned in the experimental chapter before (Chapter 2.6), O measurements are difficult to perform, due to the low detection intensity.
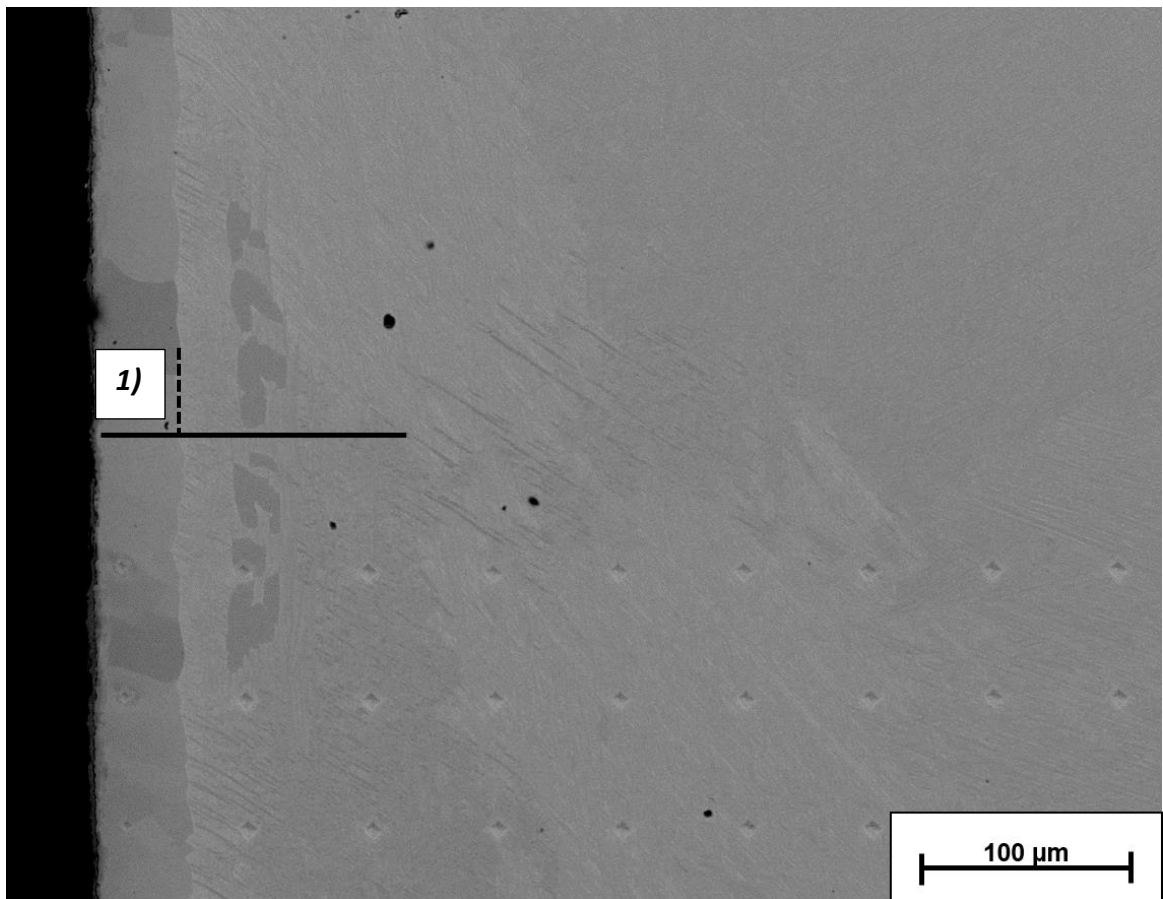
Figure 37: SEM picture of a type D sample, held for 60 min at 1200°C in an air environment and cooled with 50°C/s in N₂ gas, used for WDX measurement, with the presumed line scan added to the picture and O influenced zones.
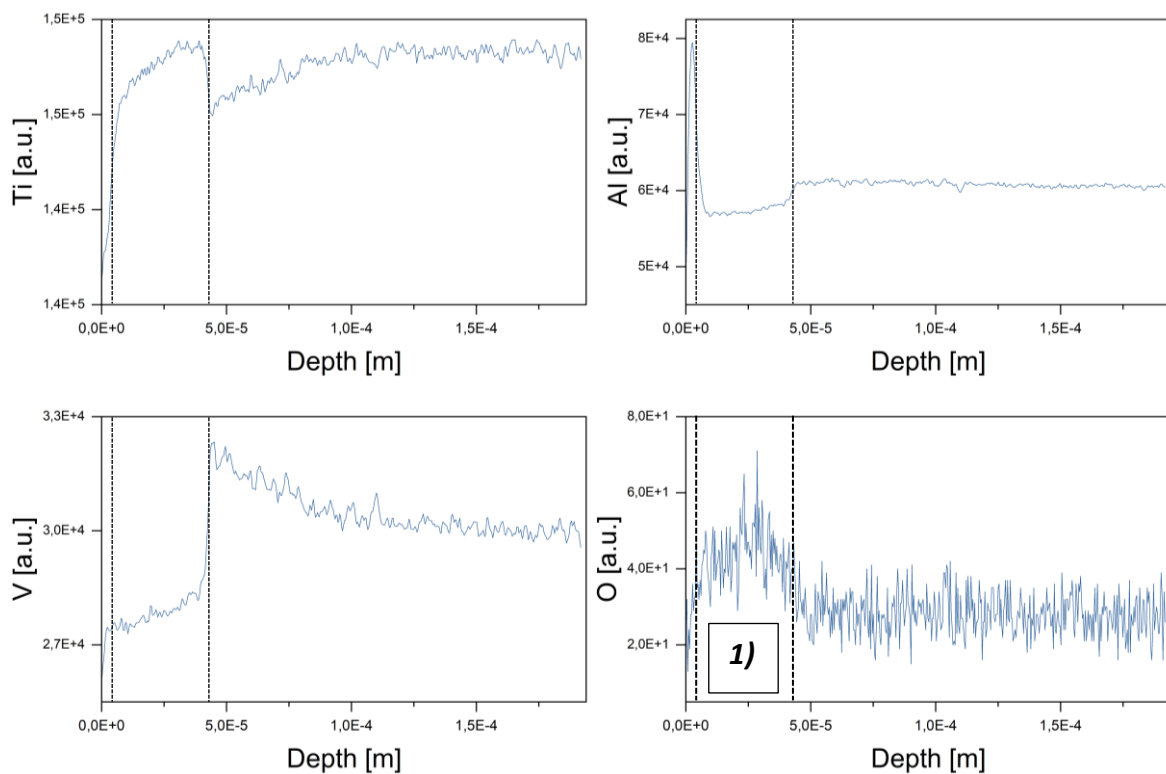
Figure 38: WDX results of the line scan performed on the sample with microstructure type D. Titanium, Al, V and O contents are shown.

Another indicator for the presence of α case within this edge zone can be observed in the diagram of the Ti content. According to Figure 36, in the area where O increases, Ti does likewise. The Ti diagram shows a steep decrease, suggesting the O decrease due to the transition from the surface zone to the matrix as well. For V and Al this behavior is observed vice versa. However, a steep increase of the Al content right next to the surface is observed again, though showing a decrease of it right after the observed peak. Indicating another phase on the very surface of this specimen. An explanation on why this behavior is visible in Figure 38 but not in Figure 36, is due to the measurement location. Comparing these two, a measurement right next to the outer sample surface might only has been performed on type D microstructure.

With these qualitative results of the WDX measurements, an attempt on estimating the O content can be made. This model is an approximation only for the used specimen in particular and should only be seen as a tool of understanding the O course within a specimen. It can only be applied on the particular specimen, as L phase is different for each sample, as well as the local limitation of the WDX line scan restricts this model. Therefore, the qualitative results of the WDX line scan of the sample with microstructure type B, which was held for 45 min at 1200°C in an air environment and cooled with 200°C/s in N_2 gas, was used. As this line scan crossed three zones of L phase and the matrix, delivering qualitative values for the O content within the sample (Figure 35 and Figure 36). In Figure 36 a slight decrease of the O values is observed with altered distance from surface for the O rich regions. On the one hand, at a distance of around 25 μm, or at the first O peak in this diagram, the average value of O is at 70.4. This averaged value comes from the majority of the qualitative values found within the first zone of O increase. On the other hand, the mean value of O of the matrix is at 32.2, this averaged value was estimated the same as the O value. Which means that the qualitative O content, within the L phase at a distance from the surface of 25 μm, is increasing by a factor of 2.2 in this specimen. If this factor is applied onto the known ground O content of 0.18 wt.% of the sample material, the O content within the L phase at a distance of 25 μm is increased up to 0.396 wt.%. With the help of the exponential fit used in the model for calculating the diffusional coefficient, the course of the O content within the sample can be illustrated, as can be seen in Figure 39. For this model, an O content of 0.45 wt.% on the surface has been estimated.

However, as already shown in the Chapters 2.3 and 2.3.1, the hardness of the L phase is at higher values compared to the matrix hardness values. If the hardness values of the matrix (625.11 HV), referred to as ground hardness, and the hardness value of a depth of around 25 μm (1020.89 HV), of the same type B specimen, are compared, the hardness is increasing by a factor of 1.63. Comparing this with the factor of 2.2 for the O content increase at the same

depth, a similarity between O content and hardness course can be observed and it demonstrates their dependence on each other.
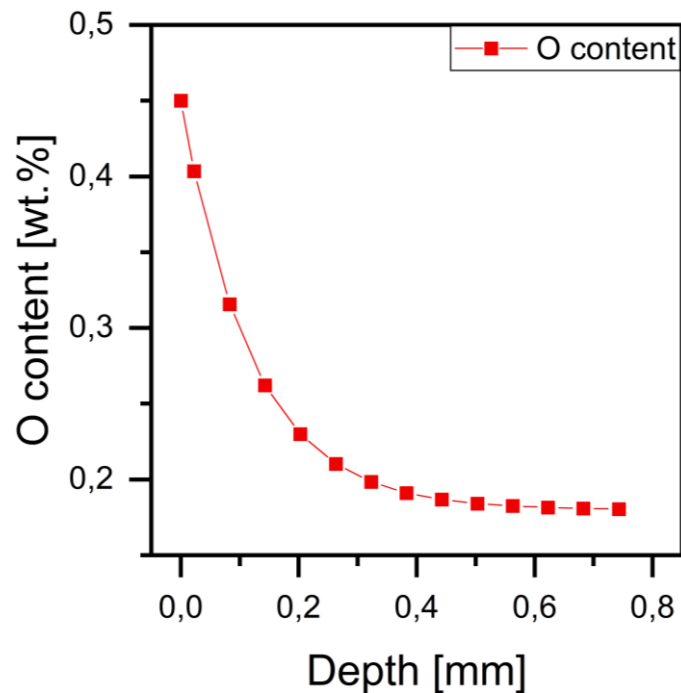
Figure 39: Estimation of O content over depth, for a sample with exposure to 1200°C for 45 min in an air environment with a cooling rate of 200°C/s in N_2 gas.

But as already mentioned, this estimation is based on a single hardness measurement series and a single WDX line scan, with averaged values for both. Therefore, this model is only of help to make an approximation and visualization and should be seen as motivation for further analysis in providing better results of the actual O content in the L phase and its decrease, as well as the influence of O onto the hardness. Even more experiments must be done in order to proof that α_S phase is in fact L phase, as assumed in Chapter 3.1 through thermodynamical calculations.

3.5.2.   EDX measurements

An even closer look onto the composition of the material surface can be achieved by a mapping using EDX technique. Due to the unexpected results described above, with the local Al maxima near the surface region seen in Figure 36 and Figure 38, the presence of another element is investigated. This element is presumably N, as the cooling process after the applied heat treatments was always performed with N. In order to gain evidence about this theory, an EDX mapping of the specimen with the microstructure type D was processed, which was held at 1200°C for 60 min in an air environment and cooled at 50°C/s in N_2 gas. In Figure 40 the elements to be considered more closely are depicted by a two-dimensional EDX measurement (Al, N and O). The combined measurement of the entire sample area can be seen in Figure 41.
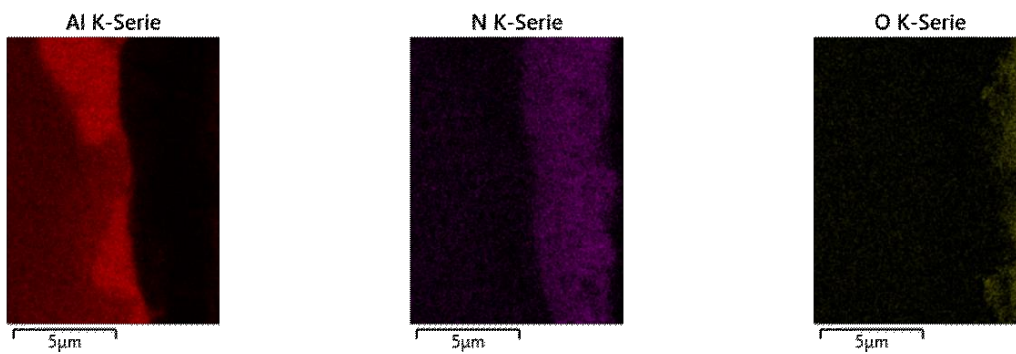
Figure 40: Differentiated illustrations of Al (red), N (purple) and O (yellow) content from EDX measurements.
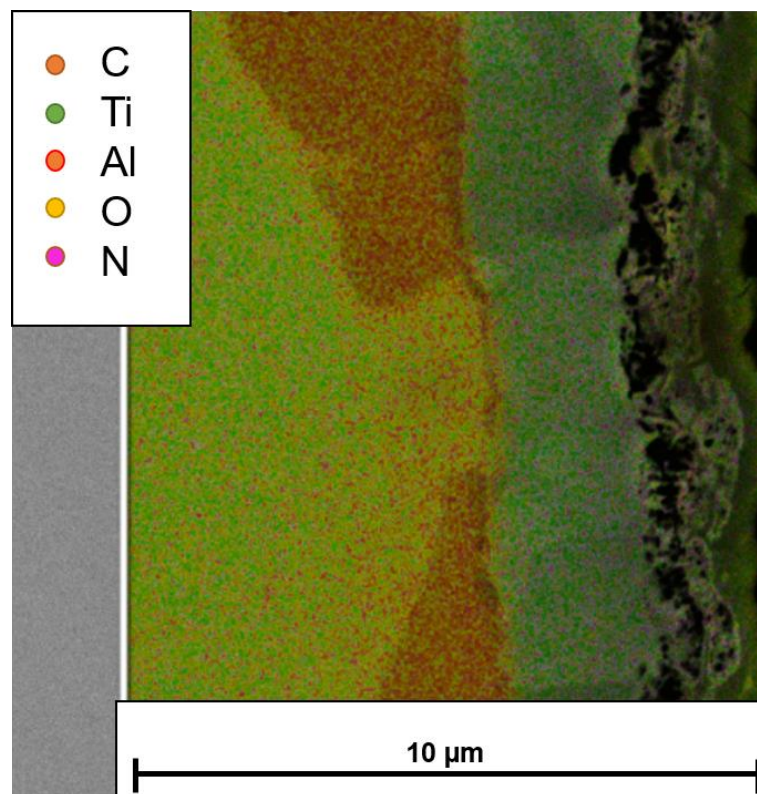
Figure 41: EDX mapping of a specimen with microstructure type D. This specimen was held for 60 min at 1200°C in an air environment and afterwards cooled with a cooling rate of 50°C/s in N_2 gas.

Nitrogen can be verified as being in the zone closest to the surface of the specimen. The element appears to be dissolved in the edge zone of the sample, indicating, a nitride phase on the very surface of the sample. Therefore, an additionally made XRD analysis should provide proof and will be discussed in the next chapter. Aluminum, however, is concentrated in areas along the edge zone. By an even closer investigation, the continuous edge zone and the matrix next to it are connected with a film of high Al content, explaining the increase of Al, seen in Figure 36 and Figure 38. As Al shows a behavior of accumulating next to Ti and O rich phases, delivering further proof of O as an α stabilizer. Du et al. [24] describes a layered assembly of TiO_2 and Al_2O_3 near the surface area, in Figure 41, a layered structure can be seen as well.

3.5.3. Qualitative XRD analysis

For further investigations of the surface phases e.g., a nitride phase on the surface, an analyzation by XRD was made. As described in Chapter 2.7, the specimens were rotated onto the unpolished surface during the measurement of the broad side 10 mm x 5 mm and the embedment was removed. This was necessary due to very narrow zone of N influence seen in Chapter 3.5.2. The XRD measurements were performed on the same samples as the previous WDX and EDX investigations were made on. With the type B specimen, held for 45 min at 1200°C in an air environment and cooled with 200°C/s in N_2 gas, while the type D specimen was held for 60 min at 1200°C in an air environment and cooled with 50°C/s in N_2 gas. In Figure 42, a diffraction pattern of the specimen with a microstructure type B can be seen. In this figure the α phase, TiO_2, in the form as rutile and peaks of TiN were observed, verifying the existence of nitride formation on the surface of specimen of Ti-6Al-4V.
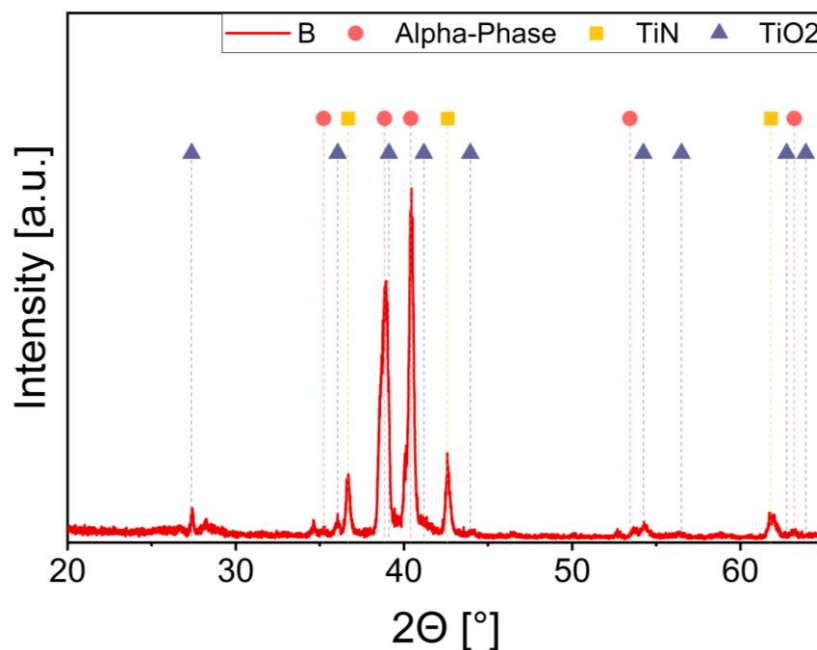
Figure 42: XRD pattern Θ/2Θ of the specimen with microstructure type B, held for 45 min at 1200°C in an air environment and cooled with 200°C/s in N_2 gas. Crystallographic phases are added to their associated reflection angle.
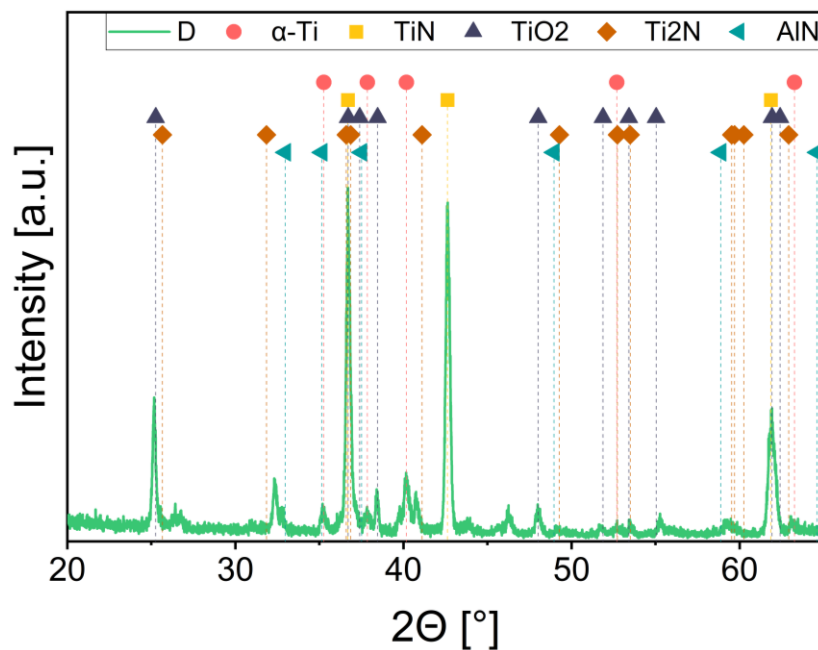
Figure 43: XRD pattern Θ/2Θ of the specimen with microstructure type D, held for 60 min at 1200°C in an air environment and cooled with 50°C/s in N₂ gas. Crystallographic phases are added to their associated reflection angle.

The second sample with microstructure type D exhibited a high amount of N in the edge zone during the EDX-measurement, as can be seen in Figure 43. More crystallographic phases are indexed, for example AlN and TiO_2 as anatase. Nonetheless, nitrides were once again detectable in TiN and Ti_2N, with Ti_2N pricing the existence of an additional nitride. However, in both graphs a few peaks cannot be detected. This might be due to an even greater variety of present phases, such as mixed oxides or nitrides. Also, the unsteady distribution of elements in the surface zone suggests the presence of multiple phases. By matching microstructures type B and type D, a high intensity of α phase can be seen for type B (Figure 42), whereas for type D, TiN shows the highest intensity peaks (Figure 42). It must be mentioned that the specimens investigated were embedded beforehand, therefore, embedment residues might be measured too. This was taken into account in order to get an unadulterated impression of the formed phases on the sample's surface.

If the microstructures of these two types are compared yet again, their different formation of the edge zone is of interest. With microstructure type D suggesting the formation of a continuous layer of α case (Figure 15), whereas microstructure type B has a wide zone of distributed L phase (Figure 12, Figure 13). Comparing this with the EDX measurement from type D (Figure 41), which showed high amounts of N within this continuous edge zone and high intensities of the TiN phase were observed as well with the XRD analysis (Figure 43). Therefore, the steep hardness increase close to the surface of type D can be assumed, as dissolved N atoms, hence, N as an additional interstitial strengthener next to O.

The outcome of this chemical investigation was the verification of O as an even more preferred stabilizer of the α phase than Al, thus forming the L phase together with Ti. However, within

the WDX measurements an unexpected interaction of the alloying elements along the surface edge was observed, with Al showing a local maximum on the surface. Due to this an additional EDX measurement was made and found that N as well is situated within the area of the continuous edge zone. With deeper investigations of the surface zone by applying an XRD analysis, proof for the existence of nitrides on Ti-6Al-4V were found. But according to this analysis, mainly TiN was verified at the surface and the Al maxima could not be explained. It should be mentioned that with a XRD analysis, the surface is investigated in a very narrow zone, therefore, the Al-nitride concentration was not able to be detected as TiN might be of greater presence than Al-nitrides or Al-oxides along the outer surface. However, the observed local Al maxima in Figure 36 and Figure 38 at the outer end of the WDX line scan, might hint an additional Al_2O_3 layer next to the α-case on the surface. This assumption of the layer formation shows the phase variety and its complexity and shows that to proof this assumption, more sample surfaces should be investigated according to its layered structure. Additionally, in the course of the WDX line scans a quantitative, approximation model was established in order to provide further information of the O decrease within the sample, thus the L phase formation. With this model an estimation of up to 0.45 wt.% of O on the sample surface could be established.

4. Conclusions

In the course of this thesis, a unique appearance of α phase within the microstructure of Ti-6Al-4V was characterized. Different heat treatments were applied to get a deeper understanding of the formation criteria and influencing parameters of this phase were made. The properties were analyzed by various tests in order to get a broad understanding of the designated L phase. However, the main conclusions that can be drawn in consequence of this study concerning the L phase formation in Ti-6Al-4V are as follows.

- The zone where L phase occurs can be enhanced by elevated temperatures with over 400 μm found in this study, however, it declines with longer holding times. The transformation was observed by first forming more stem-shaped L phase precipitations and eventually a continuous edge zone, also known as the α-case. It was also observed that with lowered cooling rates, still in the martensitic transformation range, this continuous edge zone showed an increase in thickness. However, preferred growth conditions were observed as well. Also, a diffusional barrier might have been established by growth of a continuous edge zone, which might be the reason that the L phase affected zone is becoming smaller with lower cooling rates.

- With the help of a mathematical model, combining hardness values with diffusional processes, it was possible to confirm the possibility that L phase amount, O amount and mechanical properties within the sample are correlated. With an estimation of the diffusional path, the comparison with the actual measured depth of L phase and chemical comparative analysis, this model proofed to be very sufficient. With this model established, the diffusion coefficient of O in Ti-6Al-4V for temperatures between 1000°C and 1300°C was calculated in a range between $D_{1000°C}=1.2*10^{-8}\frac{cm^2}{s}$ and $D_{1300°C}=1,2*10^{-7}\frac{cm^2}{s}$.

- The L phase influenced zone showed a great hardness increase, which is associated with the influence of O, to up to 1400 HV. However, with longer exposure times at elevated temperatures, the influenced zone decreased in depth as the hardness showed a steeper decline, similarly as the LOM study suggested. With specimens showing a complete annihilation of L phase, thus the formation of a continuous α case, this behavior was aggravated. However, all specimens, which were heat treated above T_β showed an additional increase of ground hardness.

- The nanoindentation study showed a linear decrease of L phase hardness, whereas the matrix hardness exhibited a much lower depth dependence. Knowing that O is concentrated in the L phase, boosting both, hardness and Young's modulus values similarly, to significant higher values compared to values found in literature for Ti-6Al-4V with typical chemical compositions.

- An orientation relation according to the BOR was verified for the L phase in the investigated area via EBSD analysis as well, with the found angular relation of 63.8°, 61.1° and 61°, which correlate with angular relations found in literature [34]. Confirming that the orientation relationship of Burger are applied for the L-phase too. Therefore, the rules of orientation related properties are present for the L phase as well.

- The chemical analysis proofed O as the main chemical element next to Ti within the L phase. Indicating O as a more preferred α stabilizer than Al according to the WDX measurements. Furthermore, with an approximation of the O content for the L phase, based on the original chemical compositions of the as-received samples, together with thermodynamical simulations, it can be assumed, L phase being α_S phase. In accordance with this approximation, an estimation for the O content on the surface was made with 0.45 wt.%.

- With the help of EDX measurements N was proven to be accommodated within the immediate surface zone of the specimen. Indicating the subsequent quenching step with N and up to 80 vol.% N in an air environment, of being able to influence the microstructure with N atoms. This circumstance is additionally with the amount of O within the α phase, responsible for the significant hardness increase of the immediate surface zone, hence the even higher hardness of the continuous α case compared to the hardness values of the L phase. With the N verified of being within the zone next to the surface, nitrides, as TiN and Ti_2N, were able to be confirmed on the surface via XRD measurements.

These conclusions indicate further applications of Ti-6Al-4V, as with proper heat treatments the α-case can be enhanced in its growth. With a hardness of the L phase on a level of 900 HV down to depths of 300 μm, but still retaining a ductile matrix with high fracture toughness underneath, parts with these properties could be used for mechanical applications as well, giving a motivation for further research on this particular field of Ti-6Al-4V.

5. References

[1] G. Lütjering and J. C. Williams, Titanium: Engineering Materials and Processes, Heidelberg: Springer-Verlag Berlin Heidelberg, 2003.

[2] M. Peters and C. Leyens, Titan und Titanlegierungen, D. M. Peters and D. C. Leyens, Eds., Köln: Wiley-VCH Verlag GmbH & Co. KGaA, 2002.

[3] G. Gottstein, Materialwissenschaft und Werkstofftechnik: Physikalische Grundlagen, vol. IV, Aachen: Springer, 2014.

[4] J. M. Oh, B. G. Lee, S. W. Cho, S. W. Lee and J. W. Lim, "Oxygen effects on the mechanical properties and lattice strain of Ti and Ti-6Al-4V," *Metals and Materials International,* 17, 733-736, 2011.

[5] Y. T. Lee and G. Welsh, "Young's modulus and damping of Ti-6Al-4V alloy as a function of heat treatment and oxygen concentration," *Materials Science and Engineering,* 128, 1, 77-89, 1990.

[6] R. von Mises, "Mechanik der festen Körper im plastisch-deformablen Zustand," *Nachrichten von der Gesellschaft der Wissenschaft zu Göttingen. Mathematisch-Physikalische Klasse,* 1913, 1, 582-592, 1913.

[7] K. S. Chan, M. Koike, B. W. Johnson and T. Okabe, "Modeling of Alpha-Case Formation and Its Effect on the Mechanical Properties of Titanium Alloy Castings," *Metallurgical and Materials Transactions A,* 39, 171-180, 2008.

[8] W. J. Boettinger, M. E. Williams, S. R. Coriell, U. R. Kattner and B. A. Mueller, "Alpha case thickness modeling in investment castings," *Metallurgical and Materials Transactions B,* 31, 1419-1427, 2000.

[9] M. Meng, X. G. Fan, H. Yang, L. G. Guo, M. Zhan and P. F. Gao, "Precipitation of secondary alpha in competition with epitaxial growth of primary alpha in two-phase titanium alloys," *Journal of Alloys and Compounds,* 714, 294-302, 2017.

[10] J. B. Newkirk and A. H. Geisler, "Crystallographic Aspects of the Beta to Alpha Transformation in Titanium," *Acta Metallurgica,* 1, 370-374, 1953.

[11] N. Stanford and P. S. Bate, "Crystallographic variant selection in Ti-6Al-4V," *Acta Materialia,* 52, 17, 5215-5224, 2004.

[12] T. Ahmed and H. J. Rack, "Phase Transformations during cooling in α and β titanium alloys," *Materials Science and Engineering A,* 243, 206-211, 1998.

[13] D. Banerjee and J. C. Williams, "Perspectives on Titanium Science and Technology," *Acta Materialia,* 61, 844-879, 2013.

[14] R. Davis, H. M. Flower and D. R. F. West, "Martensitic transformations in Ti-Mo alloys," *Journal of Materials Science,* 14, 712-722, 1979.

[15] J. Crank, The Mathematics of Diffusion, 2. ed., Oxford: Clarendon Press, 197.

[16] H. S. Carslaw and J. C. Jaeger, Conduction of Heat in Solids, 2. ed., Oxford: Clarendon Press, 1959.

[17] P. Shewmon, Diffusion in Solids, Cham: Springer International Publishers, 2016.

[18] M. H. Song, S. M. Han, D. J. Min, G. S. Choi and J. H. Park, "Diffusion of oxygen in β-titanium," *Scripta Materialia,* 59, 623-626, 2008.

[19] A. Einstein, "On the movement of small particles suspended in a stationary liquids required by the molecular-kinetic theory of heat," *Annalen der Physik,* 17, 549-560, 1905.

[20] E. György, A. P. del Pino, G. Sauthier, A. Figueras, F. Alsina and J. Pascual, "Structural, morphological and local electric properties of TiO2 thin films grown by pulsed laser deposition," *Journal of Physics D: Applied Physics,* 40, 5246-5251, 2007.

[21] I. Gurrappa, "An oxidation model for predicting the life of titanium components in gas turbine engines," *Jounral of Alloys and Compounds,* 389, 190-197, 2005.

[22] R. Boyer, E. W. Collings and G. Welsh, Materials Properties Handbook: Titanium Alloys, OH: ASM International, 1994.

[23] P. Kofstad, High Temperature Corrosion, New York: Elsevier Applied Science Publishers Ltd., 1988.

[24] H. L. Du, P. K. Datta, D. B. Lewis and J. S. Burnell-Gray, "Air oxidation behaviour of Ti-6Al-4V alloy between 650 and 850°," *Corrosion Science,* 36, 4, 631-642, 1994.

[25] H. Guleryuz and H. Cimenoglu, "Oxidation of Ti-6Al-4V alloy," *Jounal of Alloys and Compounds,* 472, 241-246, 2009.

[26] C. Fleißner-Rieger, T. Pogrielz, D. Obersteiner, T. Pfeifer, H. Clemens and S. Mayer, "An Additively Manufactured Titanium Alloy in the Focus of Metallography," *Pract. Metallogr.,* 58, 1, 4-31, 2021.

[27] K. Persson, "Materials Project," Lawrence Berkeley National Laboratory, 8 9 2020. [Online]. Available: https://materialsproject.org/. [Accessed 29 January 2021].

[28] J. W. Elmer, T. A. Palmer, S. S. Babu and E. D. Specht, "In situ observations of lattice expansion and transformation rates of alpha and beta phases in Ti-6Al-4V," *Materials Science and Engineering,* A, 391, 104-113, 2005.

[29] J.-O. Anderson, T. Helander, L. Höglund, P. Shi and B. Sundman, "Thermo-Calc & DICTRA, computational tools for materials science," *Calphad,* 26, 2, 273-312, 2002.

[30] "Thermo-Calc," Thermo-Calc Software, [Online]. Available: https://www.thermocalc.com/media/50231/tcti2_extended_info.pdf.. [Accessed April 2019].

[31] W. C. Oliver and G. M. Pharr, "An improved technique for determining hardness and elastic modulus," *J. Mater. Res,* 7, 6, 1564-1583, 1992.

[32] M. Fukuhara and A. Sanpei, "Elastic moduli and internal frictions of Inconel 718 and Ti-6Al-4V as a function of temperature," *Journal of Material Science Letters,* 12, 1122-1124, 1993.

[33] A. Fischer-Cripps, Introduction to Contact Mechanics, New York: Springer, 2000.

[34] Q. Chao, P. D. Hodgson and H. Beladi, "Microstructure evolution of martensitic Ti-6Al-4V alloy during warm deformation," *Materials Science Forum,* 783-786, 679-684, 2014.

6. List of Figures

7. Appendix

Figure 44: LOM pictures a) and b) of a sample which was held for 60 min at 1200°C in an air environment and quenched with cooling rate of 100°C/s in N_2 gas. This sample shows a microstructure type C.

Table 7: Tabularized hardness calculation for a sample held for 45 min at 950°C in an air environment and quenched in N$_2$ gas with a cooling rate of 200°C/s.

Indent row Nr.	d$_1$ [µm]	d$_2$ [µm]	d [µm]	Hardness [HV]	averaged [HV]	Std. dev. [HV]	Depth [µm]
R1	12.535	12.816	12.6755	588.4794938			
R1	12.205	12.263	12.234	631.7199333			
R1	11.99	11.99	11.99	657.6929204	670.8102478	59.21019921	25.4172
R1	11.743	10.901	11.322	737.5903601			
R1	10.911	11.718	11.3145	738.5685317			
R2	13.077	12.805	12.941	564.5804802			
R2	14.177	12.805	13.491	519.4852831			
R2	12.816	13.622	13.219	541.0835466	560.7557993	31.66071541	85.4172
R2	12.805	13.089	12.947	564.0573168			
R2	12.544	12.263	12.4035	614.5723699			
R3	13.633	14.167	13.9	489.3639046			
R3	14.17	13.08	13.625	509.3173975			
R3	13.897	13.625	13.761	499.299974	488.4770009	22.63822002	145.4172
R3	14.439	14.714	14.5765	444.9948853			
R3	13.897	13.622	13.7595	499.4088429			
R4	14.462	14.714	14.588	444.2935658			
R4	13.625	14.442	14.0335	480.0976003			
R4	13.897	13.894	13.8955	489.6809128	469.8932726	25.13224201	205.4172
R4	13.625	13.897	13.761	499.299974			
R4	15.007	14.442	14.7245	436.0943103			
R5	14.48	14.987	14.7335	435.5616941			
R5	14.439	14.17	14.3045	462.0789334			
R5	14.994	15.007	15.0005	420.1942088	450.1217672	19.068216	265.4172
R5	14.45	13.894	14.172	470.7596658			
R5	13.897	14.714	14.3055	462.014334			
R6	14.714	14.442	14.578	444.9033147			
R6	14.48	14.442	14.461	452.1316203			
R6	14.722	13.394	14.058	478.4256496	451.2783831	14.47304992	325.4172
R6	14.177	15.266	14.7215	436.2720661			
R6	14.722	14.442	14.582	444.6592646			
R7	14.714	14.442	14.578	444.9033147			
R7	14.722	14.722	14.722	436.2424326			
R7	14.442	13.897	14.1695	470.9257977	443.569411	16.27095604	385.4172
R7	15.529	14.45	14.9895	420.8111516			
R7	13.897	15.257	14.577	444.9643586			
R8	14.712	13.625	14.1685	470.9922751			
R8	14.17	14.442	14.306	461.9820395			
R8	15.259	13.919	14.589	444.2326599	458.4189746	11.83919354	445.4172
R8	14.722	14.442	14.582	444.6592646			
R8	14.17	14.19	14.18	470.2286341			
R9	13.894	14.45	14.172	470.7596658			
R9	14.722	14.439	14.5805	444.7507598			
R9	15.266	14.442	14.854	428.52355	435.525906	21.62713052	505.4172
R9	15.823	14.722	15.2725	405.3603494			
R9	14.439	15.279	14.859	428.2352052			
R10	14.987	13.894	14.4405	453.4162403			
R10	14.167	15.266	14.7165	436.5685674			
R10	15.266	14.439	14.8525	428.6101102	432.1172141	13.00475512	565.4172
R10	14.984	15.259	15.1215	413.4964502			
R10	14.722	14.987	14.8545	428.4947024			
R11	14.712	14.442	14.577	444.9643586			
R11	14.722	14.45	14.586	444.4154153			
R11	13.905	15.266	14.5855	444.4458855	443.0781316	8.209501824	625.4172
R11	14.442	14.439	14.4405	453.4162403			
R11	14.442	15.279	14.8605	428.1487585			
R12	13.894	15.007	14.4505	452.7889134			
R12	15.551	14.442	14.9965	420.4183946			
R12	14.987	15.823	15.405	398.4172448	432.2528339	20.77813875	685.4172
R12	14.994	14.439	14.7165	436.5685674			
R12	14.17	14.722	14.446	453.0710493			
R13	15.804	14.712	15.258	406.1311605			
R13	13.897	14.987	14.442	453.3220582			
R13	14.48	14.17	14.325	460.7573501	440.4243023	20.33179934	745.4172
R13	15.539	14.17	14.8545	428.4947024			
R13	13.622	15.259	14.4405	453.4162403			

Table 8: Tabularized hardness calculation for a sample held for 45 min at 1000°C in an air environment and quenched in N$_2$ gas with a cooling rate of 200°C/s.

Indent row Nr.	d$_1$ [μm]	d$_2$ [μm]	d [μm]	Hardness [HV]	averaged [HV]	Std. dev. [HV]	Depth [μm]
R1	10.681	11.715	11.198	754.0160786			
R1	9.535	10.084	9.8095	982.5797062			
R1	9.902	10.639	10.2705	896.3515201	892.7860708	78.70019686	15.7694
R1	9.823	10.113	9.968	951.5803702			
R1	10.385	10.353	10.369	879.4026788			
R2	13.352	12.308	12.83	574.3917856			
R2	13.361	13.122	13.2415	539.246287			
R2	14.177	13.625	13.901	489.2935001	545.4531681	33.74077835	75.7694
R2	12.877	12.535	12.706	585.6576644			
R2	12.831	13.666	13.2485	538.6766034			
R3	13.35	14.177	13.7635	499.118605			
R3	13.897	13.352	13.6245	509.3547807			
R3	13.179	14.17	13.6745	505.6367393	533.6390677	38.75932148	135.7694
R3	12.535	12.544	12.5395	601.313693			
R3	12.532	13.625	13.0785	552.7715208			
R4	13.897	13.666	13.7815	497.81566			
R4	14.835	14.714	14.7745	433.147636			
R4	14.439	13.666	14.0525	478.8002244	483.7278636	27.16431849	195.7694
R4	13.352	14.167	13.7595	499.4088429			
R4	13.894	13.352	13.623	509.4669548			
R5	14.439	13.897	14.168	471.0255191			
R5	14.714	13.919	14.3165	461.3046347			
R5	14.167	13.622	13.8945	489.7514009	471.619692	21.99960466	255.7694
R5	13.897	13.625	13.761	499.299974			
R5	14.714	14.714	14.714	436.7169314			
R6	14.442	13.361	13.9015	489.2583035			
R6	14.177	14.984	14.5805	444.7507598			
R6	14.984	14.177	14.5805	444.7507598	460.373895	17.05688641	315.7694
R6	14.442	13.937	14.1895	469.5992001			
R6	14.439	14.439	14.439	453.5104517			
R7	13.625	14.722	14.1735	470.6600288			
R7	14.167	13.937	14.052	478.8342984			
R7	13.089	14.442	13.7655	498.9735809	472.6846434	15.70869846	375.7694
R7	14.994	13.622	14.308	461.852895			
R7	13.897	14.994	14.4455	453.102414			
R8	14.442	14.167	14.3045	462.0789334			
R8	14.714	13.622	14.168	471.0255191			
R8	14.439	14.209	14.324	460.821686	465.352405	4.509735645	435.7694
R8	14.167	14.439	14.303	462.1758578			
R8	14.722	13.625	14.1735	470.6600288			
R9	14.17	13.625	13.8975	489.5399822			
R9	14.167	13.35	13.7585	499.481442			
R9	13.894	14.714	14.304	462.1112381	482.1802557	13.80774365	495.7694
R9	14.17	13.625	13.8975	489.5399822			
R9	14.19	14.17	14.18	470.2286341			
R10	13.897	13.35	13.6235	509.4295593			
R10	13.625	15.532	14.5785	444.8727974			
R10	14.984	14.167	14.5755	445.055948	474.3598276	32.97634505	555.7694
R10	13.08	13.905	13.4925	519.3697842			
R10	14.45	14.442	14.446	453.0710493			
R11	14.17	13.622	13.896	489.6456745			
R11	14.19	13.625	13.9075	488.8362411			
R11	13.625	14.714	14.1695	470.9257977	476.4179166	10.99531522	615.7694
R11	13.897	14.442	14.1695	470.9257977			
R11	13.905	14.714	14.3095	461.7560722			
R12	14.714	14.45	14.582	444.6592646			
R12	14.19	14.714	14.452	452.6949267			
R12	14.167	14.17	14.1685	470.9922751	458.3063426	10.54873295	675.7694
R12	14.19	14.712	14.451	452.7575812			
R12	14.177	14.177	14.177	470.4276656			
R13	13.622	14.722	14.172	470.7596658			
R13	14.712	13.622	14.167	471.0920176			
R13	13.894	14.722	14.308	461.852895	472.9738987	13.83305415	735.7694
R13	13.897	13.622	13.7595	499.4088429			
R13	14.177	14.442	14.3095	461.7560722			

Table 9: Tabularized hardness calculation for a sample held for 45 min at 1050°C in an air environment and quenched in N_2 gas with a cooling rate of 200°C/s.

Indent row Nr.	d_1 [µm]	d_2 [µm]	d [µm]	Hardness [HV]	averaged [HV]	Std. dev. [HV]	Depth [µm]
R1	12.877	12.037	12.457	609.3048068			
R1	12.098	12	12.049	651.2676772			
R1	12.263	12.335	12.299	625.0603203	641.1268507	51.26370968	30.6042
R1	12.877	12.535	12.706	585.6576644			
R1	11.494	11.2	11.347	734.3437847			
R2	12.816	12.559	12.6875	587.3668373			
R2	12.544	12.606	12.575	597.923394			
R2	14.261	12.015	13.138	547.7760224	589.4867805	25.42018258	90.6042
R2	13.089	12.287	12.688	587.3205452			
R2	12	12.559	12.2795	627.0471038			
R3	12.831	13.647	13.239	539.4499645			
R3	13.633	13.375	13.504	518.4855707			
R3	12.816	13.103	12.9595	562.9697261	545.2635656	21.26495283	150.6042
R3	13.08	12.544	12.812	576.0068832			
R3	13.625	13.103	13.364	529.4056833			
R4	13.375	12.263	12.819	575.3779812			
R4	13.089	12.638	12.8635	571.4039411			
R4	13.089	13.625	13.357	529.9607197	572.9842327	23.76027416	210.6042
R4	11.743	13.361	12.552	600.1166441			
R4	12.544	12.816	12.68	588.0618774			
R5	13.419	13.394	13.4065	526.0544614			
R5	14.462	13.361	13.9115	488.5551695			
R5	12.065	13.937	13.001	559.3813936	537.3571018	27.58947875	270.6042
R5	13.647	12.58	13.1135	549.8247583			
R5	12.272	13.647	12.9595	562.9697261			
R6	13.089	12.816	12.9525	563.578389			
R6	12.808	13.897	13.3525	530.3179899			
R6	13.361	13.352	13.3565	530.0003986	536.1233348	13.7768947	330.6042
R6	12.851	13.937	13.394	527.0368041			
R6	13.905	12.816	13.3605	529.6830925			
R7	13.919	14.19	14.0545	478.6639645			
R7	13.937	13.633	13.785	497.5629022			
R7	13.647	13.361	13.504	518.4855707	512.7367451	22.117288	390.6042
R7	13.666	13.089	13.3775	528.3377154			
R7	12.816	13.633	13.2245	540.6335726			
R8	14.722	14.167	14.4445	453.1651532			
R8	13.625	13.937	13.781	497.851784			
R8	14.48	13.633	14.0565	478.5277628	493.3031683	24.97346414	450.6042
R8	13.089	13.919	13.504	518.4855707			
R8	13.919	13.089	13.504	518.4855707			
R9	13.905	14.19	14.0475	479.1411288			
R9	14.722	13.077	13.8995	489.3991125			
R9	13.361	13.361	13.361	529.6434492	511.5148701	23.40984099	510.6042
R9	13.633	12.831	13.232	540.0208757			
R9	13.352	13.633	13.4925	519.3697842			
R10	13.919	13.919	13.919	488.0288132			
R10	12.559	13.394	12.9765	561.4956435			
R10	13.375	13.633	13.504	518.4855707	521.0225302	24.14886585	570.6042
R10	12.808	13.961	13.3845	527.785226			
R10	14.17	13.08	13.625	509.3173975			
R11	13.394	13.905	13.6495	507.4906526			
R11	13.633	13.103	13.368	529.088911			
R11	13.08	14.462	13.771	498.5750903	502.405951	16.3245779	630.6042
R11	14.45	13.103	13.7765	498.1770769			
R11	13.666	14.442	14.054	478.698024			
R12	14.503	13.633	14.068	477.7457298			
R12	13.361	13.394	13.3775	528.3377154			
R12	14.19	13.647	13.9185	488.0638772	494.3334975	18.60791481	690.6042
R12	13.633	13.905	13.769	498.7199407			
R12	13.625	14.48	14.0525	478.8002244			
R13	14.462	14.19	14.326	460.6930277			
R13	13.647	13.375	13.511	517.9484589			
R13	13.103	14.734	13.9185	488.0638772	491.529434	28.11501448	750.6042
R13	13.361	13.375	13.368	529.088911			
R13	14.994	13.622	14.308	461.852895			

Table 10: Tabularized hardness calculation for a sample held for 45 min at 1100°C in an air environment and quenched in N_2 gas with a cooling rate of 200°C/s.

Indent row Nr.	d_1 [μm]	d_2 [μm]	d [μm]	Hardness [HV]	averaged [HV]	Std. dev. [HV]	Depth [μm]
R1	9.267	10.629	9.948	955.4104342			
R1	11.446	10.095	10.7705	815.0604183			
R1	10.113	10.911	10.512	855.6395069	850.5683147	56.49298121	34.8088
R1	10.657	10.629	10.643	834.705757			
R1	11.223	10.629	10.926	792.0254571			
R2	12.816	10.898	11.857	672.5303585			
R2	11.446	11.728	11.587	704.2381034			
R2	11.743	11.455	11.599	702.7816872	693.6690049	12.15537152	94.8088
R2	11.728	11.494	11.611	701.3297843			
R2	12	11.455	11.7275	687.4650911			
R3	12.263	12.606	12.4345	611.5118536			
R3	13.08	12.287	12.6835	587.7373719			
R3	12.272	12.816	12.544	600.8823431	610.8633445	17.77143462	154.8088
R3	12.808	11.472	12.14	641.5406203			
R3	12.831	12.015	12.423	612.6445335			
R4	12.816	12.532	12.674	588.6187981			
R4	12.532	12.535	12.5335	601.889549			
R4	12.816	12.26	12.538	601.4575795	609.6792211	18.06222701	214.8088
R4	12.263	12.544	12.4035	614.5723699			
R4	12.559	11.715	12.137	641.857809			
R5	11.728	12.272	12	656.5972222			
R5	13.089	11.99	12.5395	601.313693			
R5	12.808	13.089	12.9485	563.9266396	590.0514739	36.25843132	274.8088
R5	13.08	12.805	12.9425	564.4496211			
R5	12.544	13.352	12.948	563.9701936			
R6	12.816	12.263	12.5395	601.313693			
R6	12.535	13.633	13.084	552.3068915			
R6	12.831	12.544	12.6875	587.3668373	594.1210803	24.85824623	334.8088
R6	12.272	12.816	12.544	600.8823431			
R6	12.263	12.263	12.263	628.7356364			
R7	12.015	13.08	12.5475	600.5471696			
R7	12.808	12.544	12.676	588.43307			
R7	12	13.08	12.54	601.2657423	593.0650889	10.47982173	394.8088
R7	12.851	12.808	12.8295	574.4365577			
R7	11.99	13.103	12.5465	600.6429049			
R8	13.089	14.177	13.633	508.7198264			
R8	12.535	12.263	12.399	615.0185474			
R8	13.352	13.077	13.2145	541.4521252	553.983813	35.14626107	454.8088
R8	12.831	13.08	12.9555	563.3174126			
R8	13.08	13.35	13.215	541.4111534			
R9	13.103	13.375	13.239	539.4499645			
R9	13.08	13.361	13.2205	540.9607707			
R9	12.831	13.089	12.96	562.9262879	561.4255239	19.03341178	514.8088
R9	12.831	12.535	12.683	587.7837134			
R9	12.808	12.816	12.812	576.0068832			
R10	13.352	12.808	13.08	552.6447456			
R10	12.535	13.08	12.8075	576.411722			
R10	13.089	13.089	13.089	551.8850095	561.8377387	11.57538682	574.8088
R10	12.808	13.352	13.08	552.6447456			
R10	13.089	12.544	12.8165	575.6024708			
R11	12.544	12.544	12.544	600.8823431			
R11	13.122	12.808	12.965	562.4921824			
R11	13.08	13.103	13.0915	551.6742497	570.8966016	19.71002876	634.8088
R11	13.361	12.805	13.083	552.391326			
R11	12.26	13.122	12.691	587.0429069			
R12	12	13.089	12.5445	600.834444			
R12	13.089	13.077	13.083	552.391326			
R12	12	13.103	12.5515	600.1644574	580.8208413	18.13774733	694.8088
R12	13.08	12.535	12.8075	576.411722			
R12	12.287	13.375	12.831	574.3022572			
R13	13.352	12	12.676	588.43307			
R13	13.633	13.103	13.368	529.088911			
R13	13.905	12.272	13.0885	551.927176	564.1651112	22.53232636	754.8088
R13	12.535	13.375	12.955	563.3608961			
R13	13.089	12.272	12.6805	588.015503			

Table 11: Tabularized hardness calculation for a sample held for 45 min at 1150°C in an air environment and quenched in N_2 gas with a cooling rate of 200°C/s.

Indent row Nr.	d_1 [μm]	d_2 [μm]	d [μm]	Hardness [HV]	averaged [HV]	Std. dev. [HV]	Depth [μm]
R1	11.183	12.015	11.599	702.7816872			
R1	11.455	10.41	10.9325	791.0839277			
R1	12.263	12.287	12.275	627.5069375	711.9779456	52.98098561	24.208
R1	11.728	11.446	11.587	704.2381034			
R1	11.223	11.472	11.3475	734.279072			
R2	12.287	11.99	12.1385	641.6991852			
R2	11.173	11.494	11.3335	736.094267			
R2	12.816	12	12.408	614.1266777	660.2905197	41.96149591	84.208
R2	12	12.335	12.1675	638.6439808			
R2	11.743	12	11.8715	670.8884876			
R3	12.816	13.089	12.9525	563.578389			
R3	12.831	11.718	12.2745	627.5580614			
R3	12.808	13.394	13.101	550.8744627	591.1120609	29.26945546	144.208
R3	12.831	12	12.4155	613.3849341			
R3	12.272	12.831	12.5515	600.1644574			
R4	13.122	12.58	12.851	572.516076			
R4	12.272	13.148	12.71	585.2890944			
R4	12.816	12.816	12.816	575.6473844	581.8133629	16.98342292	204.208
R4	13.103	12.816	12.9595	562.9697261			
R4	12.559	12.287	12.423	612.6445335			
R5	12.272	12.559	12.4155	613.3849341			
R5	13.375	12.808	13.0915	551.6742497			
R5	12.535	12.831	12.683	587.7837134	566.84774	29.90460053	264.208
R5	12.816	13.352	13.084	552.3068915			
R5	13.633	13.103	13.368	529.088911			
R6	12.58	11.987	12.2835	626.638787			
R6	11.99	13.361	12.6755	588.4794938			
R6	13.089	13.08	13.0845	552.2646816	567.2714946	35.77241596	324.208
R6	13.103	13.375	13.239	539.4499645			
R6	13.375	13.35	13.3625	529.5245463			
R7	12.808	13.122	12.965	562.4921824			
R7	13.122	14.19	13.656	507.0076555			
R7	12.544	12.287	12.4155	613.3849341	559.2502834	33.91467755	384.208
R7	13.122	12.808	12.965	562.4921824			
R7	13.08	13.122	13.101	550.8744627			
R8	13.103	13.08	13.0915	551.6742497			
R8	12.272	13.122	12.697	586.4882207			
R8	13.361	12.831	13.096	551.2951863	560.9686921	16.75955063	444.208
R8	12.805	13.633	13.219	541.0835466			
R8	12.831	12.831	12.831	574.3022572			
R9	13.089	13.419	13.254	538.2296279			
R9	13.375	12.831	13.103	550.7063081			
R9	12.808	13.122	12.965	562.4921824	550.8142711	10.49463571	504.208
R9	13.375	13.089	13.232	540.0208757			
R9	12.805	13.122	12.9635	562.6223613			
R10	12.877	12.816	12.8465	572.9172395			
R10	13.077	12.559	12.818	575.4677613			
R10	13.352	12.831	13.0915	551.6742497	558.2933685	16.86258332	564.208
R10	12.559	13.375	12.967	562.3186808			
R10	13.647	13.089	13.368	529.088911			
R11	12.535	12.831	12.683	587.7837134			
R11	12.831	13.633	13.232	540.0208757			
R11	12.808	12.808	12.808	576.3667188	556.6253816	22.09166717	624.208
R11	12.851	13.375	13.113	549.8666889			
R11	13.375	13.361	13.368	529.088911			
R12	12.816	13.103	12.9595	562.9697261			
R12	12.544	12.26	12.402	614.7210417			
R12	12.816	13.122	12.969	562.1452595	566.4502107	27.35761944	684.208
R12	13.375	12.544	12.9595	562.9697261			
R12	12.808	13.919	13.3635	529.4452998			
R13	12.559	12.544	12.5515	600.1644574			
R13	12.272	13.361	12.8165	575.6024708			
R13	13.394	12.544	12.969	562.1452595	568.2437099	18.22508583	744.208
R13	12.287	13.897	13.092	551.6321123			
R13	13.103	13.08	13.0915	551.6742497			

Table 12: Tabularized hardness calculation for a sample held for 45 min at 1200°C in an air environment and quenched in N_2 gas with a cooling rate of 200°C/s.

Indent row Nr.	d_1 [μm]	d_2 [μm]	d [μm]	Hardness [HV]	averaged [HV]	Std. dev. [HV]	Depth [μm]
R1	9.007	9.812	9.4095	1067.894722			
R1	9.823	9.363	9.593	1027.43095			
R1	8.995	9.551	9.273	1099.565269	1020.896528	61.10261311	22.6372
R1	9.812	9.812	9.812	982.0790669			
R1	9.808	10.385	10.0965	927.5126339			
R2	11.728	11.2	11.464	719.4310512			
R2	9.597	11.446	10.5215	854.0950682			
R2	11.446	9.808	10.627	837.2211134	795.8797001	47.66326561	82.6372
R2	10.639	11.2	10.9195	792.9686684			
R2	11.17	10.911	11.0405	775.6825991			
R3	11.223	11.455	11.339	735.3803528			
R3	12	10.911	11.4555	720.4990854			
R3	11.446	11.728	11.587	704.2381034	700.149893	32.09669379	142.6372
R3	11.253	12	11.6265	699.4610593			
R3	12.559	11.728	12.1435	641.1708638			
R4	11.743	12.037	11.89	668.8024016			
R4	10.356	11.494	10.925	792.170457			
R4	10.356	10.353	10.3545	881.8673593	716.5014884	112.5412111	202.6372
R4	11.183	12.263	11.723	687.9929742			
R4	12.808	13.375	13.0915	551.6742497			
R5	12.851	12.335	12.593	596.2153135			
R5	12.263	12.544	12.4035	614.5723699			
R5	12.559	12.535	12.547	600.5950344	592.8142905	14.75307069	262.6372
R5	13.077	12.532	12.8045	576.6818516			
R5	12.535	13.089	12.812	576.0068832			
R6	12.263	11.99	12.1265	642.969824			
R6	10.911	12.535	11.723	687.9929742			
R6	12.287	12.037	12.162	639.2217372	626.4917906	42.40321624	322.6372
R6	11.455	13.666	12.5605	599.3046915			
R6	12.544	13.375	12.9595	562.9697261			
R7	11.718	12.851	12.2845	626.5367701			
R7	12.816	13.666	13.241	539.2870133			
R7	12	13.666	12.833	574.1232632	596.1402707	34.42803599	382.6372
R7	12.544	12	12.272	627.8137744			
R7	12.26	12.58	12.42	612.9405328			
R8	12.272	10.911	11.5915	703.6914173			
R8	12.26	12.308	12.284	626.5877754			
R8	13.375	13.919	13.647	507.6766045	598.4905965	81.65756436	442.6372
R8	12.015	12	12.0075	655.7772445			
R8	13.361	14.177	13.769	498.7199407			
R9	11.718	13.352	12.535	601.7455075			
R9	12.851	11.715	12.283	626.6898048			
R9	12.015	12.263	12.139	641.6463237	604.0240227	26.89676267	502.6372
R9	13.122	12.532	12.827	574.6604964			
R9	12.535	13.103	12.819	575.3779812			
R10	13.103	12.831	12.967	562.3186808			
R10	12	13.089	12.5445	600.834444			
R10	12.544	13.103	12.8235	574.9742308	591.6287182	35.58144923	562.6372
R10	11.728	12.263	11.9955	657.0899473			
R10	13.089	12.831	12.96	562.9262879			
R11	12.287	13.122	12.7045	585.7959679			
R11	12.559	12.532	12.5455	600.738663			
R11	12.287	13.419	12.853	572.3379164	591.7491404	14.06294594	622.6372
R11	12.816	12.015	12.4155	613.3849341			
R11	12.272	13.122	12.697	586.4882207			
R12	12.535	12.037	12.286	626.3837914			
R12	12.544	11.794	12.169	638.4865469			
R12	11.743	12.58	12.1615	639.2742993	629.1922727	23.03054256	682.6372
R12	12.851	12.535	12.693	586.8579241			
R12	12.015	12.015	12.015	654.9588018			
R13	11.99	12	11.995	657.1447287			
R13	12.037	12.559	12.298	625.1619768			
R13	12.831	12.535	12.683	587.7837134	625.1151443	28.52050284	742.6372
R13	11.99	12.015	12.0025	656.3237255			
R13	12.816	12.308	12.562	599.1615768			

Table 13: Tabularized hardness calculation for a sample held for 45 min at 1250°C in an air environment and quenched in N_2 gas with a cooling rate of 200°C/s.

Indent row Nr.	d₁ [µm]	d₂ [µm]	d [µm]	Hardness [HV]	averaged [HV]	Std. dev. [HV]	Depth [µm]
R1	8.735	10.084	9.4095	1067.894722			
R1	9.539	9.539	9.539	1039.096389			
R1	10.084	9.808	9.946	955.7947119	989.5199993	53.78208325	38.901
R1	10.084	9.823	9.9535	954.3548647			
R1	9.808	10.353	10.0805	930.459309			
R2	10.08	9.267	9.6735	1010.402149			
R2	9.028	10.356	9.692	1006.548538			
R2	11.17	11.183	11.1765	756.9198389	887.2169378	112.9216087	98.901
R2	10.901	11.455	11.178	756.7167071			
R2	10.898	9.539	10.2185	905.4974563			
R3	10.901	11.443	11.172	757.5297253			
R3	11.17	10.901	11.0355	776.3856559			
R3	9.263	10.629	9.946	955.7947119	849.6928876	98.17274095	158.901
R3	11.173	10.901	11.037	776.1746385			
R3	9.539	10.08	9.8095	982.5797062			
R4	11.718	11.446	11.582	704.84628			
R4	11.173	11.987	11.58	705.0897712			
R4	10.629	9.539	10.084	929.8135251	800.3792095	97.89998516	218.901
R4	9.812	10.625	10.2185	905.4974563			
R4	11.446	10.911	11.1785	756.6490147			
R5	11.728	12	11.864	671.7369795			
R5	11.446	11.183	11.3145	738.5685317			
R5	11.455	11.443	11.449	721.317423	748.3703157	106.4016036	278.901
R5	10.356	9.57	9.963	952.5357241			
R5	11.99	11.99	11.99	657.6929204			
R6	11.443	11.17	11.3065	739.614061			
R6	11.99	11.715	11.8525	673.0411302			
R6	12.532	11.718	12.125	643.1289191	695.0774982	53.75776771	338.901
R6	11.715	12.532	12.1235	643.2880733			
R6	11.443	10.629	11.036	776.3153072			
R7	11.715	12.535	12.125	643.1289191			
R7	11.718	11.718	11.718	688.5802243			
R7	12.26	12.535	12.3975	615.1673812	668.6768654	42.54562366	398.901
R7	12.263	11.728	11.9955	657.0899473			
R7	10.901	11.715	11.308	739.4178552			
R8	12.26	11.443	11.8515	673.1547141			
R8	11.728	12.263	11.9955	657.0899473			
R8	11.718	11.443	11.5805	705.0288866	670.1412005	20.6441573	458.901
R8	11.455	12.263	11.859	672.3035354			
R8	12.535	11.715	12.125	643.1289191			
R9	12.287	11.987	12.137	641.857809			
R9	12.535	11.728	12.1315	642.4399329			
R9	12.263	11.715	11.989	657.802641	642.9811669	15.55417921	518.901
R9	12.535	12.26	12.3975	615.1673812			
R9	11.718	12.263	11.9905	657.6380703			
R10	11.173	12.287	11.73	687.1720852			
R10	12	12.544	12.272	627.8137744			
R10	12.532	11.443	11.9875	657.9672734	666.8319025	22.38291887	578.901
R10	11.443	12.26	11.8515	673.1547141			
R10	12.272	11.173	11.7225	688.0516654			
R11	12.263	11.446	11.8545	672.8140487			
R11	11.728	12.808	12.268	628.2232404			
R11	12.816	11.728	12.272	627.8137744	648.8323609	20.29949886	638.901
R11	11.718	11.99	11.854	672.8708083			
R11	12	12.263	12.1315	642.4399329			
R12	11.446	11.443	11.4445	721.8847814			
R12	12.26	11.173	11.7165	688.756546			
R12	11.718	12.532	12.125	643.1289191	662.3517236	38.01842562	698.901
R12	12.535	11.718	12.1265	642.969824			
R12	12.263	12.535	12.399	615.0185474			
R13	12.532	11.987	12.2595	629.0946868			
R13	11.173	12	11.5865	704.2988856			
R13	11.715	12.263	11.989	657.802641	667.2200327	26.42747775	758.901
R13	11.446	12.559	12.0025	656.3237255			
R13	11.99	11.446	11.718	688.5802243			

Table 14: Tabularized hardness calculation for a sample held for 45 min at 1300°C in an air environment and quenched in N_2 gas with a cooling rate of 200°C/s.

Indent row Nr.	d_1 [μm]	d_2 [μm]	d [μm]	Hardness [HV]	averaged [HV]	Std. dev. [HV]	Depth [μm]
R1	8.173	8.718	8.4455	1325.594827			
R1	8.214	7.628	7.921	1506.959243			
R1	8.173	8.45	8.3115	1368.682501	1386.473076	62.34319916	24.3372
R1	8.756	7.905	8.3305	1362.446306			
R1	7.901	8.722	8.3115	1368.682501			
R2	9.535	8.722	9.1285	1134.652027			
R2	8.735	8.995	8.865	1203.106445			
R2	9.267	8.722	8.9945	1168.71194	1175.855072	42.57048258	84.3372
R2	8.45	8.995	8.7225	1242.737996			
R2	9.299	8.995	9.147	1130.066953			
R3	8.718	10.356	9.537	1039.532252			
R3	9.808	10.356	10.082	930.1824622			
R3	8.995	9.812	9.4035	1069.257919	980.2588718	69.35536683	144.3372
R3	9.535	10.084	9.8095	982.5797062			
R3	9.551	11.183	10.367	879.74202			
R4	10.639	8.735	9.687	1007.587877			
R4	9.267	10.356	9.8115	982.1791641			
R4	10.356	8.995	9.6755	1009.984476	977.5474062	50.2742126	204.3372
R4	9.267	10.095	9.681	1008.837211			
R4	10.657	10.084	10.3705	879.1483018			
R5	10.08	11.728	10.904	795.2246754			
R5	12.263	11.99	12.1265	642.969824			
R5	10.356	11.183	10.7695	815.2117899	765.2494594	64.70923171	264.3372
R5	11.455	10.08	10.7675	815.5146597			
R5	11.446	10.901	11.1735	757.326348			
R6	11.734	11.173	11.4535	720.7507332			
R6	11.446	11.99	11.718	688.5802243			
R6	11.455	11.715	11.585	704.4812796	721.9820988	24.34018758	324.3372
R6	10.629	11.715	11.172	757.5297253			
R6	11.99	10.639	11.3145	738.5685317			
R7	12.015	11.728	11.8715	670.8884876			
R7	10.639	10.08	10.3595	881.0163003			
R7	11.728	12.559	12.1435	641.1708638	695.657771	93.74998346	384.3372
R7	12.263	12.26	12.2615	628.8894775			
R7	12.559	11.446	12.0025	656.3237255			
R8	12.535	12.015	12.275	627.5069375			
R8	11.718	11.728	11.723	687.9929742			
R8	11.718	10.898	11.308	739.4178552	680.4096097	41.0915477	444.3372
R8	11.987	11.17	11.5785	705.2724725			
R8	12.559	11.715	12.137	641.857809			
R9	11.718	12.816	12.267	628.3256695			
R9	11.446	11.446	11.446	721.6955876			
R9	11.17	11.443	11.3065	739.614061	674.6336678	49.87661907	504.3372
R9	12.287	12.559	12.423	612.6445335			
R9	12.015	11.728	11.8715	670.8884876			
R10	11.728	11.99	11.859	672.3035354			
R10	11.455	11.718	11.5865	704.2988856			
R10	11.443	11.718	11.5805	705.0288866	667.7524031	38.4095571	564.3372
R10	11.99	13.103	12.5465	600.6429049			
R10	12.015	11.987	12.001	656.487803			
R11	11.99	11.718	11.854	672.8708083			
R11	11.446	12.26	11.853	672.9843491			
R11	11.455	10.911	11.183	756.0401914	692.4739913	34.98789569	624.3372
R11	11.99	11.99	11.99	657.6929204			
R11	12.015	11.183	11.599	702.7816872			
R12	11.718	11.987	11.8525	673.0411302			
R12	11.173	11.718	11.4455	721.7586439			
R12	12.263	12.535	12.399	615.0185474	653.273445	39.48245272	684.3372
R12	12.272	12.263	12.2675	628.2744518			
R12	12.272	12.263	12.2675	628.2744518			
R13	10.898	11.173	11.0355	776.3856559			
R13	11.743	11.446	11.5945	703.3273134			
R13	12.535	11.455	11.995	657.1447287	696.4350859	43.81490236	744.3372
R13	12.263	11.728	11.9955	657.0899473			
R13	11.987	11.455	11.721	688.227784			

Table 15: Tabularized hardness calculation for a sample held for 15 min at 1200°C in an air environment and quenched in N₂ gas with a cooling rate of 200°C/s.

Indent row Nr.	d₁ [μm]	d₂ [μm]	d [μm]	Hardness [HV]	averaged [HV]	Std. dev. [HV]	Depth [μm]
R1	10.481	11.987	11.234	749.1912459			
R1	11.728	11.559	11.6435	697.4200652			
R1	10.58	10.982	10.781	813.4735587	739.2874733	41.18996014	18.022
R1	11.794	10.982	11.388	729.0656153			
R1	11.381	11.743	11.562	707.2868816			
R2	12.037	11.532	11.7845	680.830827			
R2	12.77	12.58	12.675	588.5259231			
R2	12.065	12.638	12.3515	619.7579804	619.506179	43.7658127	78.022
R2	12.946	13.103	13.0245	557.36464			
R2	12.308	11.794	12.051	651.0515246			
R3	12.335	12.638	12.4865	606.4291797			
R3	12.606	11.762	12.184	636.9154039			
R3	12.58	12.308	12.444	610.5785291	609.8420765	14.75990614	138.022
R3	12.851	12.407	12.629	592.8210369			
R3	12.72	12.335	12.5275	602.4662326			
R4	12.559	12.677	12.618	593.8550952			
R4	12.368	12.831	12.5995	595.600305			
R4	12.909	12.677	12.793	577.7191098	602.2923217	36.51298309	198.022
R4	12.184	11.523	11.8535	672.9275751			
R4	12.877	12.851	12.864	571.3595231			
R5	11.969	12.909	12.439	611.0694859			
R5	12.308	12.452	12.38	616.9077751			
R5	12.77	12.308	12.539	601.3616494	605.9984748	12.9200046	258.022
R5	13.103	12.368	12.7355	582.947619			
R5	12.138	12.606	12.372	617.7058445			
R6	12.606	13.841	13.2235	540.7153443			
R6	12.407	12.58	12.4935	605.749816			
R6	13.394	12.677	13.0355	556.4243732	578.0806169	29.72403816	318.022
R6	12.677	12.037	12.357	619.2064048			
R6	12.851	12.946	12.8985	568.3071463			
R7	12.72	12.851	12.7855	578.397091			
R7	13.103	12.677	12.89	569.0569063			
R7	12.452	13.394	12.923	566.1543448	572.5801393	12.33001404	378.022
R7	13.394	12.677	13.0355	556.4243732			
R7	12.677	12.58	12.6285	592.867981			
R8	13.148	12.877	13.0125	558.3931065			
R8	13.179	13.375	13.277	536.3664722			
R8	13.72	13.485	13.6025	511.0037227	553.9235411	28.53081693	438.022
R8	12.677	13.103	12.89	569.0569063			
R8	13.179	12.037	12.608	594.7974978			
R9	13.215	13.961	13.588	512.0949072			
R9	13.449	12.638	13.0435	555.7420364			
R9	13.69	12.287	12.9885	560.4585976	555.8954034	23.66653356	498.022
R9	12.851	12.638	12.7445	582.1245697			
R9	12.677	13.103	12.89	569.0569063			
R10	13.69	13.148	13.419	525.0748626			
R10	12.909	13.419	13.164	545.6143524			
R10	13.666	13.215	13.4405	523.3963417	527.7344997	17.8862188	558.022
R10	13.625	13.937	13.781	497.851784			
R10	13.122	13.179	13.1505	546.7351576			
R11	13.449	13.666	13.5575	514.4015955			
R11	14.295	13.215	13.755	499.7356634			
R11	12.877	13.148	13.0125	558.3931065	537.101438	24.96612445	618.022
R11	13.394	12.677	13.0355	556.4243732			
R11	12.946	13.122	13.034	556.5524512			
R12	13.99	13.215	13.6025	511.0037227			
R12	13.179	13.103	13.141	547.5259439			
R12	13.961	12.909	13.435	523.8249638	532.5099551	18.404994	678.022
R12	13.305	13.666	13.4855	519.9091089			
R12	13.375	12.606	12.9905	560.286036			
R13	12.909	13.666	13.2875	535.519116			
R13	13.72	13.841	13.7805	497.887912			
R13	13.215	13.122	13.1685	545.2415165	519.82025	20.27996703	738.022
R13	13.666	13.148	13.407	526.0152248			
R13	13.72	13.937	13.8285	494.4374809			

Table 16: Tabularized hardness calculation for a sample held for 30 min at 1200°C in an air environment and quenched in N_2 gas with a cooling rate of 200°C/s.

Indent row Nr.	d₁ [µm]	d₂ [µm]	d [µm]	Hardness [HV]	averaged [HV]	Std. dev. [HV]	Depth [µm]
R1	10.625	11.494	11.0595	773.0196741			
R1	11.728	10.367	11.0475	774.6999228			
R1	10.095	11.183	10.639	835.3335323	814.8588915	34.38987492	17.889
R1	10.657	10.356	10.5065	856.535571			
R1	10.629	10.657	10.643	834.705757			
R2	11.728	11.455	11.5915	703.6914173			
R2	10.952	11.446	11.199	753.8814269			
R2	12	10.911	11.4555	720.4990854	755.8631735	44.64941107	77.889
R2	10.367	10.952	10.6595	832.1236499			
R2	11.223	10.952	11.0875	769.1202882			
R3	11.446	11.472	11.459	720.0590188			
R3	12.287	11.455	11.871	670.9450037			
R3	11.455	12.544	11.9995	656.6519421	675.4138167	32.6781565	137.889
R3	11.472	11.743	11.6075	701.7527909			
R3	12.26	12.287	12.2735	627.6603278			
R4	12.816	13.089	12.9525	563.578389			
R4	11.987	12.808	12.3975	615.1673812			
R4	11.743	12.532	12.1375	641.8049279	620.7792414	30.39272663	197.889
R4	11.99	12.287	12.1385	641.6991852			
R4	12.015	12.263	12.139	641.6463237			
R5	11.99	12.272	12.131	642.4928925			
R5	11.743	11.987	11.865	671.6237543			
R5	12.544	11.743	12.1435	641.1708638	650.5323539	17.83102878	257.889
R5	12.58	11.99	12.285	626.485771			
R5	11.743	12	11.8715	670.8884876			
R6	12.808	12.544	12.676	588.43307			
R6	12.808	12.544	12.676	588.43307			
R6	11.99	12.805	12.3975	615.1673812	615.1392595	23.88060431	317.889
R6	12.559	11.718	12.1385	641.6991852			
R6	12.272	12	12.136	641.9635908			
R7	12	12.015	12.0075	655.7772445			
R7	12.335	12.535	12.435	611.4626779			
R7	12.816	12.544	12.68	588.0618774	625.451972	32.55870643	377.889
R7	12.272	11.455	11.8635	671.7936029			
R7	12.831	12.272	12.5515	600.1644574			
R8	12.272	13.08	12.676	588.43307			
R8	11.99	12.535	12.2625	628.7869105			
R8	12.272	12.287	12.2795	627.0471038	614.3557392	14.43820731	437.889
R8	12.287	12.544	12.4155	613.3849341			
R8	12.272	12.544	12.408	614.1266777			
R9	11.987	12.831	12.409	614.0277008			
R9	12.544	12.805	12.6745	588.5723578			
R9	12.816	12.272	12.544	600.8823431	593.4007448	17.23490223	497.889
R9	13.089	12.831	12.96	562.9262879			
R9	12.535	12.559	12.547	600.5950344			
R10	12.015	11.99	12.0025	656.3237255			
R10	13.622	12.851	13.2365	539.6537574			
R10	12.816	12.805	12.8105	576.141782	587.1791051	39.95841647	557.889
R10	12.26	12.816	12.538	601.4575795			
R10	13.103	12.831	12.967	562.3186808			
R11	12.535	12.544	12.5395	601.313693			
R11	12.26	12.272	12.266	628.4281236			
R11	12.263	13.361	12.812	576.0068832	604.0861123	26.80656082	617.889
R11	12.831	12.831	12.831	574.3022572			
R11	12.015	12.287	12.151	640.3796043			
R12	13.352	13.077	13.2145	541.4521252			
R12	12.816	12.535	12.6755	588.4794938			
R12	12.816	13.352	13.084	552.3068915	567.6689926	29.11822647	677.889
R12	12.544	12.263	12.4035	614.5723699			
R12	13.35	13.077	13.2135	541.5340826			
R13	13.633	13.625	13.629	509.0184804			
R13	13.103	13.352	13.2275	540.3883688			
R13	12.808	13.633	13.2205	540.9607707	543.955225	25.58883122	737.889
R13	13.352	11.99	12.671	588.8975552			
R13	13.077	13.375	13.226	540.5109498			

Table 17: Tabularized hardness calculation for a sample held for 60 min at 1200°C in an air environment and quenched in N_2 gas with a cooling rate of 200°C/s.

Indent row Nr.	d_1 [μm]	d_2 [μm]	d [μm]	Hardness [HV]	averaged [HV]	Std. dev. [HV]	Depth [μm]
R1	10.367	10.367	10.367	879.74202			
R1	10.657	10.385	10.521	854.1762502			
R1	9.539	9.842	9.6905	1006.860171	833.5411998	114.1740708	25.6352
R1	12.037	11.718	11.8775	670.210851			
R1	10.901	11.455	11.178	756.7167071			
R2	11.2	11.455	11.3275	736.8742688			
R2	11.455	11.718	11.5865	704.2988856			
R2	11.472	11.173	11.3225	737.5252178	694.5569611	40.83099307	85.6352
R2	11.743	12.559	12.151	640.3796043			
R2	12.335	11.718	12.0265	653.7068291			
R3	11.728	12.559	12.1435	641.1708638			
R3	11.743	12.287	12.015	654.9588018			
R3	11.718	12.015	11.8665	671.4539701	671.1100487	31.77558133	145.6352
R3	11.289	11.446	11.3675	731.6975611			
R3	12.263	11.743	12.003	656.2690467			
R4	12.263	12.263	12.263	628.7356364			
R4	13.103	12.272	12.6875	587.3668373			
R4	12.287	11.718	12.0025	656.3237255	620.6372965	34.21712221	205.6352
R4	11.99	12.015	12.0025	656.3237255			
R4	12.851	12.808	12.8295	574.4365577			
R5	12.26	12.831	12.5455	600.738663			
R5	11.99	12.816	12.403	614.6219212			
R5	12.272	13.361	12.8165	575.6024708	609.7870691	26.7981068	265.6352
R5	12.263	11.728	11.9955	657.0899473			
R5	12.272	12.816	12.544	600.8823431			
R6	12.26	12.831	12.5455	600.738663			
R6	11.99	12.816	12.403	614.6219212			
R6	12.272	13.361	12.8165	575.6024708	609.7870691	26.7981068	325.6352
R6	12.263	11.728	11.9955	657.0899473			
R6	12.272	12.816	12.544	600.8823431			
R7	12.544	12.535	12.5395	601.313693			
R7	12.015	12.559	12.287	626.2818368			
R7	13.375	12.272	12.8235	574.9742308	600.9315279	18.3886759	385.6352
R7	12.831	12.544	12.6875	587.3668373			
R7	12.272	12.532	12.402	614.7210417			
R8	12	13.625	12.8125	575.9619274			
R8	12.877	12.263	12.57	598.3991636			
R8	12.808	12.544	12.676	588.43307	585.110421	8.731717523	445.6352
R8	12.535	12.831	12.683	587.7837134			
R8	12.544	13.103	12.8235	574.9742308			
R9	12.831	13.103	12.967	562.3186808			
R9	12.559	12.851	12.705	585.7498613			
R9	12.559	12.272	12.4155	613.3849341	580.0729928	18.71719215	505.6352
R9	13.08	12.559	12.8195	575.333099			
R9	12.544	13.361	12.9525	563.578389			
R10	12.816	13.089	12.9525	563.578389			
R10	13.089	12.544	12.8165	575.6024708			
R10	12.808	12.816	12.812	576.0068832	568.9595	23.05589907	565.6352
R10	12.544	12.559	12.5515	600.1644574			
R10	13.352	13.375	13.3635	529.4452998			
R11	12.808	12.037	12.4225	612.6938518			
R11	12.26	12.535	12.3975	615.1673812			
R11	13.08	12.535	12.8075	576.411722	573.0291071	39.85378686	625.6352
R11	13.919	13.35	13.6345	508.6078989			
R11	13.089	13.08	13.0845	552.2646816			
R12	13.08	12.816	12.948	563.9701936			
R12	13.419	13.625	13.522	517.1061108			
R12	12	12.831	12.4155	613.3849341	569.3105744	34.49788257	685.6352
R12	12.831	12.272	12.5515	600.1644574			
R12	12.544	13.633	13.0885	551.927176			
R13	13.625	12.816	13.2205	540.9607707			
R13	12.805	13.08	12.9425	564.4496211			
R13	12.831	12.808	12.8195	575.333099	563.9489497	12.57055313	745.6352
R13	12.287	13.35	12.8185	575.4228686			
R13	13.361	12.544	12.9525	563.578389			

Table 18: Tabularized hardness calculation for a sample held for 75 min at 1200°C in an air environment and quenched in N_2 gas with a cooling rate of 200°C/s.

Indent row Nr.	d_1 [μm]	d_2 [μm]	d [μm]	Hardness [HV]	averaged [HV]	Std. dev. [HV]	Depth [μm]
R1	11.446	10.75	11.098	767.665622			
R1	8.995	9.028	9.0115	1164.306599			
R1	10.901	11.223	11.062	772.6703103	821.8321005	174.2010624	39.5028
R1	11.743	11.728	11.7355	686.5281312			
R1	11.728	11.223	11.4755	717.9898397			
R2	10.898	11.728	11.313	738.7643995			
R2	10.657	11.446	11.0515	774.1392317			
R2	11.99	11.718	11.854	672.8708083	787.2266745	80.31396451	99.5028
R2	10.095	10.41	10.2525	899.5016768			
R2	10.911	10.172	10.5415	850.8572563			
R3	11.728	13.089	12.4085	614.0771863			
R3	11.472	10.625	11.0485	774.559693			
R3	12.808	11.743	12.2755	627.4558199	678.3248061	57.61690217	159.5028
R3	11.482	11.718	11.6	702.6605232			
R3	11.173	12.535	11.854	672.8708083			
R4	11.183	12.532	11.8575	672.4736419			
R4	10.084	10.0928	10.0884	929.0026359			
R4	12.559	11.183	11.871	670.9450037	733.2998889	101.7900132	219.5028
R4	10.901	11.743	11.322	737.5903601			
R4	12.559	11.443	12.001	656.487803			
R5	11.455	11.446	11.4505	721.1284522			
R5	12.805	12.532	12.6685	589.130004			
R5	11.718	11.223	11.4705	718.6159208	662.2333117	51.46805446	279.5028
R5	12.287	12.26	12.2735	627.6603278			
R5	11.728	12.308	12.018	654.6318537			
R6	12.308	12.532	12.42	612.9405328			
R6	12.535	12.287	12.411	613.8298189			
R6	12.263	12.808	12.5355	601.6975051	613.5272282	8.257327773	339.5028
R6	11.446	13.103	12.2745	627.5580614			
R6	12.58	12.287	12.4335	611.6102227			
R7	11.715	12.037	11.876	670.3801639			
R7	11.99	12.535	12.2625	628.7869105			
R7	12.816	11.728	12.272	627.8137744	642.8010852	23.8348718	399.5028
R7	13.089	11.715	12.402	614.7210417			
R7	11.446	12.272	11.859	672.3035354			
R8	11.728	11.718	11.723	687.9929742			
R8	10.356	11.987	11.1715	757.5975359			
R8	12.263	11.987	12.125	643.1289191	667.0481085	55.62485214	459.5028
R8	11.7128	12.26	11.9864	658.0880432			
R8	12.272	13.08	12.676	588.43307			
R9	12.816	11.183	11.9995	656.6519421			
R9	11.728	12	11.864	671.7369795			
R9	12.544	11.99	12.267	628.3256695	634.0472285	26.67399748	519.5028
R9	12.308	12.808	12.558	599.54333			
R9	12.26	12.559	12.4095	613.9782214			
R10	12	11.99	11.995	657.1447287			
R10	12.559	12.535	12.547	600.5950344			
R10	12.015	12.532	12.2735	627.6603278	623.6373997	32.29043619	579.5028
R10	13.089	12.559	12.824	574.9293959			
R10	11.99	11.987	11.9885	657.8575116			
R11	12.544	12.544	12.544	600.8823431			
R11	13.089	12.851	12.97	562.0585789			
R11	12.544	12.816	12.68	588.0618774	595.5263139	19.1996533	639.5028
R11	11.99	12.808	12.399	615.0185474			
R11	12.308	12.559	12.4335	611.6102227			
R12	12	12.065	12.0325	653.0550505			
R12	11.987	11.183	11.585	704.4812796			
R12	12.532	12.606	12.569	598.4943856	658.2238981	34.4038975	699.5028
R12	10.911	12.851	11.881	669.8160371			
R12	12.015	11.828	11.9215	665.2727379			
R13	12.559	12.544	12.5515	600.1644574			
R13	12.816	12.065	12.4405	610.9221367			
R13	12.335	12.808	12.5715	598.2563731	633.5154472	37.83792725	759.5028
R13	11.455	12.287	11.871	670.9450037			
R13	11.715	11.743	11.729	687.2892651			

Table 19: Tabularized hardness calculation for a sample held for 90 min at 1200°C in an air environment and quenched in N_2 gas with a cooling rate of 200°C/s.

Indent row Nr.	d_1 [μm]	d_2 [μm]	d [μm]	Hardness [HV]	averaged [HV]	Std. dev. [HV]	Depth [μm]
R1	10.639	11.173	10.906	794.9330371			
R1	10.356	9.279	9.8175	980.9790064			
R1	9.823	10.113	9.968	951.5803702	891.4575097	70.02170558	28.6188
R1	10.657	9.868	10.2625	897.7495434			
R1	10.681	10.639	10.66	832.0455913			
R2	11.99	12.544	12.267	628.3256695			
R2	11.183	12	11.5915	703.6914173			
R2	11.728	11.173	11.4505	721.1284522	700.165564	79.49216	88.6188
R2	12.308	12.544	12.426	612.3487486			
R2	11.183	10.095	10.639	835.3335323			
R3	11.987	12.532	12.2595	629.0946868			
R3	11.987	11.446	11.7165	688.756546			
R3	11.443	11.99	11.7165	688.756546	701.008997	82.20603485	148.6188
R3	12.535	11.766	12.1505	640.4323094			
R3	10.911	10.084	10.4975	858.004897			
R4	12.816	13.375	13.0955	551.3372851			
R4	11.715	12.308	12.0115	655.340551			
R4	12.535	11.99	12.2625	628.7869105	627.2608674	41.45027153	208.6188
R4	11.987	12.544	12.2655	628.4793601			
R4	12.544	11.173	11.8585	672.3602304			
R5	11.728	11.766	11.747	685.1846037			
R5	12.816	13.089	12.9525	563.578389			
R5	11.99	12.544	12.267	628.3256695	644.7319336	46.06903245	268.6188
R5	12.263	11.718	11.9905	657.6380703			
R5	11.443	11.987	11.715	688.9329354			
R6	11.728	12.535	12.1315	642.4399329			
R6	11.715	12.816	12.2655	628.4793601			
R6	12.544	11.728	12.136	641.9635908	636.7300456	6.823109149	328.6188
R6	12.535	12	12.2675	628.2744518			
R6	11.99	12.272	12.131	642.4928925			
R7	12.559	11.99	12.2745	627.5580614			
R7	11.99	12.535	12.2625	628.7869105			
R7	12.805	12.532	12.6685	589.130004	607.0695675	17.76729059	388.6188
R7	12.544	12.544	12.544	600.8823431			
R7	13.077	12.263	12.67	588.9905182			
R8	12.015	12.808	12.4115	613.7803633			
R8	12.808	11.455	12.1315	642.4399329			
R8	12.532	13.077	12.8045	576.6818516	607.361105	33.57512784	448.6188
R8	13.089	12.877	12.983	560.9335534			
R8	11.718	12.535	12.1265	642.969824			
R9	11.99	12.015	12.0025	656.3237255			
R9	12.263	12.308	12.2855	626.4347781			
R9	13.622	12.532	13.077	552.8983396	613.328434	37.92498947	508.6188
R9	13.089	12.272	12.6805	588.015503			
R9	12.263	11.99	12.1265	642.969824			
R10	11.99	12.272	12.131	642.4928925			
R10	12.535	11.99	12.2625	628.7869105			
R10	12.263	12.272	12.2675	628.2744518	648.4189962	21.45372791	568.6188
R10	12.272	11.728	12	656.5972222			
R10	11.173	12.308	11.7405	685.9435037			
R11	12.535	12.535	12.535	601.7455075			
R11	13.089	12.532	12.8105	576.141782			
R11	13.08	11.987	12.5335	601.889549	609.2876559	22.20709968	628.6188
R11	12.015	12.559	12.287	626.2818368			
R11	12.287	12.015	12.151	640.3796043			
R12	12.808	13.375	13.0915	551.6742497			
R12	12	11.99	11.995	657.1447287			
R12	13.08	12.287	12.6835	587.7373719	597.5064948	34.19161794	688.6188
R12	12.805	12.26	12.5325	601.9856054			
R12	12.532	12.808	12.67	588.9905182			
R13	13.625	13.089	13.357	529.9607197			
R13	12.544	12.272	12.408	614.1266777			
R13	12.26	11.99	12.125	643.1289191	597.8997612	38.06713331	748.6188
R13	12.272	12.559	12.4155	613.3849341			
R13	13.352	11.99	12.671	588.8975552			

Table 20: Tabularized hardness calculation for a sample held for 60 min at 1200°C in an air environment and quenched in N_2 gas with a cooling rate of 1°C/s.

Indent row Nr.	d₁ [µm]	d₂ [µm]	d [µm]	Hardness [HV]	averaged [HV]	Std. dev. [HV]	Depth [µm]
R1	10.639	10.353	10.496	858.2501522			
R1	10.367	10.367	10.367	879.74202			
R1	10.625	11.183	10.904	795.2246754	873.4716064	51.05502816	24.3104
R1	10.113	10.625	10.369	879.4026788			
R1	10.08	9.823	9.9515	954.7385057			
R2	12.805	11.173	11.989	657.802641			
R2	10.911	10.901	10.906	794.9330371			
R2	10.442	11.446	10.944	789.4222528	799.9305046	82.34603318	84.3104
R2	10.356	10.113	10.2345	902.6684691			
R2	10.681	10.353	10.517	854.8261227			
R3	11.183	12.287	11.735	686.5866351			
R3	12.308	11.99	12.149	640.5904636			
R3	10.625	11.183	10.904	795.2246754	738.2138858	65.47312919	144.3104
R3	10.385	11.173	10.779	813.7754602			
R3	11.455	10.928	11.1915	754.8921949			
R4	13.08	11.455	12.2675	628.2744518			
R4	12.544	11.794	12.169	638.4865469			
R4	11.472	11.173	11.3225	737.5252178	654.1504355	41.96887713	204.3104
R4	12.535	11.794	12.1645	638.9590235			
R4	12.015	12.535	12.275	627.5069375			
R5	12.26	12.559	12.4095	613.9782214			
R5	12.015	11.715	11.865	671.6237543			
R5	12.808	12.544	12.676	588.43307	637.9549177	36.62200053	264.3104
R5	11.455	12	11.7275	687.4650911			
R5	12.535	12	12.2675	628.2744518			
R6	12.816	12.805	12.8105	576.141782			
R6	11.443	12.532	11.9875	657.9672734			
R6	12.287	12.535	12.411	613.8298189	619.7114746	27.98750499	324.3104
R6	12.535	11.766	12.1505	640.4323094			
R6	12.065	12.831	12.448	610.1861895			
R7	13.375	12.535	12.955	563.3608961			
R7	13.647	12.263	12.955	563.3608961			
R7	13.08	12.037	12.5585	599.4955909	576.1085238	27.15883059	384.3104
R7	12.851	13.622	13.2365	539.6537574			
R7	13.077	11.728	12.4025	614.6714785			
R8	13.08	13.622	13.351	530.4371603			
R8	12.808	13.352	13.08	552.6447456			
R8	11.472	11.455	11.4635	719.493811	588.1272737	68.12163137	444.3104
R8	13.08	12.308	12.694	586.7654655			
R8	12.559	13.633	13.096	551.2951863			
R9	13.894	13.375	13.6345	508.6078989			
R9	12.335	13.089	12.712	585.1049399			
R9	13.35	12.559	12.9545	563.4043846	566.6264309	31.45400633	504.3104
R9	12.559	13.077	12.818	575.4677613			
R9	13.08	12.015	12.5475	600.5471696			
R10	12.831	13.394	13.1125	549.9086242			
R10	13.361	12.808	13.0845	552.2646816			
R10	12.015	13.622	12.8185	575.4228686	568.3576409	18.77077372	564.3104
R10	12.808	12.272	12.54	601.2657423			
R10	12.287	13.633	12.96	562.9262879			
R11	13.622	12.831	13.2265	540.4700848			
R11	12.532	13.35	12.941	564.5804802			
R11	13.625	11.455	12.54	601.2657423	581.7791485	25.07303745	624.3104
R11	12.544	12.535	12.5395	601.313693			
R11	12.808	12.272	12.54	601.2657423			
R12	12.808	12.532	12.67	588.9905182			
R12	13.897	12.606	13.2515	538.4327296			
R12	11.494	13.089	12.2915	625.8233488	613.8975506	53.81104841	684.3104
R12	11.987	11.2	11.5935	703.4486499			
R12	12.308	12.535	12.4215	612.7925063			
R13	12.263	13.361	12.812	576.0068832			
R13	12.58	12.535	12.5575	599.5910748			
R13	13.622	12.287	12.9545	563.4043846	568.6221754	22.59245232	744.3104
R13	12.308	13.361	12.8345	573.9890726			
R13	12.805	13.905	13.355	530.1194619			

Table 21: Tabularized hardness calculation for a sample held for 60 min at 1200°C in an air environment and quenched in N_2 gas with a cooling rate of 15°C/s.

Indent row Nr.	d_1 [µm]	d_2 [µm]	d [µm]	Hardness [HV]	averaged [HV]	Std. dev. [HV]	Depth [µm]
R1	10.639	10.385	10.512	855.6395069			
R1	12.015	11.2	11.6075	701.7527909			
R1	12	12.263	12.1315	642.4399329	686.1410467	92.02160394	27.348
R1	12	12.263	12.1315	642.4399329			
R1	13.089	12.263	12.676	588.43307			
R2	13.755	12.816	13.2855	535.6803623			
R2	11.183	12	11.5915	703.6914173			
R2	12.272	12.037	12.1545	640.010851	577.825173	80.45813527	87.348
R2	13.375	14.295	13.835	493.972994			
R2	13.99	13.089	13.5395	515.7702404			
R3	12.808	13.179	12.9935	560.027343			
R3	13.72	12.831	13.2755	536.4876873			
R3	12.816	13.69	13.253	538.3108548	542.4206119	11.20713982	147.348
R3	13.69	12.544	13.117	549.5313788			
R3	13.08	13.69	13.385	527.7457957			
R4	13.69	12.532	13.111	550.034459			
R4	12.831	13.449	13.14	547.6092844			
R4	13.179	12.272	12.7255	583.8641672	554.2044311	22.95900632	207.348
R4	12.559	13.148	12.8535	572.2933894			
R4	13.647	13.394	13.5205	517.2208554			
R5	13.361	13.352	13.3565	530.0003986			
R5	12.851	12.272	12.5615	599.209276			
R5	12.535	13.179	12.857	571.9818464	557.1176466	25.3548041	267.348
R5	13.485	12.816	13.1505	546.7351576			
R5	13.103	13.419	13.261	537.6615541			
R6	13.352	13.08	13.216	541.3292238			
R6	12.544	12.272	12.408	614.1266777			
R6	12.638	13.103	12.8705	570.7825604	554.8085476	34.87878485	327.348
R6	12.58	14.025	13.3025	534.3120861			
R6	13.72	13.419	13.5695	513.4921899			
R7	13.361	13.99	13.6755	505.5627942			
R7	13.103	13.103	13.103	550.7063081			
R7	13.352	14.334	13.843	493.4022157	521.7061334	26.48493331	387.348
R7	14.295	13.148	13.7215	502.1787754			
R7	12.58	13.485	13.0325	556.6805735			
R8	12.808	13.905	13.3565	530.0003986			
R8	13.08	14.646	13.863	491.9795905			
R8	13.961	13.089	13.525	516.8767361	527.2615244	36.95453853	447.348
R8	13.179	14.295	13.737	501.0461584			
R8	12.638	12.544	12.591	596.4047385			
R9	13.919	12.805	13.362	529.5641761			
R9	14.025	13.666	13.8455	493.2240503			
R9	13.937	14.025	13.981	483.7099954	511.1390214	31.02891704	507.348
R9	14.532	13.375	13.9535	485.6184962			
R9	13.089	12.816	12.9525	563.578389			
R10	14.48	13.905	14.1925	469.400694			
R10	12.831	14.334	13.5825	512.5097192			
R10	14.503	13.937	14.22	467.5869054	503.8302869	30.23625843	567.348
R10	13.352	13.089	13.2205	540.9607707			
R10	13.394	13.352	13.373	528.6933453			
R11	13.919	15.452	14.6855	438.4136404			
R11	15.412	14.462	14.937	423.7744522			
R11	13.69	13.633	13.6615	506.599504	489.6302398	54.16265202	627.348
R11	12.58	13.08	12.83	574.3917856			
R11	13.647	13.72	13.6835	504.9718167			
R12	14.025	13.937	13.981	483.7099954			
R12	13.394	14.565	13.9795	483.8138051			
R12	13.894	13.647	13.7705	498.611297	509.2804475	29.34081555	687.348
R12	13.919	13.103	13.511	517.9484589			
R12	13.103	12.831	12.967	562.3186808			
R13	14.462	14.532	14.497	449.8888765			
R13	13.937	13.394	13.6655	506.3029761			
R13	13.08	13.961	13.5205	517.2208554	515.8289761	43.8697052	747.348
R13	12.535	12.831	12.683	587.7837134			
R13	13.103	13.919	13.511	517.9484589			

Table 22: Tabularized hardness calculation for a sample held for 60 min at 1200°C in an air environment and quenched in N_2 gas with a cooling rate of 20°C/s.

Indent row Nr.	d_1 [μm]	d_2 [μm]	d [μm]	Hardness [HV]	averaged [HV]	Std. dev. [HV]	Depth [μm]
R1	10.629	11.728	11.1785	756.6490147			
R1	10.084	10.08	10.082	930.1824622			
R1	12.808	12.808	12.808	576.3667188	687.9600226	138.5706317	38.0308
R1	13.361	12.263	12.812	576.0068832			
R1	12.263	12.831	12.547	600.5950344			
R2	12.532	12.263	12.3975	615.1673812			
R2	12	13.103	12.5515	600.1644574			
R2	12.808	13.352	13.08	552.6447456	589.8045114	31.56843534	98.0308
R2	12.272	12.263	12.2675	628.2744518			
R2	13.625	12.532	13.0785	552.7715208			
R3	13.622	14.17	13.896	489.6456745			
R3	13.375	12.263	12.819	575.3779812			
R3	12.272	13.625	12.9485	563.9266396	549.0367653	30.57865846	158.0308
R3	12.808	13.089	12.9485	563.9266396			
R3	12.816	13.352	13.084	552.3068915			
R4	12.808	13.352	13.08	552.6447456			
R4	13.08	13.375	13.2275	540.3883688			
R4	13.089	13.897	13.493	519.3312931	534.5312943	13.15918446	218.0308
R4	13.361	13.625	13.493	519.3312931			
R4	13.089	13.352	13.2205	540.9607707			
R5	13.897	12.535	13.216	541.3292238			
R5	13.08	13.352	13.216	541.3292238			
R5	13.352	12.816	13.084	552.3068915	526.6550288	22.80893704	278.0308
R5	13.625	13.897	13.761	499.299974			
R5	13.633	13.897	13.765	499.009831			
R6	12.808	13.352	13.08	552.6447456			
R6	13.625	13.352	13.4885	519.6778669			
R6	13.361	13.894	13.6275	509.1305435	530.7705664	18.27370919	338.0308
R6	13.352	12.808	13.08	552.6447456			
R6	13.625	13.35	13.4875	519.7549305			
R7	13.08	13.361	13.2205	540.9607707			
R7	13.089	12.544	12.8165	575.6024708			
R7	14.17	13.633	13.9015	489.2583035	507.8185687	44.26648581	398.0308
R7	14.17	14.722	14.446	453.0710493			
R7	14.442	13.622	14.032	480.2002492			
R8	13.077	13.103	13.09	551.8006911			
R8	13.622	12.58	13.101	550.8744627			
R8	13.394	13.622	13.508	518.1785474	518.4126356	32.94914416	458.0308
R8	13.905	13.35	13.6275	509.1305435			
R8	14.442	14.167	14.3045	462.0789334			
R9	13.361	13.361	13.361	529.6434492			
R9	12.535	12.808	12.6715	588.8510819			
R9	13.35	13.103	13.2265	540.4700848	519.1968349	52.43958302	518.0308
R9	13.897	13.375	13.636	508.4960083			
R9	15.266	14.442	14.854	428.52355			
R10	13.361	13.919	13.64	508.1978139			
R10	13.897	13.361	13.629	509.0184804			
R10	13.352	13.919	13.6355	508.5333011	493.7223272	21.50604898	578.0308
R10	14.17	13.625	13.8975	489.5399822			
R10	14.714	14.17	14.442	453.3220582			
R11	13.905	13.361	13.633	508.7198264			
R11	13.625	13.633	13.629	509.0184804			
R11	13.905	13.897	13.901	489.2935001	491.4987707	15.40800984	638.0308
R11	13.625	14.734	14.1795	470.2617972			
R11	13.897	14.167	14.032	480.2002492			
R12	13.35	13.625	13.4875	519.7549305			
R12	13.897	13.897	13.897	489.5752092			
R12	13.08	12.535	12.8075	576.411722	512.9976392	34.3101494	698.0308
R12	14.167	13.897	14.032	480.2002492			
R12	13.352	14.177	13.7645	499.046085			
R13	14.984	13.897	14.4405	453.4162403			
R13	14.714	13.622	14.168	471.0255191			
R13	14.167	14.177	14.172	470.7596658	476.8294147	16.04921397	758.0308
R13	13.08	14.442	13.761	499.299974			
R13	13.622	14.17	13.896	489.6456745			

Table 23: Tabularized hardness calculation for a sample held for 60 min at 1200°C in an air environment and quenched in N_2 gas with a cooling rate of 50°C/s.

Indent row Nr.	d_1 [µm]	d_2 [µm]	d [µm]	Hardness [HV]	averaged [HV]	Std. dev. [HV]	Depth [µm]
R1	8.986	8.718	8.852	1206.642791			
R1	8.178	8.463	8.3205	1365.723188			
R1	8.718	8.178	8.448	1324.810382	1308.837611	78.37019815	13.468
R1	8.722	7.633	8.1775	1413.905642			
R1	8.718	8.795	8.7565	1233.106052			
R2	10.657	10.41	10.5335	852.1501681			
R2	13.08	11.728	12.404	614.5228246			
R2	12.263	12.26	12.2615	628.8894775	696.233731	93.50432604	73.468
R2	11.173	11.183	11.178	756.7167071			
R2	12.263	12.26	12.2615	628.8894775			
R3	11.718	13.08	12.399	615.0185474			
R3	11.987	12.263	12.125	643.1289191			
R3	11.99	12.535	12.2625	628.7869105	640.8955667	25.52849561	133.468
R3	11.99	12.535	12.2625	628.7869105			
R3	11.715	11.718	11.7165	688.756546			
R4	11.2	11.715	11.4575	720.2475694			
R4	12.535	11.728	12.1315	642.4399329			
R4	12.015	11.446	11.7305	687.1135065	643.1634643	56.23165413	193.468
R4	12.263	12.808	12.5355	601.6975051			
R4	13.625	12.263	12.944	564.3188076			
R5	11.17	13.089	12.1295	642.6518107			
R5	11.446	11.183	11.3145	738.5685317			
R5	11.446	12	11.723	687.9929742	667.9961322	40.62240519	253.468
R5	12	12.535	12.2675	628.2744518			
R5	11.99	12.272	12.131	642.4928925			
R6	12.816	11.173	11.9945	657.1995171			
R6	12	12.535	12.2675	628.2744518			
R6	13.089	12.015	12.552	600.1166441	620.4223999	28.93301888	313.468
R6	12.015	12.287	12.151	640.3796043			
R6	13.089	12.532	12.8105	576.141782			
R7	11.743	12.544	12.1435	641.1708638			
R7	12	12.535	12.2675	628.2744518			
R7	13.08	11.99	12.535	601.7455075	625.8668763	22.0775265	373.468
R7	12.272	11.715	11.9935	657.3091142			
R7	11.728	13.361	12.5445	600.834444			
R8	13.08	12.535	12.8075	576.411722			
R8	13.361	12.535	12.948	563.9701936			
R8	12.037	11.987	12.012	655.2859949	597.3095956	31.62177335	433.468
R8	12.532	12.535	12.5335	601.889549			
R8	12.535	12.805	12.67	588.9905182			
R9	12.808	12.544	12.676	588.43307			
R9	12.544	13.077	12.8105	576.141782			
R9	13.077	12.263	12.67	588.9905182	586.3259188	9.494505236	493.468
R9	12.808	12.263	12.5355	601.6975051			
R9	12.808	12.808	12.808	576.3667188			
R10	12.808	13.077	12.9425	564.4496211			
R10	13.35	12.816	13.083	552.391326			
R10	12.532	13.08	12.806	576.5467631	581.9699258	23.11266355	553.468
R10	12.532	12.535	12.5335	601.889549			
R10	11.718	13.089	12.4035	614.5723699			
R11	12.831	12.808	12.8195	575.333099			
R11	11.99	12.808	12.399	615.0185474			
R11	12.544	13.089	12.8165	575.6024708	593.5793167	17.87565655	613.468
R11	12.287	13.089	12.688	587.3205452			
R11	12.816	11.99	12.403	614.6219212			
R12	13.375	13.08	13.2275	540.3883688			
R12	12.26	12.816	12.538	601.4575795			
R12	12.272	12.272	12.272	627.8137744	577.3598359	34.1926143	673.468
R12	13.077	12.535	12.806	576.5467631			
R12	13.361	13.089	13.225	540.5926937			
R13	12.808	13.089	12.9485	563.9266396			
R13	12.263	12.535	12.399	615.0185474			
R13	13.375	12.535	12.955	563.3608961	567.0045899	25.44458205	733.468
R13	12.808	13.375	13.0915	551.6742497			
R13	13.35	13.089	13.2195	541.0426167			

Table 24: Tabularized hardness calculation for a sample held for 60 min at 1200°C in an air environment and quenched in N₂ gas with a cooling rate of 100°C/s.

Indent row Nr.	d₁ [µm]	d₂ [µm]	d [µm]	Hardness [HV]	averaged [HV]	Std. dev. [HV]	Depth [µm]
R1	11.99	11.99	11.99	657.6929204			
R1	10.385	11.183	10.784	813.0210214			
R1	8.995	9.812	9.4035	1069.257919	868.9868307	135.0286424	21.7034
R1	10.367	10.367	10.367	879.74202			
R1	9.808	10.41	10.109	925.2202726			
R2	11.494	10.898	11.196	754.2854904			
R2	10.08	10.367	10.2235	904.6119709			
R2	12.535	11.17	11.8525	673.0411302	779.6740085	76.71563187	81.7034
R2	11.494	10.911	11.2025	753.4104297			
R2	10.911	10.657	10.784	813.0210214			
R3	12.532	12.263	12.3975	615.1673812			
R3	12.559	12.535	12.547	600.5950344			
R3	11.446	12.272	11.859	672.3035354	658.7020318	43.20671826	141.7034
R3	12.015	11.2	11.6075	701.7527909			
R3	12	11.183	11.5915	703.6914173			
R4	12.808	12.535	12.6715	588.8510819			
R4	11.718	11.446	11.582	704.84628			
R4	12.037	11.443	11.74	686.0019328	656.2780343	42.06729765	201.7034
R4	11.987	12.544	12.2655	628.4793601			
R4	11.987	11.715	11.851	673.2115168			
R5	13.352	13.361	13.3565	530.0003986			
R5	12.263	11.99	12.1265	642.969824			
R5	12.272	12.816	12.544	600.8823431	630.0315842	63.17316016	261.7034
R5	12.58	11.446	12.013	655.1769033			
R5	11.173	11.728	11.4505	721.1284522			
R6	12.308	13.352	12.83	574.3917856			
R6	12.263	11.743	12.003	656.2690467			
R6	12.272	11.99	12.131	642.4928925	617.7980485	29.17676387	321.7034
R6	12.535	12.544	12.5395	601.313693			
R6	12.808	12	12.404	614.5228246			
R7	11.99	12.037	12.0135	655.1223678			
R7	12.287	12.535	12.411	613.8298189			
R7	12.559	12.559	12.559	599.4478575	606.7258354	33.59952491	381.7034
R7	13.375	12.831	13.103	550.7063081			
R7	12	12.808	12.404	614.5228246			
R8	12.559	12.816	12.6875	587.3668373			
R8	12.263	12.272	12.2675	628.2744518			
R8	13.08	12.263	12.6715	588.8510819	598.9764629	19.13059951	441.7034
R8	12.535	13.08	12.8075	576.411722			
R8	12.559	12.26	12.4095	613.9782214			
R9	12.26	12.287	12.2735	627.6603278			
R9	12.535	12.544	12.5395	601.313693			
R9	12.535	12.272	12.4035	614.5723699	594.3264725	27.23972802	501.7034
R9	12.535	13.08	12.8075	576.411722			
R9	13.08	13.103	13.0915	551.6742497			
R10	12.808	12.532	12.67	588.9905182			
R10	12.535	13.361	12.948	563.9701936			
R10	12.544	12.808	12.676	588.43307	591.5884723	20.3962543	561.7034
R10	13.077	12.263	12.67	588.9905182			
R10	12.559	11.99	12.2745	627.5580614			
R11	12.805	13.352	13.0785	552.7715208			
R11	12.851	12.816	12.8335	574.0785278			
R11	12.263	12.544	12.4035	614.5723699	578.4274151	21.19501943	621.7034
R11	13.08	12.808	12.944	564.3188076			
R11	12.816	12.58	12.698	586.3958495			
R12	12.272	12.808	12.54	601.2657423			
R12	12.287	12.544	12.4155	613.3849341			
R12	12.831	12.805	12.818	575.4677613	590.8874562	14.7886858	681.7034
R12	12.808	12.535	12.6715	588.8510819			
R12	12.831	12.805	12.818	575.4677613			
R13	12.831	12.877	12.854	572.2488677			
R13	12.808	13.625	13.2165	541.288266			
R13	12.808	12.831	12.8195	575.333099	561.0883236	12.64012422	741.7034
R13	13.352	12.808	13.08	552.6447456			
R13	12.808	13.089	12.9485	563.9266396			

Table 25:Tabular diffusional calculation for a specimen which was held for 45 min at 1000°C in an air environment and quenched with a cooling rate of 200°C/s in N$_2$ gas.

Indent row Nr.	Hardness [HV]	Depth [mm]	Hardness term	Diffusion term
1	892.7860708	0.016	0.01640	0.15531
2	545.4531681	0.076	0.80579	0.65342
3	533.6390677	0.136	0.83264	0.90832
4	483.7278636	0.196	0.94607	0.98498
5	471.619692	0.256	0.97359	0.99851
6	460.373895	0.316	0.99915	0.99991
7	472.6846434	0.376	0.97117	1.00000
8	465.352405	0.436	0.98784	1.00000
9	482.1802557	0.496	0.94959	1.00000
10	474.3598276	0.556	0.96736	1.00000
11	476.4179166	0.616	0.96269	1.00000
12	458.3063426	0.676	1.00385	1.00000
13	472.9738987	0.736	0.97051	1.00000

Table 26: Tabular diffusional calculation for a specimen which was held for 45 min at 1050°C in an air environment and quenched with a cooling rate of 200°C/s in N$_2$ gas.

Indent row Nr.	Hardness [HV]	Depth [mm]	Hardness term	Diffusion term
1	641.1268507	0.031	0.055	0.13501
2	589.4867805	0.091	0.378	0.38529
3	545.2635656	0.151	0.655	0.59723
4	572.9842327	0.211	0.481	0.75801
5	537.3571018	0.271	0.704	0.86725
6	536.1233348	0.331	0.71173	0.93374
7	512.7367451	0.391	0.85790	0.96999
8	493.3031683	0.451	0.97936	0.98770
9	511.5148701	0.511	0.86553	0.99544
10	521.0225302	0.571	0.80611	0.99848
11	502.405951	0.631	0.92246	0.99954
12	494.3334975	0.691	0.97292	0.99988
13	491.529434	0.751	0.99044	0.99997

Table 27: Tabular diffusional calculation for a specimen which was held for 45 min at 1100°C in an air environment and quenched with a cooling rate of 200°C/s in N_2 gas.

Indent row Nr.	Hardness [HV]	Depth [mm]	Hardness term	Diffusion term
1	850.5683147	0.035	0.25495	0.22289
2	693.6690049	0.095	0.65726	0.55931
3	610.8633445	0.155	0.86958	0.79196
4	609.6792211	0.215	0.87262	0.91935
5	590.0514739	0.275	0.92294	0.97457
6	594.1210803	0.335	0.91251	0.99353
7	593.0650889	0.395	0.91522	0.99868
8	553.983813	0.455	1.01543	0.99978
9	561.4255239	0.515	0.99634	0.99997
10	561.8377387	0.575	0.99529	1.00000
11	570.8966016	0.635	0.97206	1.00000
12	580.8208413	0.695	0.94661	1.00000
13	564.1651112	0.755	0.98932	1.00000

Table 28: Tabular diffusional calculation for a specimen which was held for 45 min at 1150°C in an air environment and quenched with a cooling rate of 200°C/s in N_2 gas.

Indent row Nr.	Hardness [HV]	Depth [mm]	Hardness term	Diffusion term
1	711.9779456	0.024	0.36676	0.18419
2	660.2905197	0.084	0.58212	0.58223
3	591.1120609	0.144	0.87037	0.83475
4	581.8133629	0.204	0.90911	0.95058
5	566.84774	0.264	0.97147	0.98899
6	567.2714946	0.324	0.96970	0.99819
7	559.2502834	0.384	1.00312	0.99978
8	560.9686921	0.444	0.99596	0.99998
9	550.8142711	0.504	1.03827	1.00000
10	558.2933685	0.564	1.00711	1.00000
11	556.6253816	0.624	1.01406	1.00000
12	566.4502107	0.684	0.97312	1.00000
13	568.2437099	0.744	0.96565	1.00000

Table 29: Tabular diffusional calculation for a specimen which was held for 45 min at 1250°C in an air environment and quenched with a cooling rate of 200°C/s in N_2 gas.

Indent row Nr.	Hardness [HV]	Depth [mm]	Hardness term	Diffusion term
1	989.5199993	0.039	0.02994	0.15859
2	887.2169378	0.099	0.32224	0.38903
3	849.6928876	0.159	0.42945	0.58624
4	800.3792095	0.219	0.57035	0.73979
5	748.3703157	0.279	0.71894	0.84857
6	695.0774982	0.339	0.87121	0.91869
7	668.6768654	0.399	0.94664	0.95980
8	670.1412005	0.459	0.94245	0.98174
9	642.9811669	0.519	1.02005	0.99239
10	666.8319025	0.579	0.95191	0.99709
11	648.8323609	0.639	1.00334	0.99898
12	662.3517236	0.699	0.96471	0.99968
13	667.2200327	0.759	0.95080	0.99991

Table 30: Tabular diffusional calculation for a specimen which was held for 45 min at 1300°C in an air environment and quenched with a cooling rate of 200°C/s in N_2 gas.

Indent row Nr.	Hardness [HV]	Depth [mm]	Hardness term	Diffusion term
1	1386.473076	0.024	0.01780	0.07617
2	1175.855072	0.084	0.29493	0.25959
3	980.2588718	0.144	0.55229	0.42929
4	977.5474062	0.204	0.55586	0.57786
5	765.2494594	0.264	0.83520	0.70092
6	721.9820988	0.324	0.89213	0.79738
7	695.657771	0.384	0.92677	0.86891
8	680.4096097	0.444	0.94683	0.91911
9	674.6336678	0.504	0.95443	0.95243
10	667.7524031	0.564	0.96348	0.97337
11	692.4739913	0.624	0.93096	0.98582
12	653.273445	0.684	0.98253	0.99282
13	696.4350859	0.744	0.92574	0.99654